Icarus 360 (2021) 114332

Contents lists available at ScienceDirect

Icarus

journal homepage: www.elsevier.com/locate/icarus

Landform evolution of Oudemans crater and its bounding plateau plains on Mars: Geomorphological constraints on the Tharsis ice-cap hypothesis

An Yin *, Seulgi Moon, Mackenzie Day

Department of Earth, Planetary, and Space Sciences, University of California, Los Angeles, California, CA 90095-1567, USA

ARTICLE INFO

Keywords:
Tharsis ice cap
Circum-Tharsis outflow channels
Glacial landform
MGSLs

ABSTRACT

In this study we address the question of whether the Tharsis rise that occupies ~25 % of the surface area of Mars was once covered by an ice cap, and the sudden ice-cap melting was responsible for the catastrophic development of the Late Hesperian (3.5-3.6 Ga) circum-Tharsis giant (>1000s km in length) outflow channels. To achieve this goal, we conducted geomorphologic mapping across the Oudemans crater basin (~125 km in diameter) at elevations of ~2.7 km to ~5.0 km and its bounding plateau plains at elevations of ~5.3 km to ~6.7 km in the central Tharsis rise. Our work shows that the Oudemans-impact-induced landforms were superposed by a suite of younger landform assemblages, which consist of horn-like peaks, arête-like ridges, cirque-like depressions, hanging-valley-like features, trim-line-like escarpments, lobate ridges, striated, pitted and hummocky terrains, and features resembling drumlins, crag-and-tails and roches moutonnées. A plateau-plain striated terrain on a hummocky surface exhibits streamlined linear ridges that are 400-2000 m wide and up to ~17 km long. The average length-width ratio (~9), shape, surface texture, and associated washboard landform pattern of the linear morphological features in the striated terrain on Mars are comparable to mega-scale glacial lineations (MSGLs) on Earth. Using well-understood Earth analogues as a guide, we interpret the post-Oudemans-impact landform assemblages to have formed during regional ice-sheet-style glaciation. We further suggest the striated terrain on the plateau plains to have been generated by a fast-moving ice stream in a regional ice sheet that filled 4-km deep Oudemans crater and covered the crater-bounding plateau plains in the central Tharsis rise. The volume of the glacier ice stored in the Oudemans crater basin alone is estimated on the order of ~200,000 km^3. The shape of the inferred glacier-induced landforms and their cross-cutting relationships require early northward-flowing northward-advancing glaciation, followed by southward-flowing northward-retreating glaciation. The size-frequency distribution of the craters superposed on top of the interpreted glaciated landforms in the mapped area yields a glaciation age of ca. 3.5 Ga, coeval with the estimated age of the interpreted glacial landforms along the 2000-km long Valles Marineris trough zone east of the study area. The inferred glaciation age is also coeval with the development of the circum-Tharsis outflow channels. Although our work supports the Tharsis ice-cap hypothesis, the full extent of the ice cap within and possibly beyond the Tharsis rise remains unconstrained.

1. Introduction

With a spatial coverage of ~25% of the planet, the Tharsis rise is the youngest tectonic province and one of the most dominant topographic features on Mars (Fig. 1A) (Zuber, 2001; Solomon et al., 2005). Past studies have led to the hypothesis that the Tharsis rise may have hosted a 1-3 km thick ice cap in the geological past (Baker et al., 2000; Lucchitta, 2001; Harrison and Grimm, 2004; Cassanelli and Head, 2019). The ice-cap glacial flow, ice-cap melting, and ice-cap-melting-induced hydro-geological processes may have contributed individually or collectively to the Late Hesperian (3.5-3.6 Ga) formation of giant (>4000-6000 km long) circum-Tharsis outflow channels that are unique for their sizes (i.e., in length, depth, and width) in the solar system (Lucchitta, 2001; Harrison and Grimm, 2004; Carr and Head III, 2010; Carr and Head, 2015, 2019; Cassanelli and Head, 2019) (Fig. 1A).

Despite the potential impact on the landscape evolution of nearly a half of Mars' surface, the Tharsis ice-cap hypothesis has not yet been tested systematically. Current studies indicate that a high-elevation domain (>~6 km) (see the inset map in Fig. 1A) (note that elevations mentioned in this study are all referenced from the global datum defined

* Corresponding author.
E-mail addresses: ayin54@gmail.com (A. Yin), sgmoon@ucla.edu (S. Moon), daym@epss.ucla.edu (M. Day).

https://doi.org/10.1016/j.icarus.2021.114332
Received 14 July 2020; Received in revised form 15 January 2021; Accepted 15 January 2021
Available online 27 January 2021

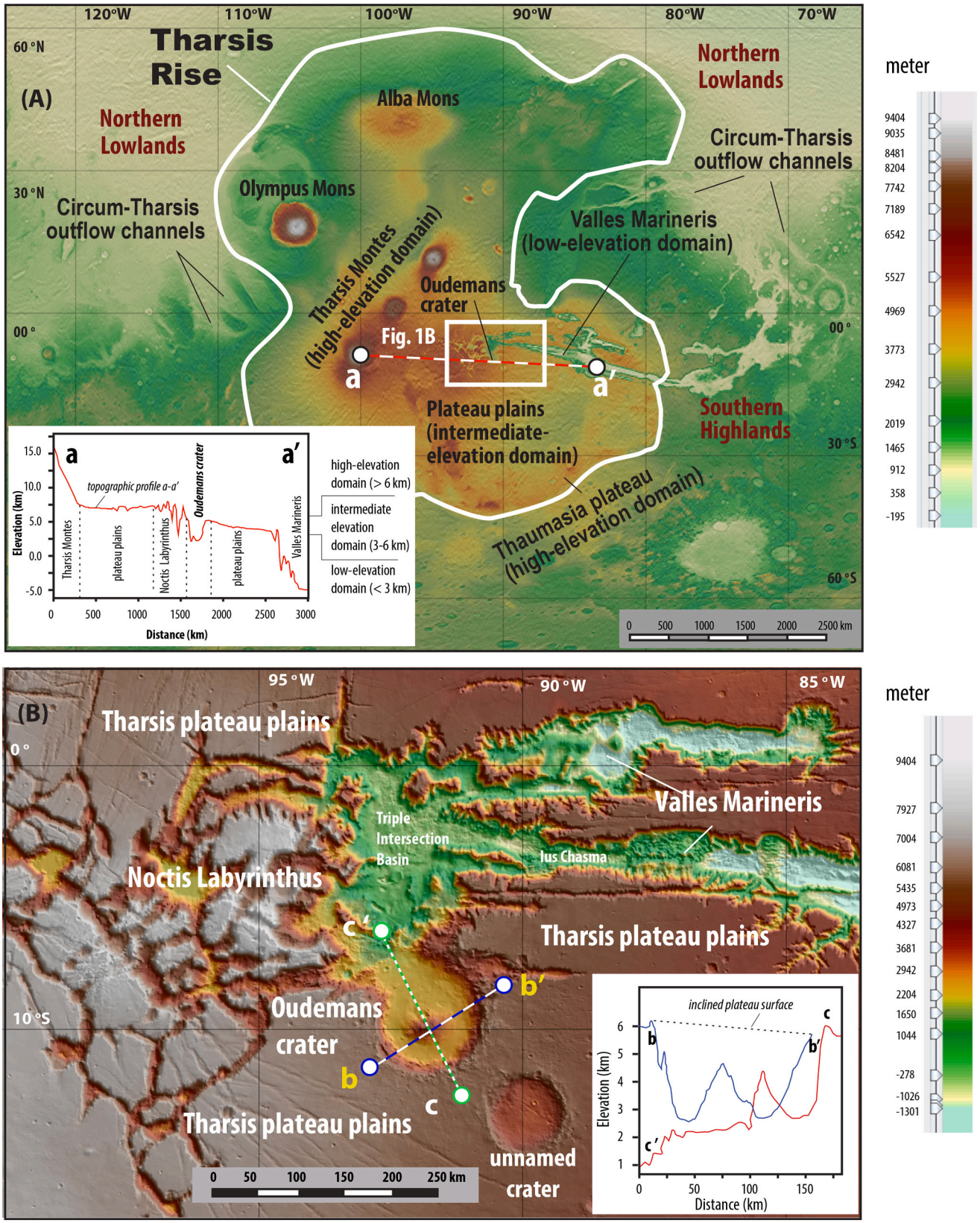

Fig. 1. (A) A blended digital-elevation-model (DEM) map of the Tharsis rise at a resolution of 200 m/pixel. We divide the Tharsis rise into high-elevation (>~6 km), intermediate-elevation (~3-6 km), and low-elevation (<~3 km) domains as shown in the inset topographic profile a-a' across a portion of the region. (B) Oudemans crater and bounding plateau plains are located within the intermediate-elevation domain. Note that the northern crater wall is missing and its basin floor connects with the floor of Noctis Labyrinthus and Valles Marineris troughs. The inset in the lower right shows two topographic profiles b-b' and c-c' across Oudemans crater.

in Smith et al., 1999) may have experienced mountain glaciation, which is restricted only to western flanks of shield volcanoes in western Tharsis (Lucchitta, 1981; Head and Marchant, 2003; Milkovich et al., 2006; Shean et al., 2005; Kadish et al., 2008; Kadish et al., 2014; Rossi et al., 2011; Head and Weiss, 2014; Scanlon et al., 2014, 2015a, 2015b; Parsons et al., 2020). Existing work also shows that a low-elevation (<~3 km) Tharsis domain (i.e., Valles Marineris in Fig. 1A) displays possible glacier-generated landforms (Fueten et al., 2011; Mège and Bourgeois, 2011; Gourronc et al., 2014; Brunetti et al., 2014; Dębniak et al., 2017). However, these interpreted glacial landforms have been disputed. For example, the observed linear escarpments could either be explained by glacial erosion as trim lines (Gourronc et al., 2014) or by tectonic deformation as fault scarps (e.g., Kissick and Carbonneau, 2019). Fault scarps as discussed by Kissick and Carbonneau (2019) along trough edges of Valles Marineris have been long known. Blasius et al. (1977) were the first to report their occurrences, while Witbeck et al. (1991) were the first to systematically map the spatial distribution of these scarps across Valles Marineris. The relationship between the interpreted fault scarps and nearby fracture zones and fold complexes was analyzed by Yin (2012b), who inferred possible left-slip faulting along the Valles Marineris trough zone. While the faulting hypothesis is a defendable explanation of linear scarps bounding Valles Marineris, nearby landforms resembling U-shaped valleys, arêtes, flow-like valley fills (Rossi et al., 2000; Chapman et al., 2005; Thaisen et al., 2008; Fueten et al., 2011), and widely occurring lobate ridges on trough floors (Dębniak et al., 2017) provide independent support of past glaciation in the Valles Marineris region.

The largest topographic province of the Tharsis rise is represented by the vast plateau plains (4000 km x 6000 km) at intermediate elevations (~3-6 km) (Fig. 1A), which bound high-elevation shield volcanoes to the west and low-elevation troughs to the east (Fig. 1A). The geologic history of the Tharsis plateau plains was recently summarized by Cassanelli and Head (2019) based mainly on early geologic mapping and regional studies predating the availability of sub-meter-resolution images (e.g., Mangold et al., 1988; Watters, 1991; Morris and Tanaka, 1994; Dohm et al., 2001; Anderson et al., 2001; Wilson and Head III, 2002; Tanaka et al., 2014). In their synthesis, Cassanelli and Head (2019) expanded the Tharsis ice-cap hypothesis by invoking supraglacial-lava emplacement as a mechanism of sudden ice-cap melting that caused the formation of the giant circum-Tharsis outflow channels. The Cassanelli and Head (2019) hypothesis predicts coeval glaciation and volcanism during the formation of the Tharsis plateau plains. However, this interpretation is inconsistent with the Late Noachian to Early Hesperian construction of the plateau plains (Tanaka et al., 2014) that predates the Late Hesperian development of the circum-Tharsis outflow channels.

In this study, we test the Tharsis ice-cap hypothesis by addressing whether the intermediate-elevation Tharsis domain has ever been affected by ice-sheet-style glaciation through a systematic analysis of the available highest-resolution (0.25-6 m/pixel) satellite images. Our study area is located at elevations of 2200-6700 m, lies at the western end of Valles Marineris in the central Tharsis rise (Fig. 1A), and covers Oudemans crater (~125 km in diameter) and its surrounding plateau plains (Fig. 1B). This area was selected because the formation of a trough-floor landform assemblage at the western end of Valles Marineris was previously attributed to either regional glaciation (Dębniak et al., 2017) or mega-flooding generated by groundwater expulsion (Rodriguez et al., 2016). In this context, our work not only tests the Tharsis ice-cap hypothesis but also addresses the competing models for the morphological evolution of western Valles Marineris.

2. Geological background

The Tharsis rise may have formed either rapidly in the Late Noachian (~3.8 Ga) (Phillips et al., 2001; Carr and Head III, 2010; Cassanelli and Head, 2019) or slowly from the Late Noachian (~3.8 Ga) to as recently as ~10 Ma (Zuber, 2001; Neukum et al., 2004; Solomon et al., 2005; Nimmo and Tanaka, 2005; Zhong, 2009; Golombek et al., 2010; Yin, 2012a; Tanaka et al., 2014) (Fig. 1A). Its significant topographic relief, spanning from ~<2 km to >20 km in elevation and sitting 2-6 km higher than the surrounding regions, may have been created by the combined effect of igneous and tectonic processes (Solomon and Head, 1982; Neukum et al., 2004; Zhong, 2009; Mangold et al., 2010; Hauber et al., 2011; Yin, 2012a; Yin, 2012b; Tanaka et al., 2014; Richardson et al., 2017; Bouley et al., 2016; Bouley et al., 2018; Cassanelli and Head, 2019; Mouginis-Mark and Wilson, 2019). Specifically, the Tharsis rise formation may have involved magmatic underplating (Carr, 1974; Wise et al., 1979; Mège and Masson, 1996a, 1996b; Harder and Christensen, 1996; Baker et al., 2007; Dohm et al., 2007; Zhong, 2009), juvenile-crust formation (Lillis et al., 2009; Yin, 2012a), thick (5-10 km) volcanic overplating (Solomon and Head, 1982; Reese et al., 2004; Golabek et al., 2011), or modern (Sleep, 1994; Stevenson, 2001) and/or primitive plate tectonics (Yin, 2012a; Yin, 2012b; Dohm et al., 2018).

Oudemans crater is a complex crater bounded by a Hesperian volcanic plateau to the south, Valles Marineris to the east, Noctis Labyrinthus to the west, and a 200 km x 100 km semi-rectangular-shaped basin (referred to as the Triple Intersection Basin in this study) to the north (Fig. 1B) (Tanaka et al., 2014). The crater has a central uplift, a locally terraced-wall zone, and a raised-rim zone (Witbeck et al., 1991; Mest et al., 2011; Caudill et al., 2012; Kasmai, 2014) (Fig. 2). The crater floor lacks alluvial fans, unique for a crater of its size on Mars (Moore and Howard, 2005). The crater-bounding plateau plains also lack layered impact deposits and ejecta rays, which is unusual for a crater of its size on Mars (Mest et al., 2011; Robbins and Hynek, 2011). The northern crater wall and the northern half of the central uplift are missing, which were interpreted as a result of the oblique Oudemans impact (Mest et al., 2011; Osinski et al., 2011; Kasmai, 2014) (Fig. 3).

The central uplift of Oudemans crater exposes light-toned strata that have been interpreted as sedimentary (Bridges, 2006) or volcanic (Caudill et al., 2012) beds. As a general case, material in the central uplift of a complex crater is always brought up to the surface from a deeper crustal level beneath the crater floor (Melosh, 1989). Using an empirical scaling relationship between observed crater diameters and known central-peak excavation depths (Grieve and Pilkington, 1996; Cintala and Grieve, 1998), researchers estimated the central-uplift rocks in Oudemans crater to have been exhumed to the surface from a depth of ~13 km below the crater-bounding plateau plains (McEwen et al., 2010; Mest et al., 2011; Quantin et al., 2012). The crater floor and central uplift expose olivine, pyroxene, and unidentified hydrated mineral phases with weak 1.9 μm H_2O absorption (Caudill et al., 2011; Tirsch et al., 2011; Quantin et al., 2012; Sun and Milliken, 2015). These results suggest that the lithology of the crater floor and central uplift has a mafic composition. Witbeck et al. (1991) interpreted the floor material to have a landslide origin, while Kasmai (2014) considered it to be impact breccias.

Noctis Labyrinthus and Valles Marineris troughs share the same basin floor with that of the Triple Intersection Basin and the Oudemans crater basin (Fig. 1B). Although the shared-floor relationship implies a shared floor-forming origin, no existing work has addressed how this relationship was established. Noctis Labyrinthus trough-floor deposits consist of halloysite/kaolinite, Fe-smectite, Si-OH bearing phases, Fe-sulfates, gypsum, and opal (Weitz et al., 2011, 2013, 2018; Thollot et al., 2012). The origin of the Noctis Labyrinthus troughs was attributed to ground-ice melting (Masson, 1980), graben-wall collapsing (Tanaka and Davis, 1988; Mège et al., 2003), effusive volcanism (Mangold et al., 2010), transient groundwater expulsion (Rodriguez et al., 2016), thermos-karst formation (Baioni and Tramontana, 2017; Baioni, 2018), or exhumation of ancient lava tubes (Leone, 2014). The origin of Valles Marineris troughs have been attributed to rifting (e.g., Carr, 1974; Wise et al., 1979) or left-slip transtensional tectonics (Yin, 2012b).

Many topographic features along Valles Marineris have been interpreted to be glacially generated (Fueten et al., 2011; Mège and Bourgeois, 2011; Gourronc et al., 2014; Brunetti et al., 2014) during west-

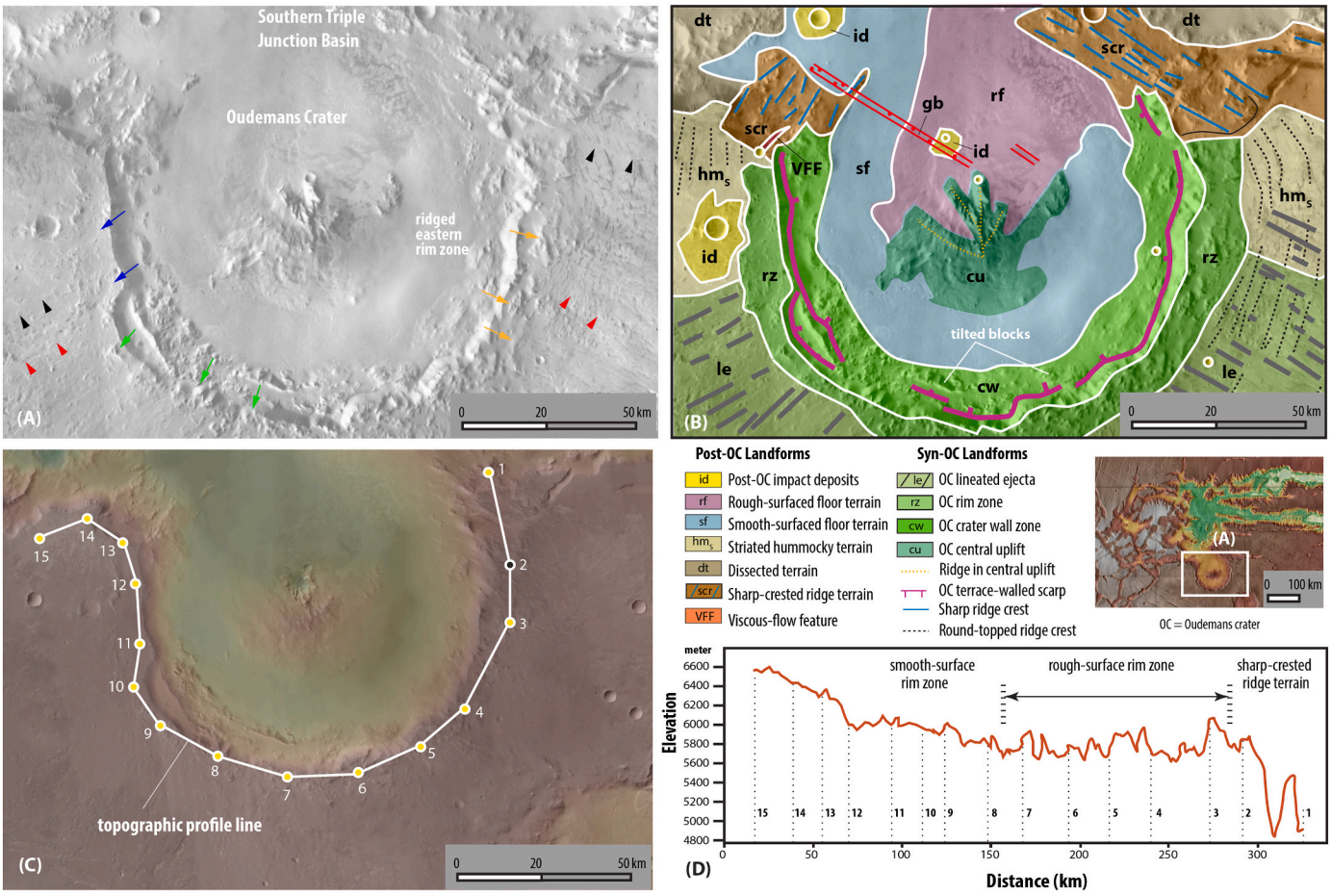

Fig. 2. (A) Uninterpreted and (B) interpreted CTX mosaic image of Oudemans crater (OC). In (A), red arrows indicate radially trending grooves and ridges with a well preserved morphology, whereas black arrows indicate radially trending ridges and grooves with a muted morphology. Also shown in (A) are the western rim zone with a smoother surface and a lack of ridges and knobs (blue arrows), the southern rim zone dominated by knobs (green arrows), and the eastern rim zone exhibiting both knobs and short ridges (orange arrows). Purple arrows mark the sharp-crested ridges in the crater-wall zone. (C) A blended DEM map with the same color scale for elevation as in Fig. 1A. The white polygonal line is the trace of a topographic profile along the rim of Oudemans crater. The numbers are location points corresponding to the topographic profile shown in (D), which displays a smooth-surfaced rim zone in the west, a rough-surfaced rim zone in the south and east, and a ridge-trough rim zone in the northeast. (For interpretation of the references to color in this figure legend, the reader is referred to the web version of this article.)

sourced and eastward-flowing trough glaciation (Brunetti et al., 2014; Dębniak et al., 2017). This notion was challenged by Rodriguez et al. (2016) and Kissick and Carbonneau (2019), who argued that some of the inferred glacial landforms could have been alternatively created by non-glacial processes.

3. Data and methods

To create regional topographic models we made use of the 200 m/pixel blended High Resolution Stereo Camera (HRSC) and Mars Orbiter Laser Altimeter (MOLA) digital elevation model (DEM) (Fergason et al., 2018) (Fig. 1). The blended DEM was superposed over a global mosaic of 100 m/pixel Thermal Emission Imaging System (THEMIS) daytime-infrared images (Edwards et al., 2011; (Fergason, Hare and Laura, 2018) and/or a ~6 m/pixel global mosaic of Context Camera (CTX) images (Dickson et al., 2018) obtained by the Mars Reconnaissance Orbiter (Malin et al., 2007). We performed the above data superposition using the Java Mission-planning and Analysis for Remote Sensing GIS software package (JMARS) of Christensen et al. (2009). The highest-resolution topographic maps were obtained from 1 m/pixel DEMs constructed by the Lunar and Planetary Laboratory at the University of Arizona (Kirk et al., 2008) from stereo images collected by the High Resolution Imaging Science Experiment (HiRISE; McEwen et al., 2007). All data used in this work are publicly available and archived through the NASA Planetary Data System.

We conducted regional geomorphologic mapping and crater counting using JMARS and the beta01 version of the global CTX mosaic constructed by Dickson et al. (2018). As a preliminary dataset, this version of the CTX mosaic has several limitations, chief amongst which is image seaming (see http://murray-lab.caltech.edu/CTX/ under "Limitations of the beta01 Release"). In our mapping, we carefully avoided the issue of mismatched CTX images along the image boundaries. More detailed geomorphologic mapping was conducted using HiRISE images (McEwen et al., 2007, 2010) at resolutions of 25-50 cm/pixel.

Age estimates of the mapped geologic units are based on crater size-frequency distributions using the freely available software *craterstats2* program created by the Planetary Research Group of the Freie Universität Berlin (Michael, 2013). The epoch boundaries used in this study follow that of Michael (2013): >3.94 Ga for the Early Noachian, 3.94-3.83 Ga for the Middle Noachian, 3.83-3.71 Ga for the Late Noachian, 3.71 Ga-3.61 Ga for the Early Hesperian, 3.61-3.37 Ga for the Late Hesperian, 3.37-1.23 Ga for the Early Amazonian, and <1.23 Ga for the Late Amazonian.

Interpreting the formation processes of a mapped landform can be highly nonunique, which is best illustrated by the debate between glacier- vs. non-glacier-generated individual types of landforms in the Valles Marineris region (e.g., Fueten et al., 2011; Mège and Bourgeois,

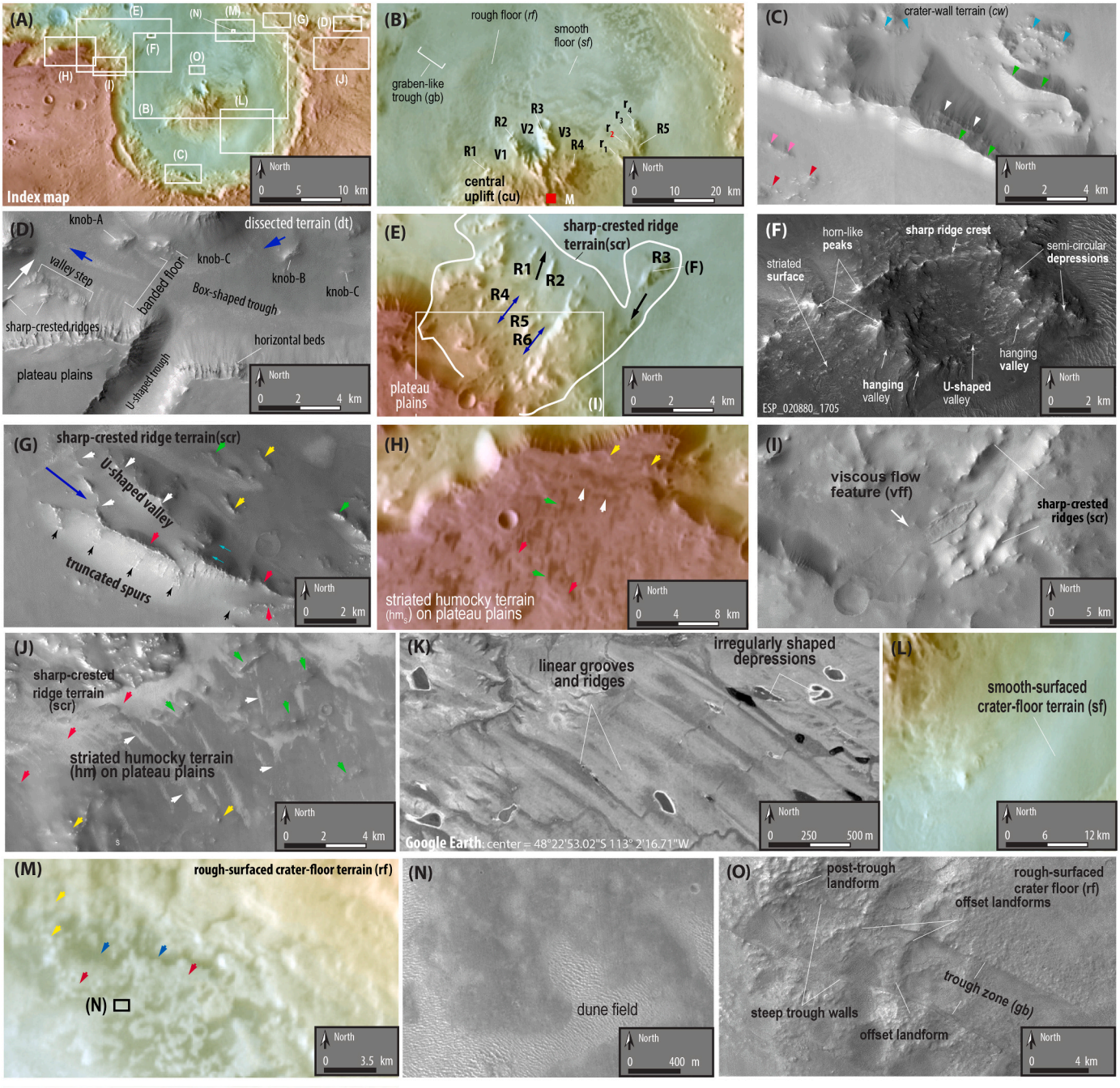

(caption on next page)

Fig. 3. Displays of the mapped geomorphologic units in Fig. 2B using DEM maps (A, B, E, H, L, and M), CTX images (C, D, G, H, I, J, M, and O), a HiRISE image (F), and a Google Earth image (K) for Earth analogue. DEM maps have the same color scale for elevation as in Fig. 1A. (A) A DEM map of the study area and locations of (B) to (J) and (L) to (O). (B) Topographic expression of the central uplift (*cu*), smooth-surfaced crater-floor terrain (*sf*), rough-surfaced crater-floor terrain (*rf*), and a graben zone (*gb*). R1-R5 are major ridges in the central uplift that bound valleys labelled as V1-V3. R1-R4 converge at point M at the southern end of the central uplift. R5 is an isolated ridge that consists of four smaller ridges r1-r4 bounding three smaller valleys. (C) The crater wall terrain (*cw*) consists of sharp-crested ridges (green arrows) exposing tilted beds (white arrows), irregularly shaped ridges topped by knobs (blue arrows), and round-topped ridges draped over by mantling materials (pink arrows). Also shown are clustered and isolated knobs (red arrows). (D) The dissected terrain (*dt*) is dominated by orthogonally terminating troughs bounded by the plateau plains. The trough floor displays linear sharp-crested ridges, valley steps at the intersection of two troughs, trough-parallel bands of different tones, and map-view irregularly or triangularly shaped knobs. The trough cliff faces expose horizontal beds. Blue arrows indicate the interpreted glacier-flow directions. See text for details. (E) The sharp-crested ridge terrain (unit *scr*) is outlined by the solid white line, and a graben zone (unit *gb*) is outlined by an open red rectangular box. Also shown are the locations of (F) and (I). R1-R6 are linear ridges discussed in the text. The white and black arrows indicate interpreted glacial flow directions, whereas the blue arrows indicate possible two phases of glacial flows across the terrain. (F) The sharp-crested ridge terrain that displays landforms resembling those created by valley glaciers: U-shaped hanging valleys, horn-like peaks, blade-like ridge crests, circular depressions, and striated surfaces. (G) The sharp-crested ridge terrain (unit *scr*) northeast of Oudemans crater. In the largest ridge complex shown in this image, minor northwest-trending ridges (white arrows) merge with the main west-northwest-trending ridge (red arrows). This largest ridge complex is bounded in the south by a linear escarpment, expressed by a series of truncated spurs (black arrows). Note that the escarpment is absent away from the range front, suggesting that the formation of the scarp is only related to the location of the ridge complex. The largest ridge complex also displays a southeast-facing valley step (green arrows). Isolated ridges outside the ridge complex have two trends: one parallel (green arrows) and another oblique (yellow arrows) to the main trend of the largest ridge complex. Blue arrow indicates the inferred glacial flow direction. (H) Morphology of the striated hummocky terrain (hm_S) northwest of Oudemans crater. The terrain is dominated by northeast-trending ridges (green arrows) superposed by obliquely trending ridges (red and white arrows). Isolated knobs are present (yellow arrows) along the edges of this terrain. (I) A viscous flow feature (unit *vff*). (J) The main landform features in the northeastern striated hummocky terrain (unit hm_S). This area exposes northeast-trending ridges with a rough-surfaced morphology (green arrows), north- to northwest-trending ridges and troughs (white arrows), and isolated knobs or knob clusters (yellow arrows). A north-facing striated slope forms the diffuse boundary zone between the striated hummocky terrain (unit hm_S) in the south and the sharp-crested ridge terrain (unit *scr*) draped over by a hummocky surface texture in the north (red arrow). Note that the continuous northwest-trending ridges are perpendicular to the local trough margin, whereas the older and discontinuous northeast-trending ridges is oriented perpendicularly and radially to Oudemans crater. (K) Quaternary glaciated landscape expressed as streamlined linear ridges in the southeasternmost Glacier National Park of the western United States. (L) Morphology of the smooth-surfaced crater-floor terrain. (M) Morphology of the rough-surfaced crater-floor terrain. This unit is characterized by linear and curvilinear ridges (red arrows), linear and curvilinear grooves (blue arrows), and irregularly shaped hummocks up to ~100s of meters in size (yellow arrows). (N) A NE-trending ridge with a hummocky surface morphology in the rough-surfaced crater-floor terrain. (O) Linear trough interpreted as a tectonic graben (unit *gb*). See text for details. (For interpretation of the references to color in this figure legend, the reader is referred to the web version of this article.)

2011; Brunetti et al., 2014; Dębniak et al., 2017; cf. Rodriguez et al., 2016; Kissick and Carbonneau, 2019). To identify the most likely landform-formation mechanism, we adopt a holistic landsystem approach (e.g., Evans, 2003). Specifically, we seek to identify a landsystem model that is capable of explaining spatially and temporally related geomorphological elements in a landform association established from geological mapping. Such an approach drastically reduces the uncertainty of interpreting the origin of a single morphological element in the larger hosting landform association. The landsystem approach is further strengthened in this study by adopting process-based geomorphological models constructed from well-documented and well-understood Earth analogues. This approach has been proven effective for unraveling landscape evolution on Mars (e.g., Head et al., 2010; Gallagher and Balme, 2015; Butcher et al., 2016, 2017).

4. Landform mapping of first-order units

We divide the landforms in the study area into the first-order and second-order units. We regard each unit as a landform assemblage consisting of spatially and temporally related constituting morphological elements (Evans, 2003). The first-order units mainly define the general morphology of Oudemans crater and its bounding plateau plains, whereas the second-order units define features distributed within and superposed on top of the first-order units.

First-order landform units are shown in Fig. 2B against an uninterpreted CTX mosaic in Fig. 2A. Definition of each unit is illustrated with CTX and HiRISE images, and in some cases with the assistance of colorized DEM maps in Fig. 3. Below we describe these units and provide preliminary interpretations. More detailed interpretations and proposed landsystem models are given in conjunction with description of second-order landform units.

(1) Lineated Ejecta Zone (*le*) (Fig. 2B). This unit lies at elevations from ~6500 m in the west to ~5500 m in the east on the plateau plains (see *a-a'* and *b-b'* in Fig. 1B). It displays radially trending grooves and ridges (red arrows in Fig. 2A). The striated morphology becomes muted in areas directly northwest and northeast of Oudemans crater (black arrows in Fig. 2A).

Interpretation. Following Mest et al. (2011) and Robbins and Hynek (2011), we interpret the unit to be Oudemans-impact-generated. Muted ejecta morphologies may have resulted from post-Oudemans-impact resurfacing as suggested by Robbins and Hynek (2011).

(2) Crater Rim Zone (*rz*) (Fig. 2B). This unit varies in elevation from ~5300 m in the northwest to ~6700 m in the northeast on the plateau plains (Figs. 2C and 2D), which is consistent with the regional east-sloping plateau surface (Fig. 1B and 1D). The unit terminates at the sharp-crested ridge terrain (unit *scr* and see below for more details) and occurs symmetrically next to the northwest and northeast margins of Oudemans crater (Fig. 2A). The rim-zone morphology varies: the western zone has a smoother surface and lacks ridges and knobs (blue arrows in Fig. 2A), the southern zone consists mostly of knobs (green arrows in Fig. 2A), and the eastern zone is dominated by short ridges (orange arrows in Fig. 2A).

Interpretation. Because the western rim zone is higher than the eastern rim (Figs. 2C and 2D), Oudemans crater may have formed on a preexisting east-sloping plateau surface or a preexisting flat-lying plateau surface that was later tilted. Differentiating the two scenarios has important implications for the style (e.g., uniform vs. non-uniform) and timing (synchronous vs. diachronous) of the Tharsis rise uplifting process. A topographic profile (*b-b'* in Fig. 1B and 1D) shows that the elevation of the crater floor on the two sides of the central uplift is similar. If this crater-floor elevation was created by the Oudemans impact, the above observation implies that the crater was formed on a tilted plateau surface. However, this inference is based on the assumption that the crater-floor elevation has not changed since the Oudemans impact. Because the crater rim is truncated by the sharp-crested ridge terrain (unit *scr*), the Oudemans crater basin must have been modified by post-impact resurfacing processes. Hence, the current elevation of the Oudemans crater floor cannot be used to differentiate the two competing

scenarios for the relationship between the Oudemans impact and the evolution of the Tharsis rise.

(3) Central Uplift (*cu*) (Fig. 2B). This unit varies in elevation from ~2.7 km around the uplift margins to ~5 km in the uplift center. It is surrounded by the smooth-surfaced and rough-surfaced crater-floor units (units *sf* and *rf* in Fig. 2B). The uplift has a half-circled shape (Figs. 2B and 3A) and consists of four ridges (R1, R2, R3, and R4 in Fig. 3B) that radiate northward from the south-central part of the uplift (point *M* in Fig. 3B). The ridges bound three U-shaped troughs that terminate in the south and are open northward (V1, V2, and V3 in Fig. 3B). An isolated northeast-trending ridge lies east of the central uplift (R5 in Fig. 3B), which consists of four smaller north-trending ridges (r_1 to r_4) that bound three smaller U-shaped valleys (Fig. 3B).

Interpretation. Kasmai (2014) attributed the half-circled central uplift to the northward-plunging oblique Oudemans impact. Although the oblique impact hypothesis may explain the general asymmetric shape of the central uplift, it does not explain its detailed morphology expressed by radially trending and sharp-crested ridges that bound U-shaped valleys. It also does not explain the isolated ridge complex (R5) outside the central uplift. We will return to this issue when describing second-order landform units within the central uplift.

(4) Crater Wall Zone (*cw*) (Fig. 2B). This unit varies in elevation from ~2.7 km against the crater basin floor to ~6 km against the crater-rim-bounding plateau plains. The crater-wall zone exposes rim-parallel linear and curvilinear sharp-crested and round-topped ridges (purple arrows in Fig. 2A). Fig. 3C shows that (i) the sharp-crested ridges (green arrows) expose tilted beds (white arrows), (ii) the irregularly shaped ridges have their crests dotted by knobs (blue arrows), and (iii) the round-topped ridges are draped by smooth-surfaced mantling materials (pink arrows). Clustered and isolated knobs also occur next to one another in this unit (red arrows in Fig. 3C). The crater-wall unit is truncated in the northwest and northeast by the sharp-crested ridge terrain (unit *scr*) (Fig. 2B).

Interpretation. Ridges with internally tilted beds are classic expressions of a terraced crater wall (Melosh, 1989). The knobs and their clusters without obvious internal layering may represent impact breccias or more likely post-impact sedimentary deposits. The truncational relationship between the crater wall and the younger sharp-crested ridge terrain (unit *scr*) requires post-Oudemans-impact resurfacing.

(5) Dissected Terrain (*dt*) (Fig. 2B). This terrain varies in elevation from ~4400 m to ~5500 m. The unit is characterized by crater-bounding plateau plains that are dissected by orthogonally terminating U-shaped and box-shaped troughs. The trough walls expose horizontal beds, whereas the trough floors display sub-parallel bands of variable widths and variable albedos (Fig. 3D). The trough floor displays trough-parallel sharp-crested ridges, trough-perpendicular valley steps, and triangularly shaped knobs in map view (Fig. 3D).

Interpretation. Any mechanism for the formation of this terrain must explain (1) the U-shaped and box-shaped troughs, (2) trough-perpendicular valley steps, (3) trough-parallel linear ridges, (4) trough-parallel elongated bands, and (5) triangularly shaped knobs. A fluvial knick zone may explain the valley step in Fig. 3D, but the knick zone migration should have generated fluvial terraces downstream from the valley step (e.g., Bull, 1991; Lavé and Avouac, 2001; Burgess et al., 2012). Because the predicted terraces are not present on the trough floor (Fig. 3D), we consider this interpretation unlikely. Alternatively, the valley step could have resulted from differential fluvial erosion. This mechanism is problematic, because the bedrock exposed on the trough walls is uniformly horizontal and has a uniform surface texture implying a similar rock strength (Fig. 3D) (i.e., the volcanic flow unit of Witbeck et al., 1991). A fluvial origin also fails to explain U-shaped and box-shaped troughs, sharp-crested linear ridges on the trough floor, and alternatingly toned trough-parallel bands on the trough floor. The lack of fault scarps, offset landforms and geologic features, and the mutual termination relationship of troughs (Fig. 3D) do not favor a tectonic origin for this terrain.

We note that the morphology of U-shaped and box-shaped troughs shown in Fig. 3D is similar in cross-sectional geometry to that of tunnel valleys created by subglacial meltwater flow on Earth (e.g., Livingstone and Clark, 2016; also see Fig. 20 and the related text on the Hiawatha crater and the spatially associated subglacial landforms below the Greenland ice sheet). Inspired by this comparison, we propose a subglacial landsystem interpretation for the dissected terrain. This interpretation is capable of explaining the formation of all morphologic elements as listed below. The valley step was induced by a change in the glacial-flow velocity, causing faster erosion below the step and slower erosion above the step (see the right basal side of Fig. 8I) (see chapter 7 in Cuffey and Paterson, 2010 for the related physics). The step then became a cavity zone across which the flowing glacier plucked the rock on the lee side of the step under a high pore-fluid-pressure condition (Iverson, 2012). This interpretation implies a down-step flow direction (white arrow next to the step in Fig. 3D). The linear ridges on the trough floor may represent glacially streamlined subglacial tills (e.g., Clark, 1993), or glacially streamlined bedrock ridges (e.g., Krabbendam et al., 2016). The trough-parallel bands may represent a streamlined debris-rich valley glacier such as those associated with the Malaspina glacier system in southeast Alaska (e.g., Sharp, 1958). The map-view triangularly shaped knobs may represent drumlins (knob-A and knob-B) or whaleback features (knob-C and knob-D) (Fig. 3D) generated by streamlining of subglacial tills during glacial flow .

(6) Sharp-Crested Ridge Terrain (*scr*) (Fig. 2B). This terrain dominated by blade-like ridges occurs symmetrically next to the northwest and northeast corners of Oudemans crater. Its elevation varies from ~3200 m to ~5600 m in the area directly northwest of Oudemans crater and from ~2500 m to ~5000 m in the area directly northeast of Oudemans crater. The terrain northwest of Oudemans crater displays shorter ridges that are linearly aligned and parallel to the longer ridges (Fig. 3E). Map-view shapes of the shorter ridges include unidirectionally pointing/narrowing (R1, R2, and R3) or bi-directionally pointing/narrowing (R4, R5, and R6) terminations (Fig. 3E). A more detailed view of the R6 feature in Fig. 3E with the aid of a HiRISE image (ESP_020880_1705) in Fig. 3F shows that the sharp-crested ridge terrain hosts U-shaped troughs, U-shaped hanging valleys, horn-like peaks, arête-like ridge crests, and cirque-like circular depressions (Fig. 3F).

The terrain directly northeast of Oudemans crater (Fig. 3G) hosts U-shaped valleys, minor ridges (white arrows) trending obliquely to the main ridge (red arrows) in the largest ridge complex displayed on this image, linear escarpments (black arrows), and valley steps (narrower green arrows). Interestingly, isolated and shorter ridges in this terrain trend obliquely to one another, with one set parallel (wider green arrows in Fig. 3G) and another set (yellow arrows in Fig. 3G) oblique to the main ridge in the largest ridge complex

Interpretation. Because this terrain truncates the crater-rim and crater-wall zones, its development must postdate the Oudemans impact and have contributed to the morphological modification of the Oudemans crater basin. The sharp-crested linear ridges could have been generated by faulting or erosion. For example, the linear trace of the truncated spurs shown by black arrows in Fig. 3G could represent a fault

scarp. Because the scarp bounds the ridge complex in the north against a plain to the south, the inferred fault should have postdated both the ridge complex and the plain deposits. This age relationship requires that the "fault" cuts through the plain deposits with a scarp-like morphological expression along its projected trace. As shown in Fig. 3G, the scarp is restricted to the base of the ridge and does not extend laterally into the plain deposits, which rules out a tectonic origin. Additionally, the fault-scarp-like feature only occurs along the base of one sharp-crested ridge, which suggests that faulting cannot be invoked as a general mechanism for the formation of all ridges in this terrain. Fluvial and aeolian origins are also unlikely, because they are not known for creating linear escarpment, sharp-crested ridges, and U-shaped troughs.

Morphological features resembling the classic glacial landforms on Earth (e.g., U-shaped hanging valleys, horns, and cirques shown in Figs. 3F and 3G) led us to suggest that the sharp-crested ridge terrain was generated by glaciation. In this interpretation, the local linear escarpment represents a glacier-induced trim line, U-shaped troughs represent glacier trunk valleys and tributary hanging valleys, sharp-crested ridges represent arêtes, circular depressions represent cirques, striated surfaces resulted from glacial streamlining and basal abrasion, and valley steps represent sites across which the basal glacial flow velocity increased rapidly causing faster erosion below the step (see the right side of the glacier base in Fig. 8I and related discussion).

In the sharp-crested ridge terrain northwest of Oudemans crater, features R1, R2, and R5 in Fig. 3E display a northeastward-narrowing ridge shape. We interpret this map-view ridge shape to have resulted from subglacial streamlining, which implies a northeastward glacial flow as shown by the white arrow in Fig. 3E. In contrast, R3 displays a southwest-narrowing map-view ridge geometry, which implies a southwestward glacial flow (black arrow in Fig. 3E). Features R4 and R6 appear to be symmetric at the two ends, which may have been created by superposition of northeastward and southwestward glacial flows (blue arrows in Fig. 3E). The above interpretation implies that the sharp-crested ridge terrain northwest of Oudemans crater may have been created by *two phases of glacial flows that moved in opposite directions*.

In the sharp-crested ridge terrain northeast of Oudemans crater, the main ridge complex shown in Fig. 3G has a southeastward narrowing map-view shape, indicating a southeastward-flowing glacier (blue arrow in Fig. 3G). This inferred glacial-flow direction is consistent with the southeastward valley-step facing direction that also indicates a southeastward glacial flow. The two ridge trends in this area may suggest two phases of glacial flow in different flow directions.

(7) Striated Hummocky Terrain (hm_S) (Fig. 2B). This unit occurs symmetrically on the plateau plains next to the northwest and northeast rims of Oudemans crater. It has an elevation range of ~6200-6400 m (Fig. 2B), and is characterized by round-topped linear ridges on an undulating surface (Figs. 2A and 2B). The terrain northwest of Oudemans crater is dominated by northeast-trending ridges (green arrows in Fig. 3H) superposed by shorter and narrower northwest-trending transverse ridges (red and white arrows in Fig. 3H; also see discussion on this feature in more details related to Figs. 17 and 18). This unit also displays isolated knobs (yellow arrows in Fig. 3H), and is the source of a viscous flow feature similar to those defined by Milliken et al. (2003) (*VFF* in Fig. 3I) (see Figs. 3A and 3E for location of Fig. 3I).

The striated terrain northeast of Oudemans crater displays sparsely distributed northeast-trending ridges with a rough-surfaced morphology (green arrows in Fig. 3J). The northeast-trending ridges are cut by north- to northwest-trending ridges and troughs (white arrows in Fig. 3J) that dominate this terrain. The terrain also displays isolated knobs or knob clusters (yellow arrows in Fig. 3J). A north-facing striated slope forms the boundary zone between the striated hummocky terrain in the south and the sharp-crested ridge terrain locally associated with a hummocky-surface texture in the north (red arrow in Fig. 3J; the white dashed line marks the boundary between units *scr* and hm_S). Note that continuous and dominant northwest-trending ridges are perpendicular to the local trough margin, whereas the older and discontinuous minor northeast-trending ridges are parallel to the radially trending ejecta rays.

Interpretation. The parallel ridges and grooves in the striated hummocky terrain could have been generated by impact, aeolian, fluvial, tectonic, or glacial processes. We rule out the impact-origin because (1) the dominant northwest-trending ridges are not oriented radially emanating from Oudemans crater, and (2) the northwest-trending striation ridges in fact cut the radially trending ridges. Parallel northwest-trending ridges might have been generated by fluvial processes, but the lack of point bars, cutbacks, and dendritic V-shaped valleys makes this interpretation unfavorable. Tectonic faulting could also have created parallel ridges, which would require offset landforms that are not observed at the resolution of CTX images.

Parallel ridges in the striated hummocky terrain could have been created by aeolian erosion, such as through the formation of yardangs (e.g., Inbar and Risso, 2001; Kapp et al., 2011; Dong et al., 2012; Pullen et al., 2018; Pelletier et al., 2018; Ding et al., 2020). Yardangs have been documented on Mars (e.g., Ward, 1979; Zimbelman and Griffin, 2010) and the presence of dune fields in the study area suggests active winds, and the available sand could drive aeolian erosion. However, this mechanism does not explain (1) the occurrence of transverse ridges (Fig. 3H), (2) diverging and curvilinear ridge trends (Fig. 3J), (3) scattered knobs on striated surfaces (Figs. 3H and 3J), and (4) the hummocky surface that hosts the striation ridges (Fig. 2A; also see more detailed description of this unit related to description and discussion of Figs. 15, 17, and 18 below).

Glacier-generated linear ridges commonly occur on hummocky surfaces and are associated with transverse ridges with a washboard-like landform pattern (e.g., Stokes et al., 2006; Cline et al., 2015). Accordingly, we suggest that the flat- to round-topped ridges represent streamlined subglacial mega-scale glacial lineations (MSGLs), transverse ridges represent ribbed moraines (Clark, 1993; Clarke, 2005; Evans et al., 2006), and the isolated mounds represent supraglacial tills deposited as kames (e.g., Brodzikowski and Van Loon, 1987). An Earth analogue from southeasternmost Glacier National Park of the western United States (Alden, 1914) displays striated and streamlined landforms (Fig. 3K), similar in morphology to those displayed in the striated terrain. More observational details on the interpreted MSGLs will be presented in the Discussion section.

(8) Smooth-Surfaced (*sf*) and Rough-Surfaced (*rf*) Crater-Floor Terrains (Fig. 2B). These two terrains surround the central uplift and have an elevation range of ~2200-2700 m. The smooth-surfaced terrain is characterized by a long-wavelength (>5 km) undulating surface with a homogenous surface texture (Fig. 3L). In contrast, the rough-surface unit is characterized by diverse surface features including linear and curvilinear ridges (red arrows in Fig. 3M), linear and curvilinear grooves (blue arrows in Fig. 3M), and interconnected groove and ridge networks. The rough-surface unit also displays hummocks up to ~100s m in size (yellow arrows in Fig. 3M). Ridges in the rough-surfaced unit (*rf*) are typically round-topped and have a hummocky surface texture (Fig. 3N).

Interpretation. Following Witbeck et al. (1991) and Kasmai (2014), we attribute the general morphology of the crater floor to have been generated by the Oudemans impact. However, the Oudemans impact process alone does not explain the widely occurring hummocks and complex curvilinear groove-ridge networks. Rather, younger resurfacing event must have modified the original Oudemans impact-crater-floor morphology (see below).

(9) Linear Troughs (*gb*) (Fig. 2B). Linear troughs occur across the mapped area and trend dominantly to the northwest. The most prominent linear trough in the study area is exposed on the Oudemans crater floor (Fig. 3O). The walls of this northwest-trending trough are defined by linear scarps that cut and offset hummocky landforms (Fig. 3O). The trough-bounding scarps in turn are overlain by younger hummocky-surfaced landforms (Fig. 3O). This relationship requires trough formation to have occurred between two phases of hummocky-terrain development. Because hummocky landforms are commonly associated with glaciation (Hambrey et al., 1997; Eyles et al., 1999), the above observation suggests that extensional tectonics and glaciation were generally synchronous on the floor of Oudemans crater.

(10) Post-Oudemans Impact Craters and Related Deposits (unit *id* in Fig. 2B). Small craters (1-3 km in diameter) are scattered across the mapped area; many display fresh crater morphologies characterized by well-preserved raised rims and locally preserved ejecta deposits.

Summary of the first-order units in the study area. We divide the first-order units to those created by the Oudemans impact processes and those generated by post-Oudemans impact processes. The impact-induced units include the central uplift, crater-wall zone, crater-rim zone, crater-ejecta zone, and crater floor. Post-impact units include the interpreted glacier-generated striated hummocky terrain on the plateau plains, dissected terrain, and sharp-crested ridge terrain.

5. Landform mapping of second-order units

5.1. Central uplift

The central uplift (Fig. 4A; cf. Fig. 4B) exposes the following units: (1) U-shaped trunk valley terrain (unit *tv*), (2) bedrock-ridged terrain (unit *br*), (3) ridge-cutting valley terrain (unit *rcv*), (4) hummocky terrain (unit *hm*), (5) horn-like summits (*sm*), (6) lobate ridges (*lb*), and (7) irregularly shaped depressions (unit *ird*). Fig. 4B shows a trunk valley (*feature 1*) bounded by a low-relief (*feature 2*) and high-relief (*feature 3*) ridged terrains. The western trunk-valley margin is diffuse and irregular, which is defined by a transitional boundary between the low-relief ridged terrain and a smooth-surfaced valley-floor terrain (white dashed line between *features 1 and 2* in Fig. 4). In contrast, the eastern valley margin (marked by dark blue arrows in Fig. 4B) is sharply defined by a trace of linearly aligned scarps between the bedrock ridged terrain and the smooth-surfaced valley-floor terrain. The scarp trace extends southeastward and links with the northern margin of a spoon-shaped valley (yellow arrows in Fig. 4B). The southeastern end of the northwest-opening spoon-shaped valley is a ridge that exposes a section of light-toned beds that do not show any sign of fault offsets (green arrows in Fig. 4B).

The high-relief ridged terrain (*feature 3*) east of the trunk valley (*feature 1*) hosts features resembling U-shaped hanging valleys (orange arrows), horns (white arrows), and arêtes (red arrows) (Fig. 4B). The U-shaped hanging valleys (orange arrows) intersect the main trunk valley (*feature 1*) at acute angles pointing southward (Fig. 4B). Valleys and lower-elevation regions south of the hanging and trunk valleys host round-topped smooth-surfaced lobate ridges that are convex southward (light blue arrows of various widths in Fig. 4B).

We further analyzed the second-order units using a 1 m/pixel HiRISE DEM created by the HiRISE team (Fig. 5A), which was coupled with mapping on a correlated HiRISE image (ESP_026194_1700) at a resolution of 25 cm/pixel (Fig. 5B). The combined effort reveals (Figs. 6A and 6B): (1) high-relief *round-topped bedrock ridges* (southern part of unit *scr* in Fig. 5C) are associated with lighter-toned, thinner-bedded, and finer-grained-like beds displaying alternating light and dark tones (Fig. 6C), (2) high relief *sharp-crested bedrock ridges* (northern part of unit *scr* in Fig. 5C) are associated with darker-toned, thicker-bedded, and coarser-grained-like beds (Fig. 6D), and (3) low-relief *valley-floor hills and mounds* (unit *bh* in Fig. 5C) are associated with massive (Fig. 6E) or crudely bedded (Fig. 6F) boulder-bearing materials.

Fig. 7 shows the main geomorphologic features along a north-trending trough in the central uplift of Oudemans crater. Two areas (see the index map of Fig. 7) display map-view triangular landforms with south-pointing terminations. Fig. 7A shows the southern trough-floor area that exposes triangular landforms. There, a north-trending ridge bounding the west side of the valley consists of a sharp-crested segment in the north (yellow arrows) and a round-topped segment in the south (green arrows). The change in ridge morphology corresponds to the change in the bedrock surface texture and bed thickness as described above: the sharp-crested ridge segment is associated with a dark-toned thicker-bedded and coarse-grained-like sequence hosting a U-shaped hanging valley (red arrow) and a horn-like peak (purple arrow) (Fig. 7A), whereas the round-topped ridge segment is associated with a lighter-toned thinner-bedded and finer-grained-like sequence lacking hanging valleys and horn-like peaks. Both the round-topped and sharp-crested ridges display steeply dipping beds (blue arrows in Fig. 7A). The eastern side of the trough exposes smooth-surfaced bedrock outcrops characterized by alternating dark- and light-toned bands, which are interpreted as bedding (white dashed lines in Fig. 7A).

The trough floor shown in Fig. 7A displays a south-pointing triangular landform and several lobate ridges numbered as 1 to 5 (cf. Fig. 7B). Lobate ridge 1 in Fig. 7A is superposed by a younger set of northeast-trending striations (solid orange lines). The triangular landform exposes alternating light- and darker-toned bands (blue arrows in Fig. 7C) similar to those exposed at bedrock outcrops. The surface of the triangular landform is striated (yellow arrows in Fig. 7C), scattered by dark-toned boulders a few meters in size (white arrows in Fig. 7C), and topped by three linear ridge crests forming a triple-junction-like pattern (red arrows in Fig. 7C).

Nearby lobate ridges are flat-topped, bound interior depressions (Fig. 7D), and expose unconsolidated boulder deposits (Fig. 7E). The sequence of lobate-ridge development is inferred based on their cross-cutting relationships. The emplacement directions of the lobate ridges are interpreted from their map-view shapes (Fig. 7A; cf. Fig. 7B).

Fig. 7F shows a triangular landform consisting of several smaller triangular ridges covered by striated surfaces (white arrows in Fig. 7F). The large and small triangular features all have a south-pointing shape (tips are indicated by red arrows) (Fig. 7F). Alternating dark- and light-toned bands interpreted as bedding cut across the crest of a smaller triangular landform (blues arrows in Figs. 7F and 7G). One of the smaller triangular ridges at the southern toe of the larger triangular landform (Fig. 7F) is composed of massive-textured boulder deposits (Fig. 7H).

Fig. 8A shows interpreted features along the same north-trending trough as shown in Fig. 7 (see the index map on the left side of the figure for location). The trough floor displays a north-facing valley step (orange dashed line) from which several north-plunging ridges are emanated (blue lines in Fig. 8A). South of the valley step is an isolated boulder-bearing mound (purple arrow), whereas northeast of the valley step is a southward-pointing triangular ridge (large red arrow). This triangular ridge exposes alternating dark- and light-toned bands interpreted as bedding (white dashed lines) (Fig. 8A). The triangular-ridge landform exposes northwest-trending ridges (red arrows in Fig. 8A) on the north side and smaller northeast-trending ridges (yellow lines in Fig. 8A and white arrows in Fig. 8B; also see Fig. 8C) on the southwest side. Because the two sets of linear landform fabrics do not overlap, their cross-cutting relationship is unknown.

The northeast-trending linear ridges and grooves on the southwest side of the larger triangular ridge are constructed on top of bedrock. These ridges cut obliquely across the underlying beds and terminate at a ridge in the north (Figs. 8A and 8C). On the opposite north side of the ridge crest, the bedrock surface is dotted by boulders and broken bedrock where no clearly defined striations are present (Fig. 8D). We note that both minor northeast-trending striations and major northwest-

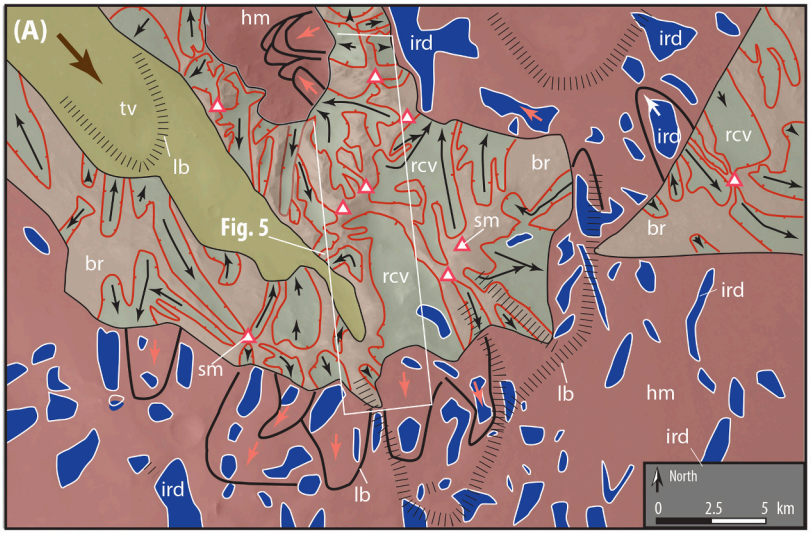

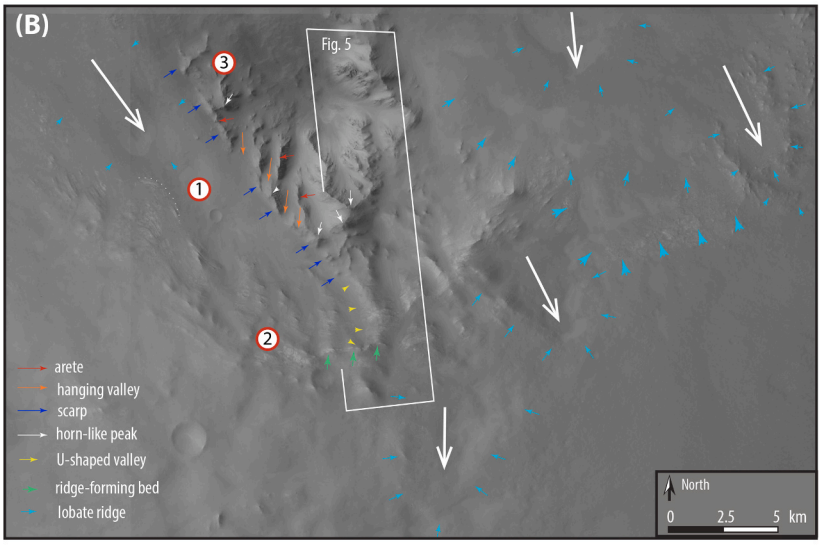

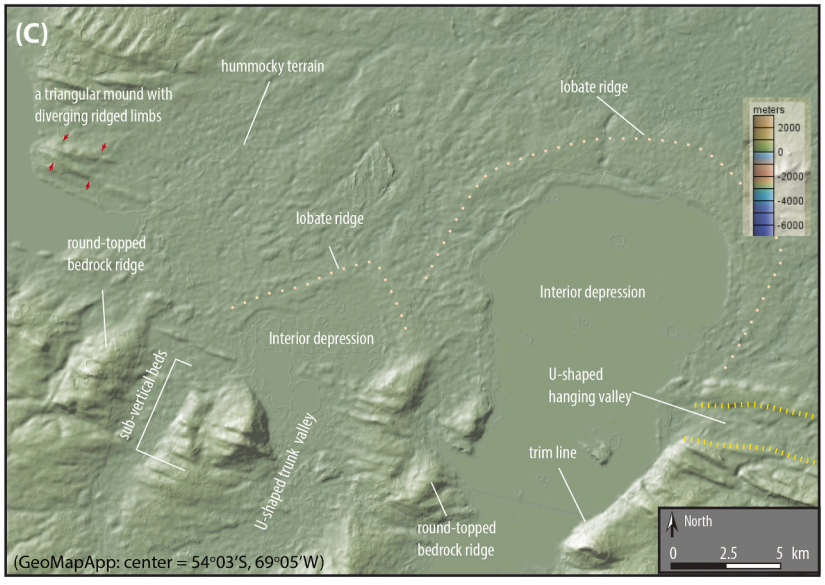

Map Symbols

tv
U-shaped trunk valley

rcv
U-shaped ridge-cutting -valley terrain

hm
Hummocky terrain

br
Bedrock ridged terrain

Horn-like summit (sm)

Ridge-cutting-valley boundary (red line) and inferred glacial flow direction (black arrow)

Irregularly shaped depression (ird) mostly in the hummocky terrain

Round-topped lobate ridge (left) and boulder-bearing piedmont lobate ridges (right) (lb) with arrows indicating protrusion direction

Interpreted glacial-flow direction along main trunk valleys

① Trunk valley

② Low-relief ridge terrain

③ High-relief ridge terrain

(caption on next page)

Fig. 4. (A) A geomorphological map created from a CTX mosaic image in (B). Light blue arrows with various sizes and line thickness: lobate ridges; dark blue arrows: escarpment interpreted as a glacier trim line; orange arrows: hanging valleys in a high-relief ridge terrain (feature 3) that intersect a trunk valley (feature 1) at an acute angle pointing southward. Interpreted trim line (dark blue arrows) truncates hanging valleys and ends at a spoon-shaped valley (yellow arrows) bounded by a low-relief ridge terrain (feature 2). The southern edge of the spoon-shaped valley exposes bedding along a ridge (green arrows) that is continuous without being offset by faulting. The high-relief ridge terrain displays horn-like features marked by white arrows. The large white arrows indicate the interpreted glacier-flow directions based on the shape of lobate ridges and intersection-angle relationships between the trunk valley (feature 1) and hanging valleys. (C) An Earth-based DEM map created using GeoMapApp software. The map displays a glacier landsystem in the Patagonia ice field that has many features comparable to those exposed in Oudemans crater. See text for details.

trending ridges do not cut into the valley-floor deposits (Fig. 8A), which suggests that the deposition of the valley fill postdates the striation and ridge development.

Fig. 8E shows interpreted landform fabrics in a mountainous area of the central uplift (cf. Fig. 8F and see the index map on the left for the location of this image). In the area, north-trending striations are exposed on a bedrock ridge and cut obliquely across steeply dipping beds (Fig. 8E; cf. Fig. 8F). A map-view teardrop-shaped landform displays a steeper upslope ridge surface where it exposes layered bedrock and a gentler downslope ridge surface where it exposes unconsolidated boulders (Fig. 8D; cf. Fig. 8E). This landform narrows downhill to the northwest.

Interpretation. Formation of major north-trending ridges and troughs in the central uplift was attributed to Oudemans-impact-induced faulting by Kasmai (2014). Although the ridge-bounding linear escarpment in Fig. 4B (blue arrows) alone could be interpreted as a fault trace, placing this feature in a larger geologic context makes this interpretation unlikely. This is because (1) the "fault trace" terminates at a spoon-shaped valley (yellow arrow in Fig. 4B) where no clear fault-scarp-like features can be identified, and (2) the projected "fault trace" does not produce observable offset of landforms or layered bedrock materials (green arrows in Fig. 4B).

Alternatively, the trunk valleys in the central uplift could be explained by fluvial processes, such as mega-floods (e.g., Carling et al., 2009). Mega-floods should produce vortices that in turn should generate kolk pits, plunge pools, cataracts, and butte-basin landforms (e.g., Carling et al., 2009), which are absent in the central-uplift area.

Aeolian processes could be invoked to explain local landforms in the central uplift, such as the map-view triangular landforms on trough floors. Specifically, they may be interpreted as whaleback yardangs (e.g., Li et al., 2016). However, the nearly equal-dimensional shape of the triangular landforms, their striated surfaces, their isolated occurrences, and the hierarchical nature of larger triangular landforms hosting smaller triangular landforms are all inconsistent with yardangs created by aeolian erosion on Earth (e.g., Dong et al., 2012; Li et al., 2016).

The lobate ridges in Fig. 7A could have been generated by volcanic lava flows (e.g., Tanaka et al., 2014), which would require the ridges to be composed of fine-grained materials (i.e., <mm-scale grains), not resolvable at the spatial resolution of HiRISE images (25 cm/pixel). This interpretation requires eruption sources at the end of the lobate ridges. The boulder-like ridge composition and the lack of eruption sources at the ends of the lobate ridges do not favor this interpretation.

We find that a subglacial landsystem model could explain the formation of all the observed second-order landform units in the central uplift. Specifically, horn-like peaks, cirque-like depressions, and U-shaped trunk and hanging valleys may have all resulted from glaciation, and the lobate ridges may have formed as recessional moraines (e.g., Chandler et al., 2016). In our glacial interpretation, the southward-tapering triangular landforms in Figs. 7A and 7F may have resulted from subglacial streamlining processes, and their south-pointing shape suggests a southward glacial flow in the upslope direction of the north-sloping north-trending trough (large yellow arrows in Figs. 7A and 7F). This flow direction is consistent with that indicated by the nearby lobate ridges (Fig. 7A). As shown in Fig. 4B, the shape of the lobate ridge in a trunk valley (*feature 1*) and the pointing direction of acute intersection angles between the trunk valley and several feeder hanging valleys (orange arrows) also require a southward glacial flow. Taken together, the first-order glacial-flow direction across the central uplift of Oudemans crater was southward.

At a local scale, however, the inferred glacier-flow directions are complex. For example, the north-facing valley step in Fig. 8A requires a northward glacial flow (blue arrow in Fig. 8A). Because the valley fill truncates the striated landforms on the east side of the step, we suggest that this northward glacial flow (large blue arrow) is the youngest event as shown in Fig. 8A. Note that the nearby triangular bedrock ridge with a southward pointing tip requires a southward glacial flow (red arrow in Fig. 8A). In addition, a northeastward glacial flow (yellow arrow in Fig. 8A) is indicated by the paired striated unbroken-bedrock (north slope) and un-striated broken-bedrock (south slope) surfaces (Figs. 8C and8D). The features resemble the stoss (upslope = south slope) and lee (downslope = north slope) sides of a roche moutonnée on Earth (Sugden et al., 1992; Hall et al., 2020). A possible process for the formation of a roche moutonnée is shown in Fig. 8G.

The map-view teardrop-shaped ridge in Fig. 8E (cf., Fig. 8F) and the triangular landform in Fig. 7F are characterized by bedrock on the wider and steeper sides and boulder deposits on the narrower and gentler sides of the ridges. This asymmetric morphology and its association with bedrock vs. unconsolidated deposits resemble a crag-and-tail feature on Earth (Jansson and Kleman, 1999; Dowdeswell et al., 2016). As shown in Fig. 8H, the morphology of the bedrock and boulder-bearing landforms requires the glacial flow from the steep-slope side towards the gentle-slope side in the northwest direction.

The isolated ridge at the southern tip of the larger triangular landform in Fig. 7F could represent a drumlin composed of only a boulder material (Fig. 7H). A possible shape of a drumlin in cross section and map view is shown in Figs. 8I and 8J. We envision that the valley step was induced by faster basal glacial flow on the down-flow side of the step and slower basal glacial flow on the up-flow side of the step (see chapter 7 in Cuffey and Paterson, 2010 for the physics related to velocity-dependent glacial erosion rates). This change in flow velocity requires extension of the ice sheet directly above the step, which in turn would favor the formation of an extensional-fracture fracture system cutting downward through the flowing ice sheet. Isolated boulder mounds on the trough floor could have formed by deposition of supra-glacial debris transported through these extensional fractures that locally reached the base of the flowing ice sheet.

The cross-cutting relationship among lobate ridges and triangular landforms shown in Fig. 8A (cf. Fig. 8B) suggests the following sequence of events: (1) southward flow creating the south-pointing streamlined bedrock landform (red arrow for the flow direction), (2) northeastward flow creating a roche moutonnée (yellow arrow for the flow direction), and (3) northwestward flow creating the valley step and northwest-trending valley-floor ridges (blue arrow for the flow direction). For topographically unconstrained glaciation (e.g., Antarctica and Greenland ice sheets), the glacial-flow direction is controlled by the overall gravitational-potential gradient expressed by the regional glacier-surface slope (e.g., p. 295 in Cuffey and Paterson, 2010). In this sense, the complex glacial flow directions inferred above may have resulted from a combination of time- and space-varying glacier-accumulation rates that control the spatial distribution of the gravitational potential-energy gradient of the flowing ice sheet. This physical concept readlily explains the upslope glacial flow as required by our observations shown in Figs. 4B, 7A, 7F, and 8A. In contrast, the complex glacial flow directions in the mountainous area may have been associated with

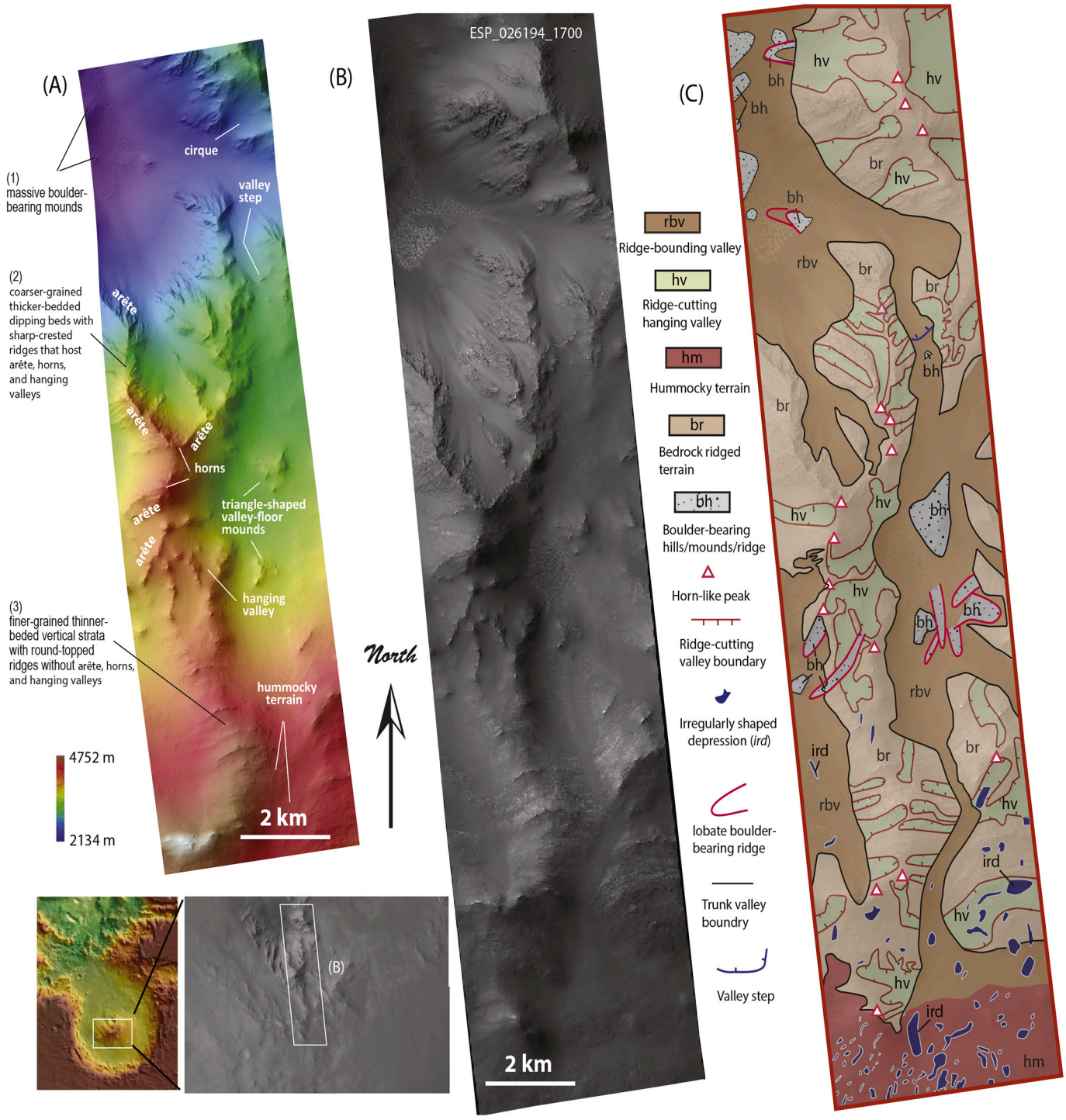

Fig. 5. (A) A HiRISE DEM image (DTEEC_026339_1700_026194_1700_U01) created by the HiRISE team. Correlation between ridge morphology and three types of rocks: (1) massive boulder-bearing rocks host trough-floor mounds and hills, (2) thick-bedded coarse-grained dark-toned beds host sharp-crested ridges, and (3) thinner-bedded finer-grained lighter-toned beds host round-topped ridges. Also shown are landforms resembling arêtes, hanging valleys, and horns in glaciated regions on Earth. (B) HiRISE image ESP_026194_1700 corresponding to the aerial coverage of the DEM map in (A). (C) Interpreted geomorphologic map highlighting key morphologic units based on mapping on the HiRISE image ESP_026194_1700 shown in (B).

the terminal stage of deglaciation when glacial flows were controlled by local topography.

Round-topped bedrock ridges (Fig. 5A) composed of alternating dark- and light-toned bands (Fig. 6C) in the central uplift lack hanging valleys and arête-like crests. This morphology appears to contradict our glacier-induced landform-formation interpretation. On Earth, round-topped ridges lacking hanging valleys and arête do occur in glaciated mountainous terrains as exemplified by landforms in the Patagonia ice field (Fig. 4C) (Bendle et al., 2017). There, round-topped ridges bounding U-shaped glacier trunk valleys are associated with (1) vertical beds trending perpendicular to the glacial-flow direction, (2) trim-line scarps, (3) lobate ridges in the piedmont plains, and (4) triangular landforms on trough floors (see Fig. 4C). All of the aforementioned features are similar in forms to those associated with the round-topped

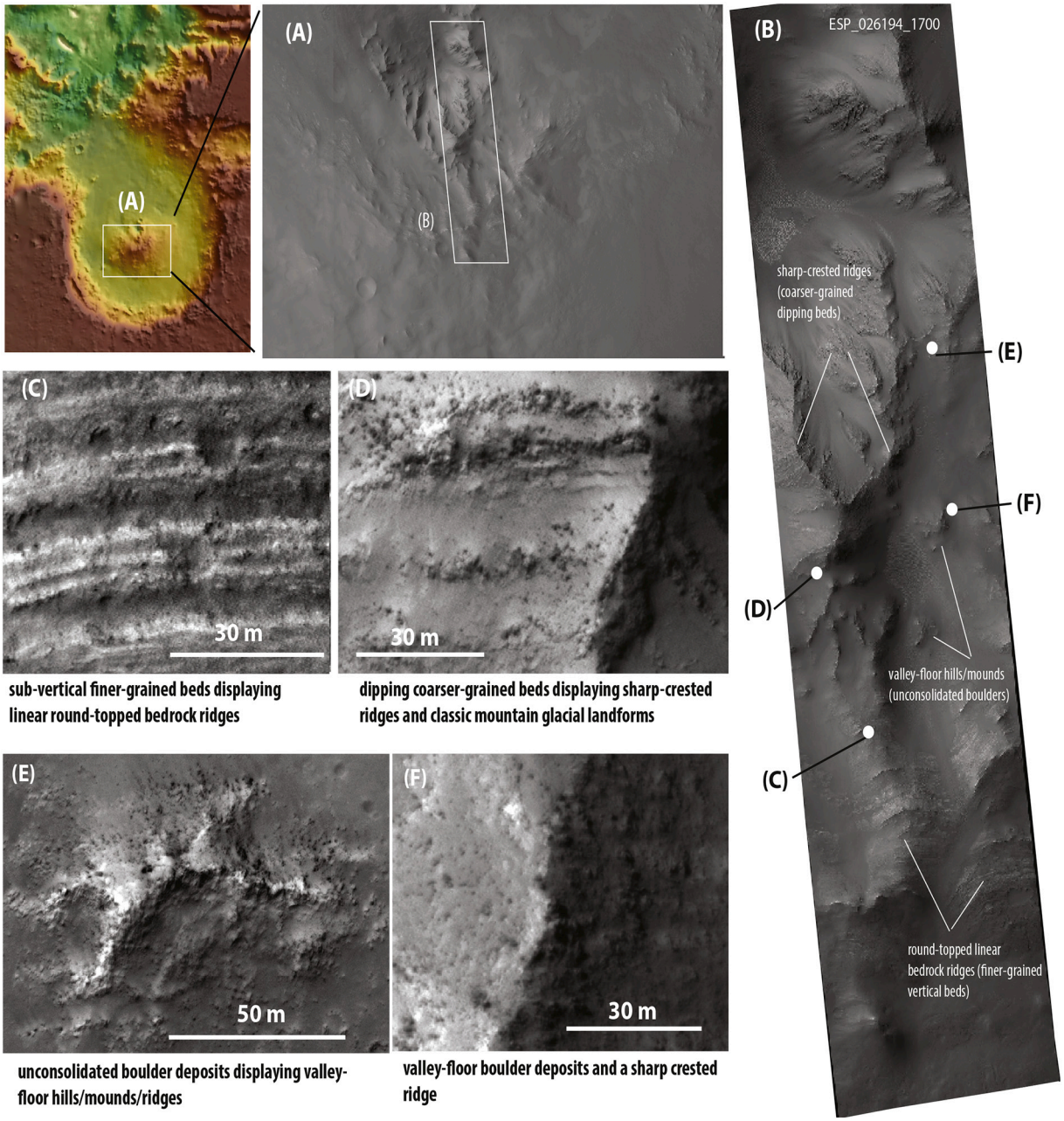

Fig. 6. (A) and (B) show locations of (C)-(F) in this figure. (C) Finer-grained thinner-bedded light-toned dipping beds host low-relief round-topped ridges. (B) Coarser-grained thicker-bedded and dark-toned dipping strata host high-relief sharp-crested ridges and valley-glacier-like landforms. (E) Unconsolidated massive boulder-bearing materials host low-relief mounds. (F) Unconsolidated boulder deposits host a low-relief ridge on the valley floor.

ridges in the central uplift ((Fig. 7). Based on the above comparison, we suggest that whether glaciated ridges hosting or not hosting valley-glacier-induced landforms on Earth or Mars depends on the mechanical strength of the hosting bedrock. As shown in our mapped area, it appears that weaker bedrock expressed by a round-topped ridge morphology was incapable of creating the aforementioned valley-glacier-induced landforms. This may explain the lack of cirques and hanging valleys in the trough-wall terrain of Valles Marineris (Gourronc et al., 2014).

5.2. Crater floor

We divide the crater floor into the northern, western, eastern, and southern/southwestern areas. Below we describe their morphologic characteristics and discuss possible landform-formation mechanisms.

(1) Northern Crater-Floor Area. Our mapping (Figs. 9A and 9B) reveals a rough-surfaced ridge terrain (unit *rsr*) in which irregularly shaped ridges are bounded by dune-filled depressions. The ridge surfaces display decameter- to meter-scale knob-like hummocks (white arrow) and minor curvilinear ridges (yellow arrow) parallel to the larger and darker-toned hosting ridges (blue arrows in Fig. 9C). The northern floor area (Fig. 9D) also exposes post-Oudemans impact craters and the related impact deposits (unit *fct*) (white arrows). The impact features are emplaced on top of lobate ridges (*lb*) (yellow arrows) that have interior depressions (blue arrow). Additionally, the northern crater floor exhibits a linear-knob terrain (kb_L) (red arrow in Fig. 9B) and a flat-topped ridge terrain (*ftr*) (dark blue arrow in Fig. 9B). Hummocky terrains in the area occur either on a relatively flat and smooth surface (hm_F) (Fig. 9E), or on an undulating surface (hm_U) that is

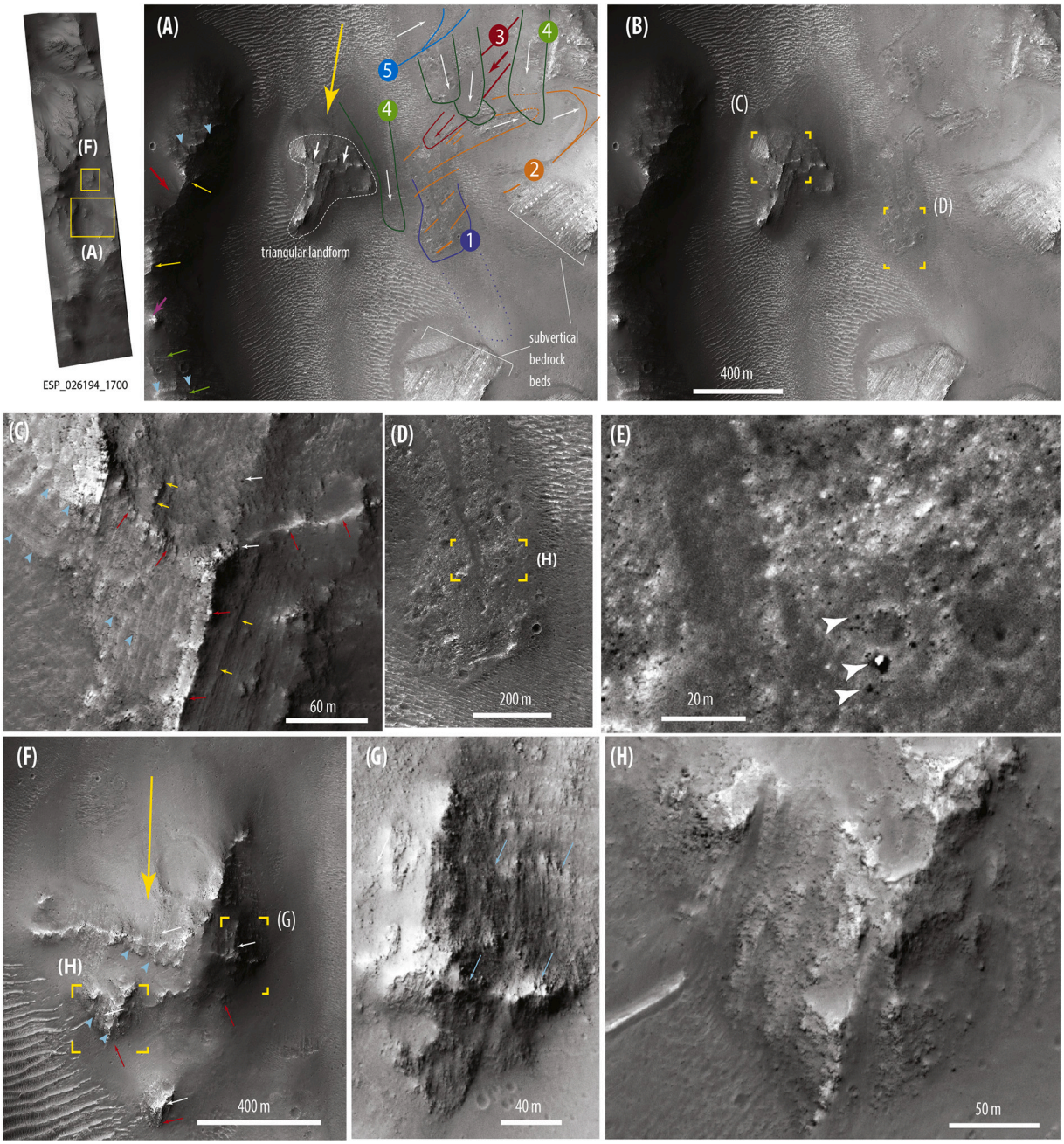

Fig. 7. HiRISE image ESP_026194_1700 showing landforms exposed on a trough floor in the central uplift. The upper-right index map shows the locations of images (A) and (F) that exhibit south-pointing triangular landforms. (A) An interpreted HiRISE image of a sharp-crested ridge (yellow arrows) transitioning southward into a round-topped ridge (green arrows). The change corresponds to a change from dark-toned thick-bedded coarse-grained-like beds to lighter-toned thinner-bedded and finer-grained-like beds (see text for detail). The sharp-crested ridge hosts a hanging valley (red arrow) and a horn-like peak (purple arrow), and exposes sub-vertical bedding (white dashed lines). Both the round-topped and sharp-crested ridges display steeply dipping beds (blue arrows). Lobate ridges are numbered from 1 to 5 (1 = dark blue, 2 = orange, 3 = red, 4 = dark green and 5 = light blue) in an older-to-younger sequence. White arrows indicate the interpreted emplacement directions of lobate ridges. Lobate ridge 1 is superposed by northeast-trending striations (solid orange lines). The eastern trough margin exposes smooth-surfaced bedrock outcrops displaying dipping bedding (white dashed lines). A hanging valley indicating a southeast-flow direction in the ridged terrain is shown in the image. The triangular mound complex on the valley floor has a streamlined and drumlin-like morphology. (B) Uninterpreted HiRISE image based on which (A) was interpreted. (C) A map-view triangular landform exposes bedding (blue arrows) similar to those exposed on the east side of the trough. The surface of the triangular landform displays north-trending striations (yellow arrows), dark-toned boulders (white arrows), and linear crests (red arrows). (D) A flat-topped lobate ridge composed of unconsolidated boulder deposits is shown in (E). (F) A triangular landform located north of the triangular landform and shown in (C) consists of smaller triangular ridges with striated surfaces (white arrows), south-pointing tips (red arrows), and dipping bedding (blues arrows). (G) A closer view of (F) that shows crudely layered boulder materials. (H) A smaller triangular ridge at the southern tip of a larger triangular landform shown in (F). (For interpretation of the references to color in this figure legend, the reader is referred to the web version of this article.)

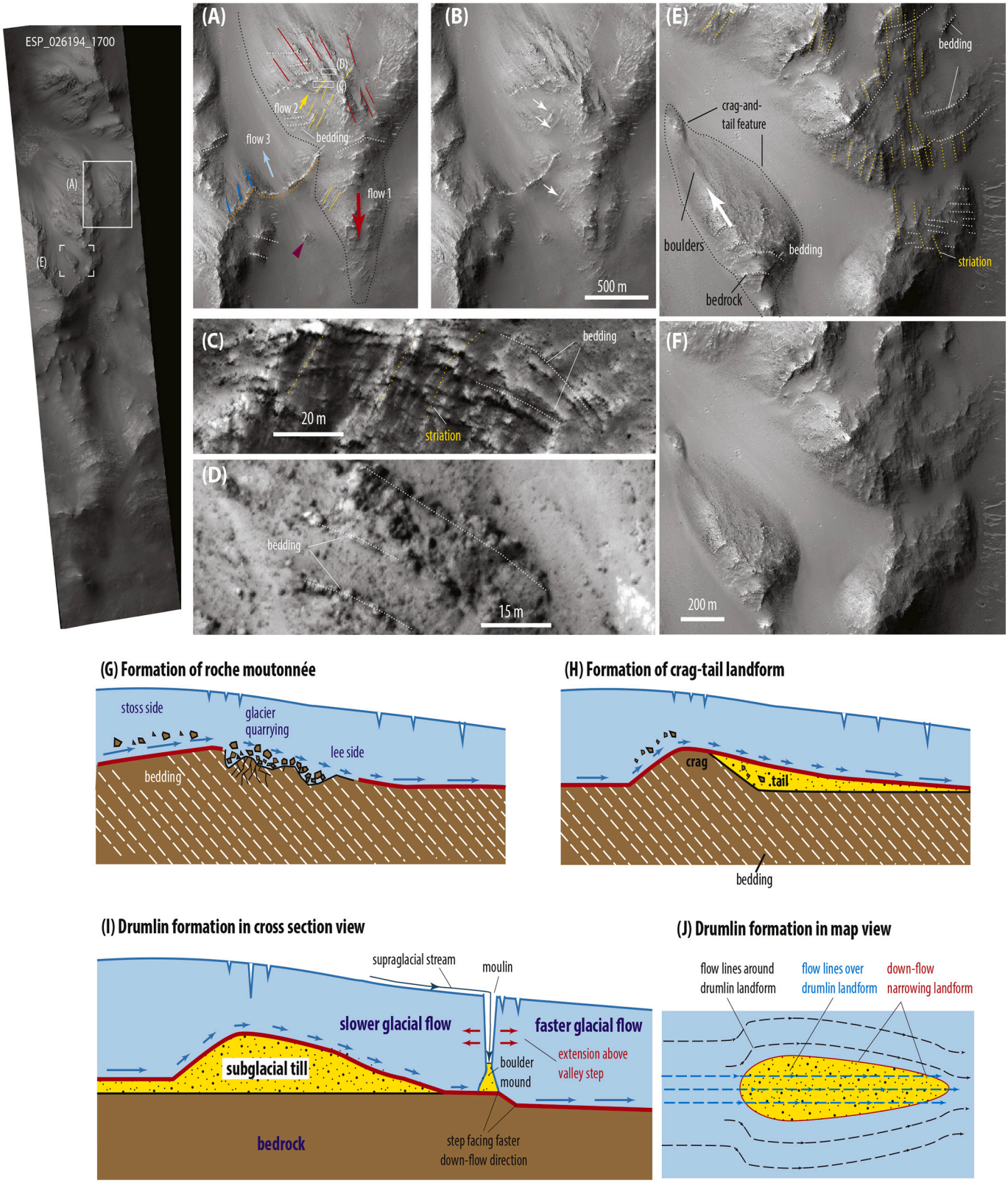

Fig. 8. (A) Interpreted morphologic features from HiRISE image ESP_026194_1700 shown in (B) along a trough in the central uplift. The trough floor displays a north-facing valley step (orange dashed line) where several north-plunging ridges emanate (blue lines), and an isolated boulder mound (purple arrow). Also shown in a south-pointing triangular ridge (large red arrow) exposing alternating dark-light albedo bands (white dashed lines) interpreted as bedding and exhibiting northwest-trending (red arrows) and northeast-trending (yellow arrows) ridges. (C) The northeast-trending linear ridges and grooves are constructed on bedrock and cut across the underlying beds. (D) The northeast-trending linear ridges terminate at a ridge crest across which the bedrock surface is dotted by boulders and angular broken beds. (E) Landform fabrics interpreted from a HiRISE image are shown in (F). (G) A schematic for the formation process of a roche moutonnée. (H) A schematic for the formation process of a crag-and-tail feature. (I) A schematic for the formation of a drumlin in cross section view. (J) A schematic for the formation of a drumlin in map view. (For interpretation of the references to color in this figure legend, the reader is referred to the web version of this article.)

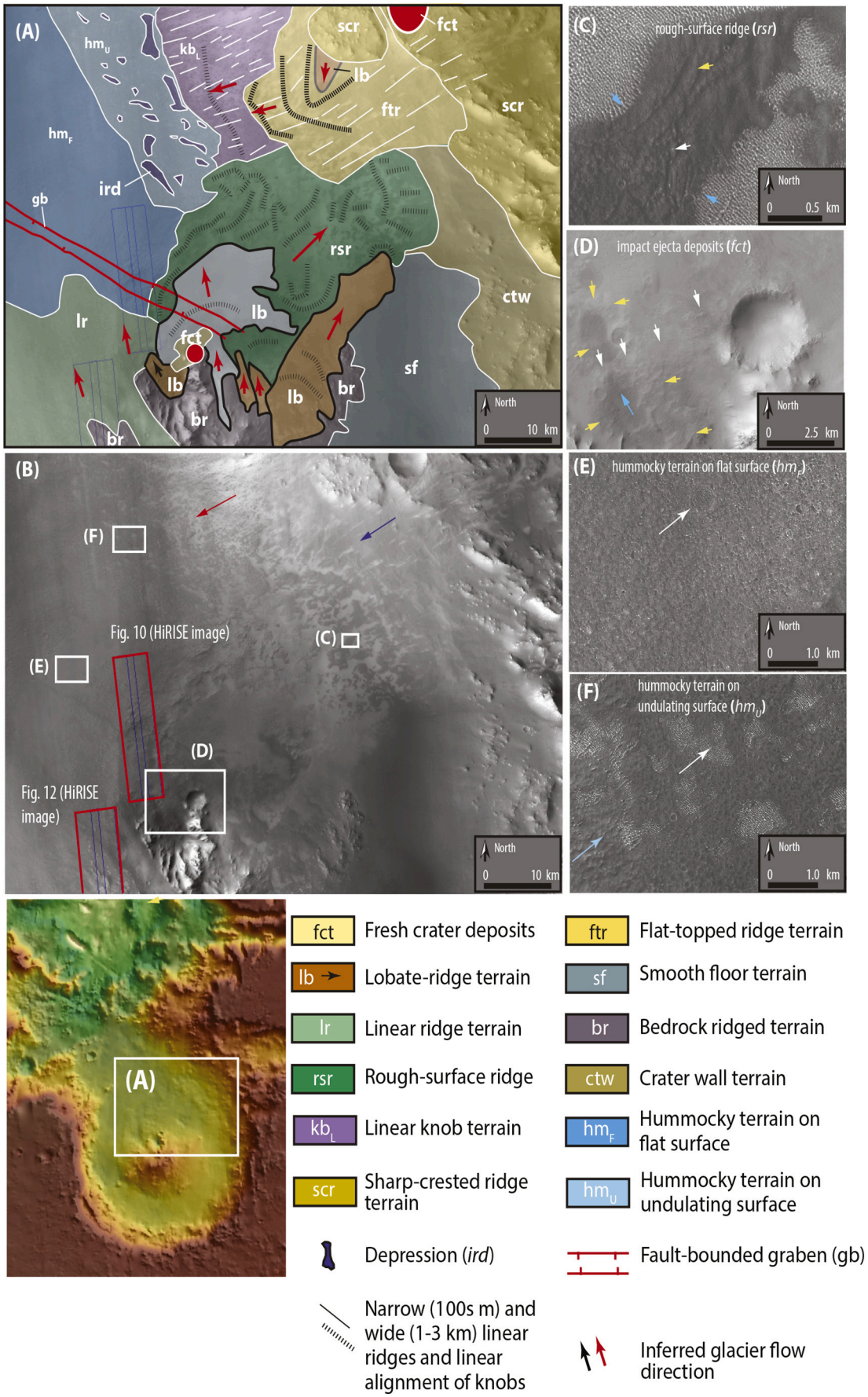

(caption on next page)

Fig. 9. (A) Geomorphologic map interpreted from a CTX image shown in (B). (C) Rough-surfaced ridge terrain (*rsr*) characterized by decameter- to meter-scale knob-like hummocks (white arrow) and minor curvilinear ridges (yellow arrow) parallel to the hosting ridges (blue arrows). (D) An impact crater and its related deposits (unit *fct*) (white arrows) are superposed on top of an elongated lobate ridge (*lb*) (yellow arrows) that bounds an interior depression (blue arrow). (E) Hummocky terrain on a flat surface (hm_F) where crater morphology is muted. (F) Hummocky terrain on an undulating surface (hm_U) dotted by irregularly shaped depressions (white arrows) and linear ridges (blue arrow). (For interpretation of the references to color in this figure legend, the reader is referred to the web version of this article.)

dotted by irregularly shaped depressions (white arrows in Fig. 9F) and linear ridges (blue arrow in Fig. 9F).

We mapped finer-scale geomorphological features in the northern crater-floor area (Fig. 10A; cf. Fig. 10B) and their cross-cutting relationship indicates two phases of landform development. The first phase is expressed by the formation of an undulating surface that hosts a landform assemblage consisting of the following features (Fig. 10B): (1) a smooth-surfaced northwest-sloping northwest-trending round-topped ridged terrain (*sm*) (*feature 1*) that has a sharp south-facing step (*feature 2*), (2) hummocky terrains characterized by northeast-trending fold-like hummocks (hm_f) (*feature 3*), northeast-trending chains of domes (hm_d) (*feature 4*), or mesa-like hummocks (hm_m) (*feature 5*), (3) boulder-bearing hills (unit *bh*) (*feature 6*), (4) irregularly shaped depressions (*ird*) (*feature 7*), and (5) a mound-moat terrain (unit *mm*) (*feature 8*). The area also exposes (Fig. 10B) longer northwest-trending (white dotted lines and *feature 9*) and shorter northeast-trending (blue dotted lines and *feature 10*) round-topped ridges with a hummocky-surface texture. Craters with their diameters greater than 500 m are muted (*feature 11* in Fig 10B), whereas craters with their diameters less than 100s m mostly display fresh-crater morphology with well-defined raised rims and locally related impact deposits (long blue arrow and *feature 12* in Fig 10B).

The second phase of landform development in the northern crater-floor is expressed by the largest-scale undulating surface extending across the entire mapped area and hosting the aforementioned landforms to have been cut by a northwest-trending trough (*feature A* in Fig. 10B). The trough-bounding escarpments consist of continuous and discontinuous segments that truncate and offset northwest-trending ridges (short white arrows and *feature B* in Fig. 10B). These observations suggest that the trough is a fault-bounded graben.

The south-facing step of the smooth-surfaced ridge terrain (unit *sm*) exposes subhorizontal strata with thinner-bedded finer-grained textures in the upper section (yellow arrows) and thicker-bedded coarser-grained textures in the lower section (white arrows) (Figs. 11A and 11B). The lower section displays hollows (blue arrows) and extruding knobs (red arrows) on a cliff face (Fig. 11B), which we interpret to represent boulder-sized clasts in a horizontally stratified sequence. This unit also hosts circular and elliptical pits (blue arrows) that enclose light-toned central mounds (green arrows) (Fig. 11A). Fig. 11C shows that the mounds consist of radial ridges (white arrows) and exhibit a rampart morphology next to the quasi-circular moats (yellow arrows). Fig. 11C also shows two phases of mound-moat construction: (1) an initial phase is expressed by a darker-toned landform associated with the central mound (green arrows) and a moat (blue arrows), and (2) a later-stage landform with a light-toned mound-moat association lies on top of the older construct.

Fig. 11D shows a field of circular, half-circular, and irregularly shaped low-relief hills (white arrows) next to mound-moat features (yellow arrows). The circular hills have locally raised rims and are composed of unconsolidated diamicton-like deposits expressed by light-toned finer-grained-like matrix and dark-toned boulder-sized clasts (Fig. 11E).

An exhumed fold complex exhibits a disharmonic bed geometry (Figs. 11F and 11G). The fold shape is defined by alternating curvilinear ridges (white arrows) and grooves (red arrows) (Fig. 11G). Also exposed in the area are three types of hummocky terrain. Fig. 11H (cf. Fig. 11I) shows a hummocky terrain associated with fold-like hummocks (hm_f) (yellow arrows) and folded beds (white arrows), Fig. 11J shows a hummocky terrain associated with elongated dome-like hummocks (hm_d), and Fig. 11K shows a hummocky terrain associated with internally layered mesa-like hummocks (hm_m).

Interpretation. Below, we discuss possible formation mechanisms of the pre-graben-formation landform assemblage in the mapped area described above. The fold-like northeast-trending hummocks (Figs. 11H and 11I) and the disharmonic fold complex may both have formed by tectonic deformation. However, this interpretation is problematic. First, the above interpretation does not explain why folds are local features. Second, the geometry of the disharmonic fold requires intra-bedding ductile flow (e.g., Ramsay and Huber, 1987), which can occur only as a result of crystal-plastic deformation under high temperatures (i.e., >350° C for felsic rocks and higher temperatures for mafic rocks) (Kohlstedt et al., 1995), or during soft-sediment deformation under high pore-fluid pressures during fluvial (Mills et al., 1983; Waldron and Gagnon, 2011; Shanmugam, 2017) or glacial processes (Rijsdijk et al., 1999; Boulton et al., 2001; Evans et al., 2006; Phillips et al., 2018). A high-temperature folding process would require regional ductile deformation, not consistent with the isolated occurrence of the disharmonic fold and fold-like hummocks. The lack of channels in the mapped area makes the fluvial origin of the folds unlikely.

Although aeolian processes may not explain the formation of folds, they could explain the formation of round-topped and flat-topped ridges (*features 6 and 7* in Fig. 10B) as yardangs, such as those observed on Earth (e.g., Kapp et al., 2011; Dong et al., 2012). This scenario is supported by the abundant aeolian bedforms in the mapped area (e.g., inside irregularly shaped depressions and muted crater basins; short red arrows and *feature 11* in Fig. 10B). However, an aeolian origin does not explain the hummocky-surface textures of the ridges, their close association with minor transverse ridges, and the occurrence of the mound-moat landforms on or next to the ridges.

Because the landform assemblage predating the graben formation is hosted by a single undulating surface (Figs. 10A and 10B), we hypothesize that its hosted assemblage was created by a single geologic process. As noted earlier, hummocky terrains are common features of glaciated landforms on Earth. Based on this inference, we construct a subglacial landsystem model shown in Fig. 11M, which is capable of explaining all the landform elements in the landform assemblage hosted by the regional hummocky surface in the mapped area described above. The model is largely inspired by a case study of subglacial structures below the Ordovician western Gondwana ice sheet in northern Africa that was carefully documented by Le Heron et al. (2005). It also borrowed concepts and interpretations from several classic studies on the role of subglacial-till deformation in creating glaciated landforms (Rijsdijk et al., 1999; Boulton et al., 2001; Evans et al., 2006; Phillips et al., 2018).

In our model (Fig. 11M), subglacial tills (*feature 1*) consist of megabreccia and boulder aggregates (*feature 2*) that are embedded in a finer-grained matrix (*feature 3*). The till layer lies above bedrock (*feature 4*) but below a moving ice sheet (Fig. 11M). Mud volcano chambers (*feature 5*) formed in high pore-fluid-pressure regions of the subglacial tills, and the emplacement of the mud-volcanic lava into the overlying ice sheet created mound-moat landforms (*feature 6A*) with a rampart

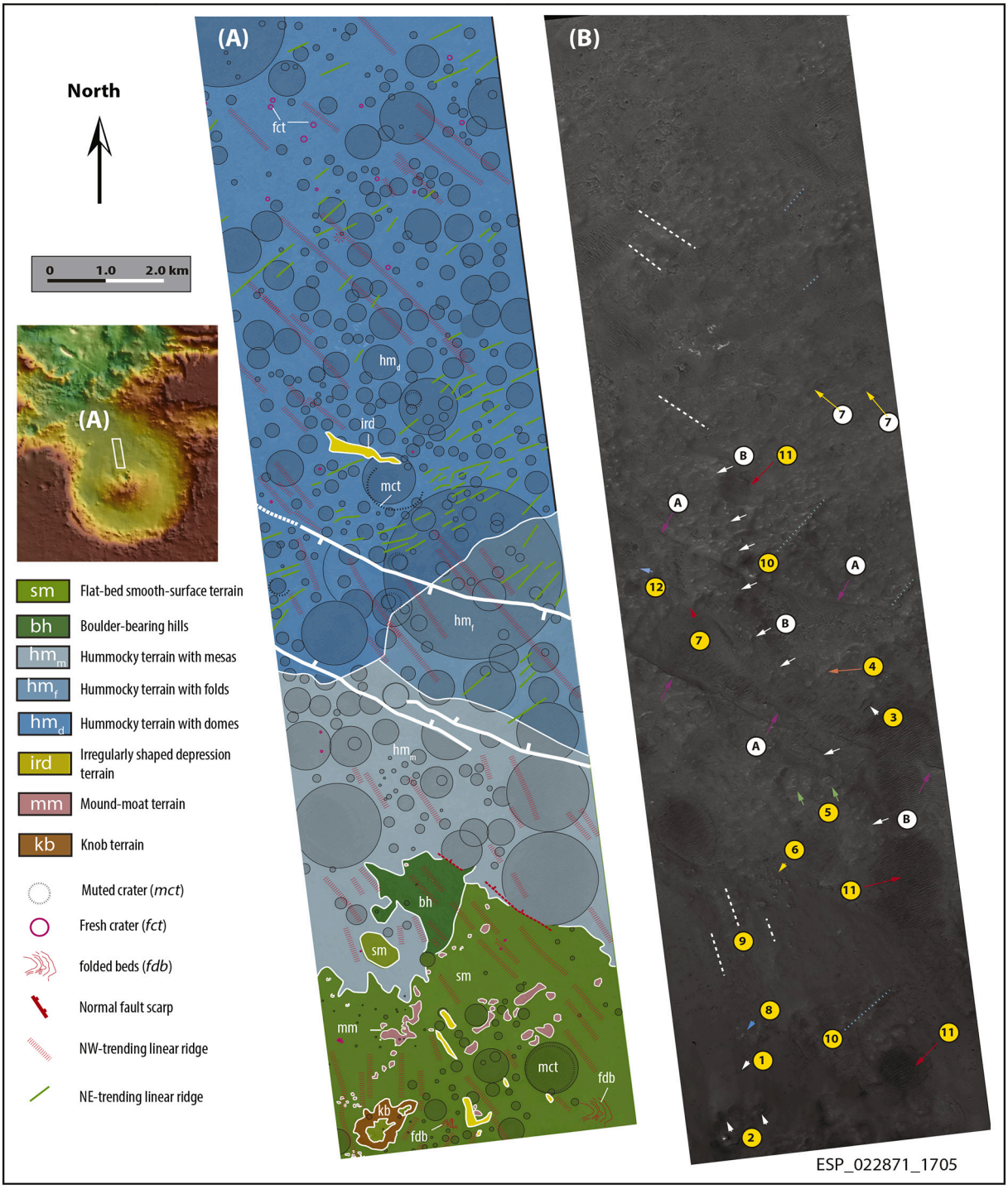

Fig. 10. (A) Geomorphologic map interpreted from a HiRISE image shown in (B). In B: a smooth-surfaced northwest-sloping northwest-trending round-topped ridge terrain (*sm*) (*feature 1*) displays a sharp south-facing step (*feature 2*); hummocky terrains have fold-like hummocks (hm_f) (*feature 3*), dome-chain-like hummocks (hm_d) (*feature 4*), and mesa-like hummocks (hm_m) (*feature 5*). The mapped area also hosts boulder-bearing hills (unit *bh*) (*feature 6*), irregularly shaped depressions (*ird*) (*feature 7*), and a mound-moat terrain (unit *mm*) (*feature 8*). Longer northwest-trending ridges (white dotted lines and *feature 9*) are superposed by shorter northeast-trending ridges (blue dotted lines and *feature 10*). Larger craters (D>500 m) are muted (*feature 11*), whereas smaller craters (D<100 m) mostly display fresh-crater morphology (long blue arrow and *feature 12*). A graben cuts across the area, which is bounded by linear escarpments (*feature A*) that offset a northwest-trending ridge (*feature B*). (For interpretation of the references to color in this figure legend, the reader is referred to the web version of this article.)

shape for the central mounds (*feature 6B*) (Fig. 11M). Emplacement of mud-volcano lava into the overlying ice sheet also generated flow lobes (*feature 7*) (Fig. 11M). Shear deformation of subglacial tills induced by overlying glacial flow created the observed disharmonic fold; meanwhile, basal ice sliding cut across and exhumed the fold complex on top of the subglacial shear zone (*feature 8*) (Fig. 11M). Glacial flow streamlined subglacial tills, which are expressed by the round-topped ridges (*feature 9*) (Fig. 11M; cf. northwest-trending ridges in Fig. 10B). Melting of the stagnant ice blocks in subglacial tills created the irregularly shaped depressions on a hummocky surface (*feature 10*) (Fig. 11M). Supraglacial debris transported through moulins (*feature 11A*) formed the mesa-like hummocky terrain in ice-wall glacial lakes (*feature 11B*)

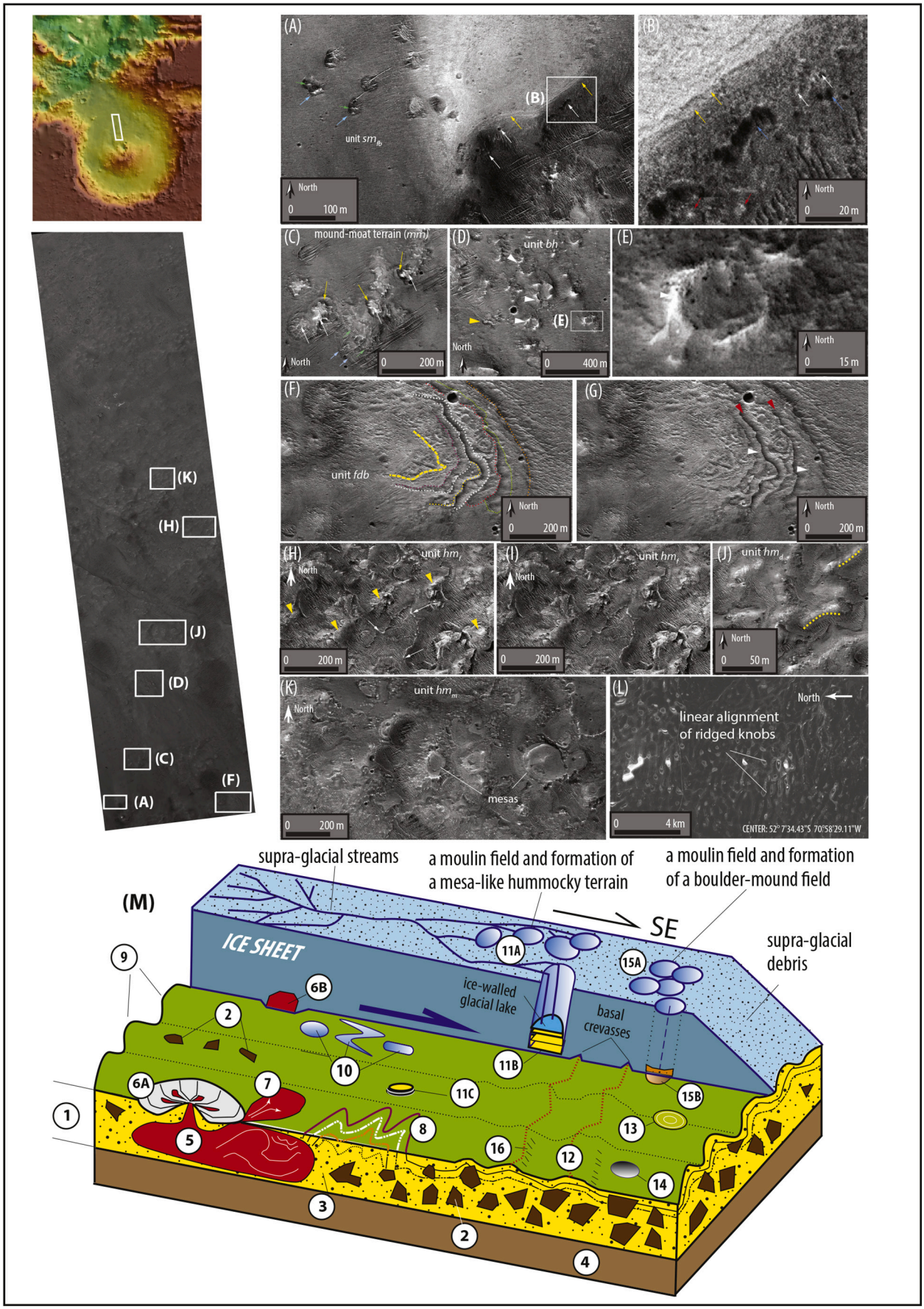

(caption on next page)

Fig. 11. HiRISE image (ESP_022871_1705) displaying landforms mentioned in the text. (A) Smooth-surfaced terrain (*sm*) hosts circular and elliptical pits (blue arrows) that enclose light-toned central mounds (green arrows). Smooth-surfaced terrain is composed of subhorizontal strata below the surface with thinner-bedded finer-grained-like materials in the upper section (yellow arrows) and thicker-bedded coarser-grained-like materials in the lower section (white arrows). (B) The lower section displays hollows (blue arrows) and extruding knobs (red arrows) interpreted to represent boulders. The upper section (yellow arrows) displays a finer surface texture interpreted to indicate a finer-grain size than that in the lower section. (C) Mound-moat terrain with the mounds consisting of radial ridges (white arrows) and displaying a rampart morphology next to quasi-circular moats (yellow arrows). Also shown are two phases of mound-moat construction: the older phase is expressed by a darker-toned landform associated with a central mound (green arrows) and a moat (blue arrows), whereas the younger phase is expressed by the formation of a light-toned mound-moat association constructed on top of the older mound-moat association. (D) Circular, half-circular, and irregularly shaped hills (white arrows) next to mound-moat features (yellow arrows). (E) A view of a circular hill exposing unconsolidated diamicton-like deposits. (F) A disharmonic fold with interpreted bedding traces, cf. (G). (G) The fold shape is defined by alternating curvilinear ridges (white arrows) and grooves (red arrows). (H) Hummocky terrain with fold-like hummocks (hm_f) (yellow arrows) and folded beds (white arrows). Interpreted (I) and uninterpreted (H) HiRISE image of a hummocky terrain associated with fold-like hummocks. (J) Hummocky terrain with slightly elongated dome-like hummocks (hm_d). (K) Hummocky terrain with mesa-like hummocks (hm_m). (L) A Google Earth image of a hummocky terrain defined by elongated dome-like hummocks from the Patagonia ice field. See text for details. (M) A glacial landsystem model that explains the observed landform features from the northern crater floor: 1 = subglacial tills; 2 = mega-breccia and boulder aggregates; 3 = matrix material in subglacial tills; 4 = bedrock; 5 = mud-volcano chamber; 6 = mound-moat landform generated by mud volcanism; 7 = lobes emanating from a mound-moat structure; 8 = exhumed fold complex in deformed subglacial tills; 9 = round-topped ridges; 10 = stagnant ice blocks in subglacial tills; 11 = circular mesas exposing layered materials as ice-walled glacial-lake deposits; 12 = transverse ridges as ribbed moraines; 13 = subglacial-till-filled crater; 14 = glacially eroded crater without raised rim; 15 = semi-circular mounds with raised rims interpreted as kames; 16 = SE-facing steps resulting from southeastward glacial flow. (For interpretation of the references to color in this figure legend, the reader is referred to the web version of this article.)

(Fig. 11M), which explains the interior layering of the mesas (*feature 11C*) (Fig. 11M). Minor transverse ridges (i.e. northeast-trending ridges in Fig. 10B) superposed on top of the wider and longer ridges (i.e., northwest-trending ridges in Fig. 10B) were produced by basal crevasse squeezing (*feature 12*) (Fig. 11M) while the moving glacier caused streamlining of the northeast-trending ridges in the subglacial tills.

Craters were filled by glacial tills (*feature 13*) and their rims were worn out by glacier abrasion (*feature 14*) (Fig. 11M), which explains the widely occurring muted crater basins without raised rims in Fig. 10B. Although mantling materials may obscure the original crater morphology, their deposition should not have caused the removal of the raised crater rims commonly associated with the muted crater basins in the study area. We also note that our study area located at the latitude of ~10 °S is outside the latitude-dependent mantling terrain that is best developed at latitudes of >30° (Dickson et al., 2015). A moulin field connecting the interpreted ice-sheet surface to the ice-sheet base may have transported coarser-grained supraglacial debris to the base of the ice; this process created low-relief boulder-bearing hills; the locally raised rims of these hills may have been caused by the ice-wall effect during glacial-lake deposition (*feature 15*) (Fig. 11M). We suggest that the step-like northeast-trending features in Fig. 10B to have been produced by differential basal sliding velocity (see Fig. 8I) that was later explored by glacier quarrying processes (see Iverson, 2012 for the related mechanics and physics). The step-facing direction indicates a southeastward glacial flow (*feature 16*) (Fig. 11M), which is generally parallel to the inferred southward-flowing glaciation across the central uplift as discussed earlier.

Our proposed interpretation of the central-mound rampart morphology as a result of mud-lava intrusion beneath an overlying ice sheet is similar to the process proposed for the formation of a tuya-like volcano construct below an ice sheet or a glacier (cf., tuyas in Antarctica, Alaska, and Iceland as described in Smellie, 2006). A key difference between the igneous-lava vs. mud-lava emplacement into an overlying ice is as follows. The igneous lava has a deep crustal source and its emplacement does not produce a moat around the volcanic cone. In contrast, mud withdraw from a near-surface source would have created a moat bounding the central erupting mound as shown in Fig. 11M.

We note that the linearly aligned dome-like hummocks (yellow arrows in Fig. 10B) are similar to those exposed in a Quaternary glaciated piedmont of the southern Patagonia ice field (Fig. 11L) (Bendle et al., 2017). This piedmont setting on Earth is similar to the northern crater-floor area located in the piedmont plain of the central uplift of Oudemans crater. The above similarity further strengthens our glacier-origin interpretation for the hummocky terrain, which in turn supports our overall subglacial landsystem model shown in Fig. 11M.

Although the viscous-flow material associated with the interpreted mud volcanism could have been alternatively interpreted by igneous volcanism, the size of the erupting systems, only 10s of m across (Fig. 11C), appears to be too small to serve as volcanic eruption centers. Additionally, the light-toned flow material is not consistent with a basaltic material, generally inferred as the dominant volcanic type in the study area (e.g., Witbeck et al., 1991; McEwen et al., 1999).

(2) Western Crater-Floor Area. The dominant northwest-trending linear ridges (Figs. 12A and 12B) expose mega-breccias (10s of m across) and boulder (a few meters in size) aggregates that are 10s of m to >100 m across. The breccias and boulder aggregates are embedded in a darker-toned finer-grained-like matrix (Fig. 12C; cf. Fig. 12D). The larger northwest-trending ridges, labelled as major linear ridges in Fig. 12A, are superposed by smaller northeast-trending ridges, marked as linear ridges in the lower-left corner of Fig. 12C (solid yellow lines). This relationship is similar to that in the northern crater-floor area as shown in Fig. 10A. The major ridges also expose mound-moat landforms (Fig. 12C) that, again, are similar in form to those exposed in the northern crater-floor area as described earlier. The mound-moat landforms in the western crater-floor area (Fig. 12C) are characterized by (1) marginal lobate ridges (green dashed lines) on the bounding plateau, (2) ring-shaped moats, (3) central mounds (red triangles) with a rampart morphology (white arrows in Fig. 12D; cf. Fig. 11C), and (4) ring-like inward-facing scarps (red lines with tick marks).

Major ridges (unit hm_r in Fig. 12B) display hummocky surface textures and are bounded by irregularly shaped depressions (unit hm_p in Fig. 12B). Some hummocks on ridge tops and in depressions are dome-like (unit hm_d in Fig. 12B), occur in groups, and transition to the neighboring "block-in-a-viscous-flow-material" unit (unit *bv* in Fig. 12B). The latter consists of light-toned "rigid blocks" surrounded by a darker-toned matrix characterized by curvilinear grooves and ridges (Figs. 12E and 12F).

Interpretation. The landform assemblage in this area is similar to that exposed in the northern crater-floor area, but with the exposure of two additional units: (1) a ductile-flow-like matrix that surrounds rigid blocks (Figs. 12E and 12F), and (2) deposits composed of mega-breccias and boulder-bearing aggregates in a darker-toned finer-grained-like matrix (Figs. 12B and 12D). Although the mega-breccias alone may be interpreted as products of an impact (McEwen et al., 2010) during the formation of the Oudemans crater basin, their close association with matrix-supported boulder aggregates (Figs. 12C and 12D) requires a geologic process that was capable of mixing of breccias, boulder aggregates, and dark-toned matrix materials. The size (10s of m to >100 m) of breccias and boulder aggregates requires a high-energy transport process such as debris-flow deposition, alluvial-fan deposition, or glacial

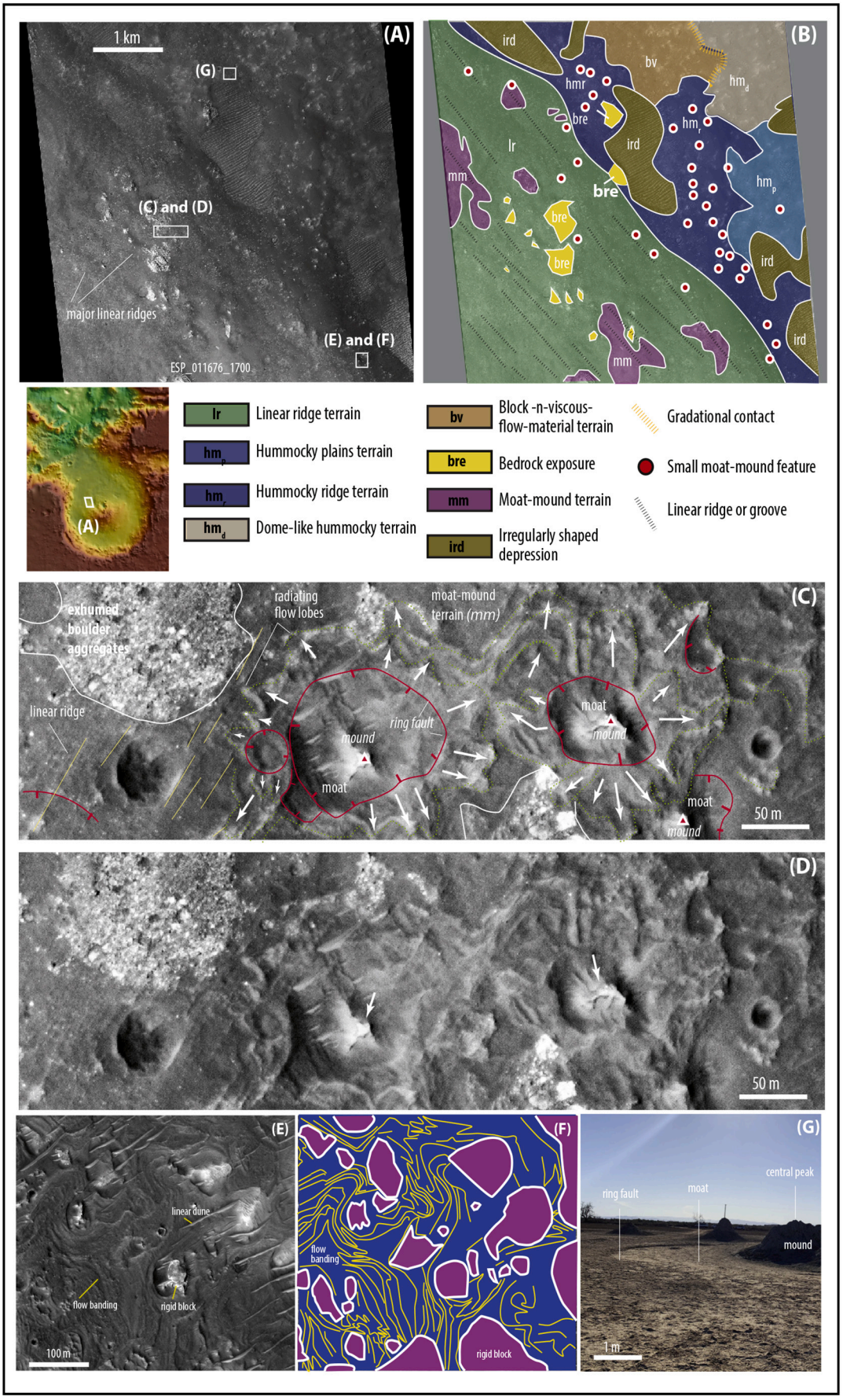

(caption on next page)

Fig. 12. An uninterpreted (A) and interpreted (B) HiRISE image ESP_026194_1700. (C) Interpreted geomorphic features on a northwest-trending ridge from HiRISE image ESP_026194_1700, which exposes mega-breccias (10s of m across) and boulder-bearing (a few meters in size) aggregates (10s of m to >100 m) in a darker-toned finer-grained-like matrix. Mound-moat landforms are characterized by (1) marginal lobate ridges (green dashed lines) on the bounding plateau surface, (2) ring-shaped moats, (3) central mounds (red triangles) with a rampart morphology, and (4) ring-like inward-facing scarps (red lines with tick marks). (D) Uninterpreted HiRISE image ESP_026194_1700 corresponding to the map shown in (C). White arrows show the rampart morphology of central mounds. (E) "Rigid-block-in-a-viscous-flow material" terrain (unit *bv*) displays many similarities to the mound-moat landforms. See text for details. (F) Interpreted viscous-flow-like matrix that bounds mound-moat landforms. (G) A mud-volcano field from Salton Sea of southern California for comparison against the mound-moat landforms on the western floor of Oudemans crater. See text for details. (For interpretation of the references to color in this figure legend, the reader is referred to the web version of this article.)

transport. Debris flow- and alluvial-fan construction should have produced internal layering, channel bodies, clast imbrications, and clast grading in the sedimentary sequence (e.g., Blair, 1999). None of these features are observed in this unit (Fig. 12D). This led us to propose that the matrix-supported breccias and boulder aggregates are clasts in subglacial tills.

Similar to our interpretations for the northern crater-floor area, we suggest that the mound-moat features may resemble mud volcanos intruded into an overlying ice sheet (Fig. 11M). Mud volcanoes have been reported in the northern lowlands (Oehler and Allen, 2010) and Valles Marineris in the Tharsis region (Okubo, 2016). The mechanical plausibility of mud-volcano formation on Mars was also demonstrated by Brož et al. (2020). Although mud volcanoes on Earth occur in a wide range of geologic settings (Mazzini et al., 2011), they all share the same formation mechanism involving high-fluid pressures in unconsolidated materials (Skinner Jr and Mazzini, 2009; Loher et al., 2018). An example on Earth is from the Salton Sea area of California (Fig. 12G), where geothermal heating from below induces high-pore-fluid pressures in unconsolidated lake deposits that in turn created mud volcanoes (e.g., Mazzini et al., 2011; Onderdonk et al., 2011). In our case, we infer the high-pore-fluid pressure to have been generated by deformation-induced compaction of subglacial tills, following the interpretation of similar features exposed on Earth (e.g., Rijsdijk et al., 1999; Boulton et al., 2001). A key difference between our interpreted mud-lava intrusion into an overlying ice sheet (Fig. 12C) versus the mud lava emplaced onto Earth's surface (e.g., Salton Sea mud volcanoes in Fig. 12G) is that the shape of the subglacial mud-lava flows are constricted by an overlying ice sheet interpreted to have existed in our study area.

The "rigid-block-in-a-viscous-flow" features (Figs. 12E and 12F) (unit *bv* in Fig. 12A) have many similarities to the mound-moat landforms: both consist of light-toned central mounds with a rampart morphology, bounding moats, and surrounding darker-toned plateau plains. Here, we suggest that unit *bv* is a modified form of the mound-moat unit; its radiating flow lobes as shown in green dashed lines in Fig. 12C were modified by younger ductile flow of water-saturated subglacial tills during ice-sheet flow.

(3) Eastern Crater-Floor Area. This area exposes lobate round-topped ridges and southward-pointing triangular landforms (Fig. 13A; cf. Fig. 13B). The ridges (white arrows) are superposed on top of quasi-circular depressions interpreted as denudated impact craters (blue arrows) (Fig. 13C). The ridges bound interior depressions (yellow arrows), and their surfaces are marked by muted craters with irregular rims (red arrows) (Fig. 13C). Lighter-toned sharp-crested linear ridges (Fig. 13D) on top of the triangular landforms display striated surfaces (yellow arrows in Fig. 13E).

The eastern crater-floor area also exposes a circular depression that is rimmed by a ridge (Fig. 13F; cf. Fig. 13G) with a northern lighter-toned segment (*feature 1* in Fig. 13F) and a southern darker-toned segment (*feature 2* in Fig. 13F). The northern segment displays a sharp-crested morphology and is linked with a wider northeast-trending curvilinear sharp-crested ridge to the north. The southern segment exhibits a round-topped ridge morphology and is locally connected with apron-like deposits defined by a convex-southward rim across the southern flank of the circular depression (*feature 3* in Fig. 13F). Inside the circular depression is a zone of convex-southward round-topped lobate ridges (*feature 4* in Fig. 13F). The northern edge of the depression has a northward-opening gap that links the basin floor with the outside plain (*feature 5* in Fig. 13F). Also present is a set of northeast-trending ridges (*feature 6* in Fig. 13F). We interpret this circular depression as an impact basin. Although it is much smaller, the shape of the basin with a missing northern wall and a zone of convex southward lobate ridges are remarkably similar to the much larger Oudemans crater basin that also has a missing northern wall and hosts a zone of convex southward lobate ridges (see Figs. 1B and 4B).

Interpretation. The presence of lobate ridges cannot be explained by impact, aeolian, fluvial, or tectonic processes. However, such features are reminiscent of recessional moraines on Earth (Lastras and Dowdeswell, 2016; Chandler et al., 2016). Interpreting the lobate ridges as recessional moraines implies (1) the ridges having a depositional origin and (2) the muted craters having their raised rims removed by glacial erosion. Interpreting the lobate ridges as recessional moraines requires a southwestward glacial-flow direction (white arrow in Fig. 13C).

The triangular landforms on the crater floor resemble drumlins on Earth (Trenhaile, 1975; Johnson et al., 2010; Clark et al., 2018). Their southward-tapering geometry indicates a southward-flowing glacier (green arrows in Fig. 13A), consistent with the flow direction indicated by the nearby lobate ridges (white arrow in Fig. 13A).

We interpret the circular depression to be an impact basin (*feature 4* in Fig. 13F), and the lobate ridges within the basin to represent recessional moraines (red arrow in Fig. 13F). The missing northern wall of the crater was a result of southward-flowing glacial erosion, and the southern apron with a southward convex rim represents spillover southward-flowing glacial deposits. The northeast-trending sharp-crested linear ridge emanated from the northeastern crater rim and trending parallel to sharp-crested ridges on the nearby crater floor may have resulted from subglacial streamlining processes.

(4) Southern and Southwestern Crater-Floor Areas. The southern crater-floor area is dominated by a hummocky surface that hosts lobate ridges (*feature 1*) and elongated depressions (*feature 2*) (Fig. 14A; cf. Figs. 14B, 14C, and 14D). The surface dotted by domes and round-topped ridges (Fig. 14E) terminates at a knobbed terrain against the southern crater-wall zone mapped in Fig. 2B. The knobbed terrain consists of round-topped ridges and mounds on top of a hummocky surface (*feature 3* in Fig. 14A). This terrain cuts across sharp-crested linear ridges (*feature 4* in Fig. 14A) that are part of the crater-wall unit shown in Fig. 2B. This relationship suggests the knob terrain to have formed after the Oudemans impact event.

Lobate ridges bounding interior depressions (green arrow) have their surfaces dotted by hummocks (white arrow), knobs (yellow arrow), and smooth-surfaced patches (red arrow) (Fig. 14C). The crater-floor plains that host the lobate ridges exhibit muted craters without raised rims (blue arrows in Fig. 14C). The lobate-ridge surfaces are also covered by irregularly shaped depressions (white arrows in Fig. 14D).

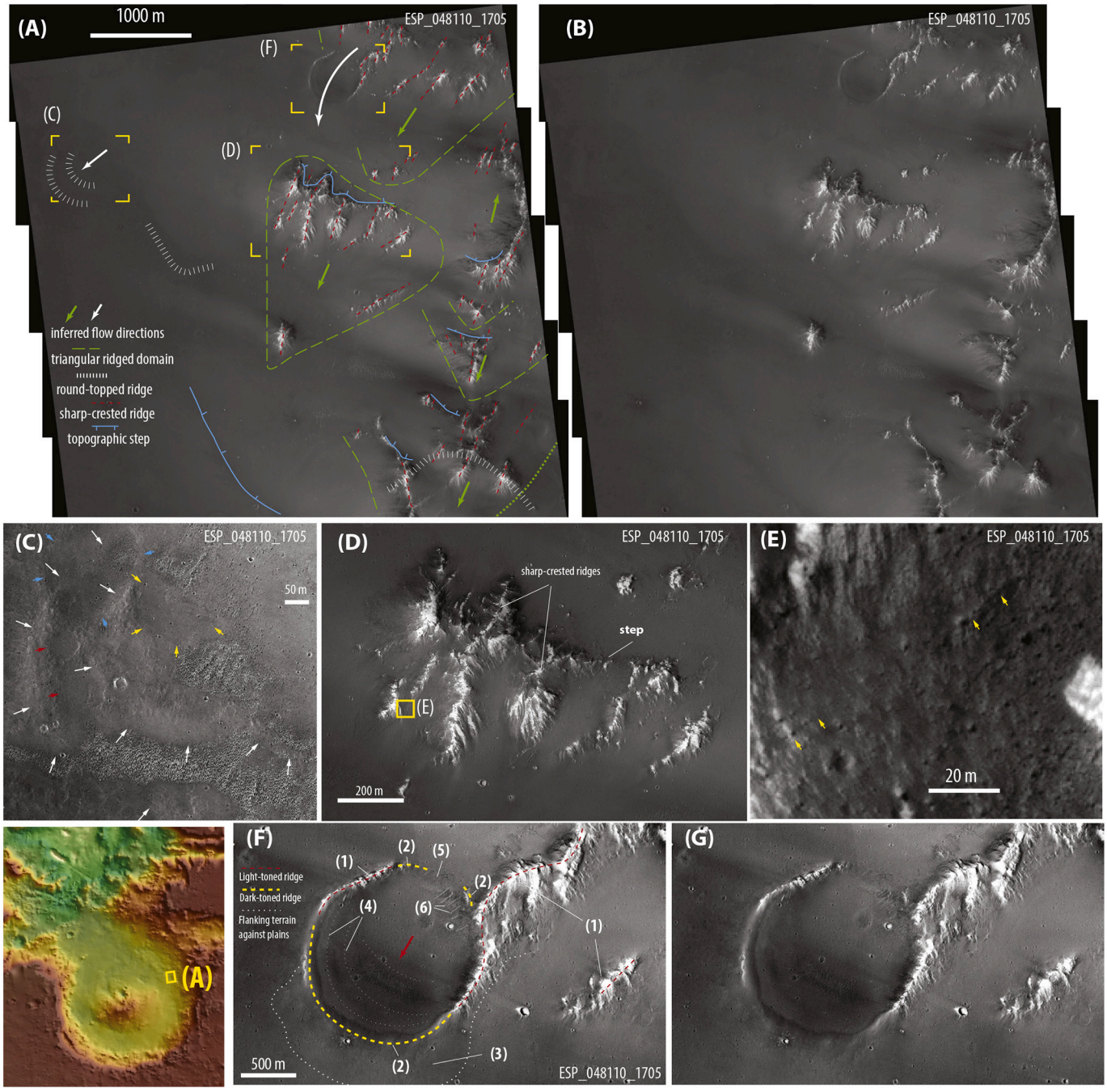

Fig. 13. (A) Interpreted HiRISE image (ESP_048110_1705) from an eastern crater-floor area that displays round-topped lobate ridges (white dashed lines) and sharp-crested ridges within southward-pointing triangular landforms (green dashed lines). The white and green arrows are inferred glacier-flow directions. (B) Uninterpreted HiRISE image (ESP_048110_1705) corresponding to (A). (C) Lobate ridges (white arrows) are superposed on top of quasi-circular depressions interpreted as denudated impact craters (blue arrows). The lobate ridges bound interior depressions (yellow arrows) dotted by muted crater basins with irregular crater rims (red arrows). (D) Lighter-toned sharp-crested linear ridges in triangular landforms display striated surfaces marked by yellow arrows in (E). (F) and (G) are interpreted and an uninterpreted HiRISE image. See (A) for location. The image shows a circular depression rimmed by a ridge consisting of a northern lighter-toned segment (*feature 1*) and a southern darker-toned segment (*feature 2*). The former displays a sharp-crested morphology and is linked with a wider northeast-trending curvilinear sharp-crested ridge to the north. The latter exhibits a round-topped morphology and is locally connected with apron-like deposits across the southern flank (*feature 3*) of the depression. Inside the circular depression is a zone of convex-southward round-topped lobate ridges (*feature 4*). The northern edge of the circular depression has a gap that allows the floor of the circular-depression to link with the outside plains (*feature 5*). Also present is a set of northeast-trending linear ridges in the northeastern corner of the depression (*feature 6*). The red arrow in (F) indicates the inferred ice-flow direction. (For interpretation of the references to color in this figure legend, the reader is referred to the web version of this article.)

The southwestern Oudemans crater-floor area exposes a curvilinear channel-like groove with a flat floor and steep walls (white arrows). This feature cuts into a hummocky surface and has abrupt terminations (Fig. 14F). The crater floor in this area also displays south-trending southward-tapering ridges (yellow arrows in Fig. 14F). Fig. 14G (cf. Fig. 14H) shows that these ridges occur immediately next to several convex-southward lobate ridges with a hummocky-surface texture.

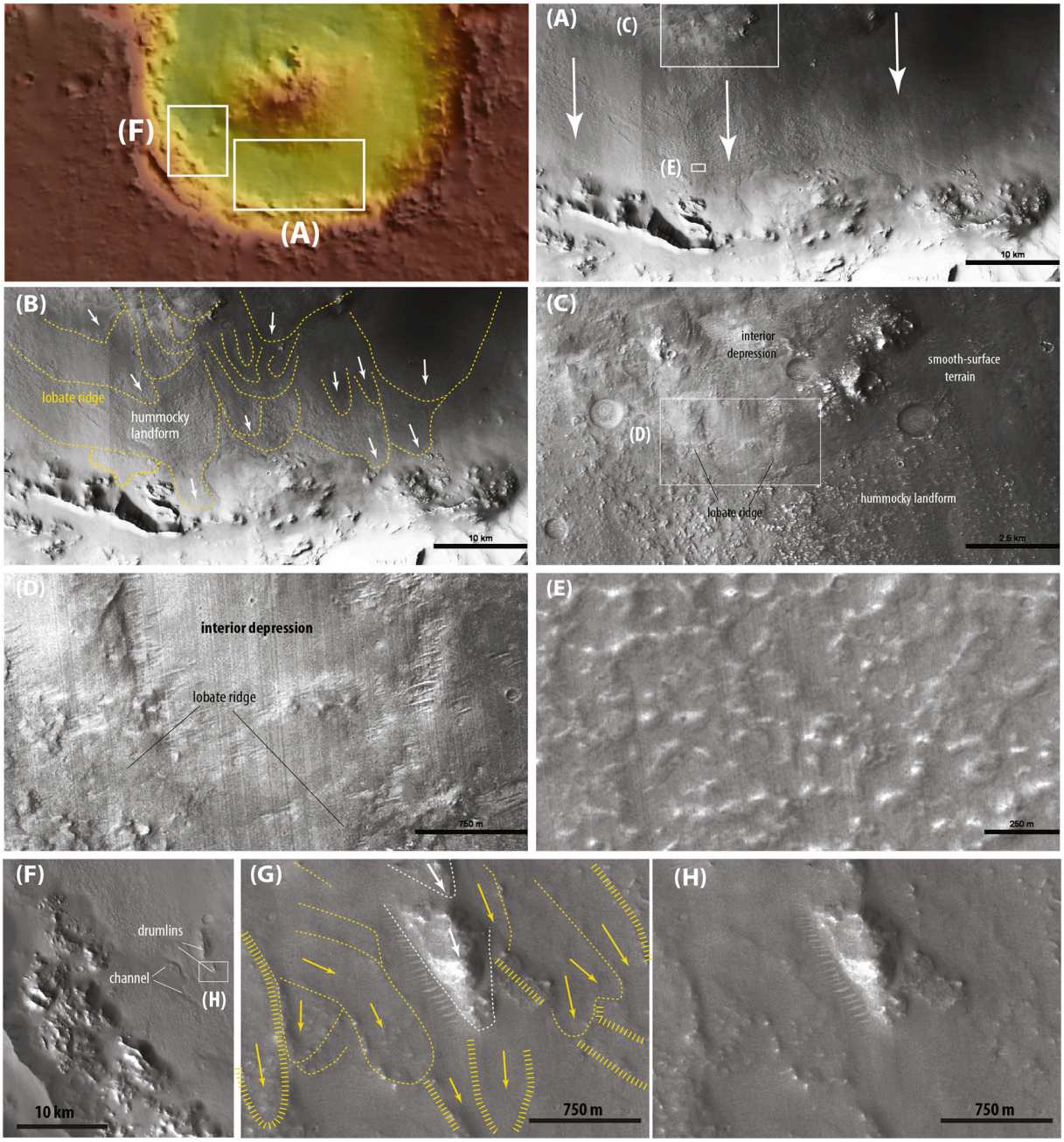

Fig. 14. (A) and (B) are interpreted and uninterpreted CTX image of the southern crater-floor area, which is dominated by a hummocky surface that hosts lobate ridges (*feature 1*) and elongated depressions (*feature 2*). The surface terminates at a knobbed terrain (*feature 3*) that cuts across sharp-crested linear ridges (*feature 4*) belonging to the crater-wall zone. (C) Lobate ridges bound interior depressions (green arrow) and are dotted by hummocks (white arrow), knobs (yellow arrow), and smooth-surfaced patches (red arrow). The plain region next to the lobate ridges exhibits muted craters (blue arrows). (D) Surface of the lobate ridges displays irregularly shaped depressions (white arrows). (F) The southwestern Oudemans crater-floor area exhibits a curvilinear channel-like groove with a flat floor and steep walls (white arrows). The channel-like groove cuts into a hummocky surface. The crater floor also displays south-trending southward-tapering ridges (yellow arrows). (G) and (H) Convex-southward lobate ridges with hummocky-surface textures. (For interpretation of the references to color in this figure legend, the reader is referred to the web version of this article.)

Interpretation. As discussed earlier, lobate ridges, hummocky terrains, and unidirectional tapering ridges could all have been generated by glaciation. Specifically, we suggest that the lobate ridges were created by recessional-moraine construction, hummocky terrains were created by dead-ice melting within subglacial tills, and tapering ridges were created by subglacial streamlining processes. The curvilinear groove with a flat floor, steep walls, and abrupt terminations may represent a subglacial meltwater channel, because its morphology is similar to those reported on Earth (i.e., tunnel valleys) (e.g., Livingstone and Clark, 2016). The shape of the lobate ridges and the morphology of the streamlined ridges consistently indicate a southward glacial flow in the southern (Fig. 14A) and southwestern (Fig. 14G) crater-floor areas. The knobbed terrain (*feature 3* in Fig. 14A) may represent terminal moraines or supraglacial tills.

5.3. *Crater-bounding plateau plains*

The plateau plains bounding the east side of Oudemans crater display

(1) pitted hummocky terrain (unit hm_P), (2) striated hummocky terrain (unit hm_S), (3) lobate-ridged hummocky terrain (unit hm_R), (4) a lineated smooth-surfaced terrain (unit *lsm*), (5) a muted lineated terrain (unit *mle*), and (6) a lineated terrain (unit *le*) (Fig. 15). A suite of northwest-trending steep-walled and flat-floored troughs are also present in the area (*swt-1* to *swt-4* in Fig. 15B). The troughs are not parallel and their trends change systematically from ~N35°W in the north for *swt-1* to ~N70°W in the south for *swt-4*. The steep-walled troughs are spatially associated with pit fields (blue arrows Fig. 15B). The latter are superposed on top of, and hence postdate, linear landforms that trend radially from Oudemans crater (red arrows in Fig. 15B). Linear, orthogonally terminating, and curvilinear channels (*ch1-ch3* shown by white arrows in Fig. 15B) cut across pit fields and/or steep-walled troughs (Fig. 15B).

Plateau-plain craters are characterized by: (1) rims superposed by pits (labelled as "*prec*" and an associated green arrow in Fig. 15B), (2) ejecta deposits overlying the pitted terrain (labelled as "*pstc*" and associated orange arrows in Fig. 15B), and (3) partially filled crater basins (labelled as "*fdc*" and associated black arrow in Fig. 15B). Also present are north-trending mound chains consisting of ridges or interconnected knobs (pink arrows in Fig. 15B).

Steep-walled flat-floored troughs could represent grabens (see Figs. 3O and 10B) or erosional channels. To differentiate the two possibilities, we examine two steep-walled troughs on the plateau plains in detail. For the first trough (unit *swt-1* in Fig. 15B), its northeastern margin defined by two round-topped ridges (yellow arrows in Fig. 16A) is cut across by an L-shaped gully (white arrows in Fig. 16A), which turns abruptly from an east trend to a north trend as it extends westward (red arrows in Fig. 16A). Its southwestern margin terminates at a cliff in the north. When projected linearly northward (dotted red line in Fig. 16B), the trace of the extended margin *does not offset beds* below the trough floor (white arrows in Fig. 16C). This observation indicates that unit *swt-1* in Fig. 15B is an erosional rather than tectonic feature.

Similar observations apply to the second trough (unit *swt-2* in Fig. 15) that has a Z-shaped northeastern margin (yellow arrows in Fig. 16D) and a linear southwestern margin (red arrows in Fig. 16D). The trough terminates at a northern cliff face (Figs. 16D and 16E) and a southern pit field (red arrows in Fig. 15F). When projected along its trend, the trace of the northeastern trough margin *does not offset beds* below (white arrows) (Fig. 16E), which rules out a graben origin.

The pitted hummocky terrain (unit hm_P) (blue arrows in Fig. 15B) displays groove-like northeast-trending linear depressions. This terrain also exposes circular- and oval-shaped depressions, and a washboard-like landform pattern. The latter is defined by orthogonal sets of ridges and grooves trending in the northeast and northwest directions, respectively (Figs. 16G and 16H).

The striated hummocky terrain (unit hm_S) is dominated by northeast-trending linear (red arrows in Fig. 16I) and curvilinear (red arrows in Fig. 16J) ridges. This terrain is locally dotted by irregularly shaped depressions (blue arrow in Fig. 16I) and displays washboard-like landforms defined by the longer northeast-trending ridges (red arrows) and shorter northwest-trending ridges (white arrows) (Fig. 16J).

The lobate-ridged hummocky terrain (unit hm_R) displays convex-southward round-topped lobate ridges (white dashed lines in Fig. 16L; cf. Fig. 16K). These ridges truncate and/or override the northwest-trending trough *swt-3* in Fig. 15B, which is bounded by steep walls (red dotted lines in Fig. 16N; cf. the uninterpreted image shown in Fig. 16M). The trough that is overridden by a lobate ridge itself truncates an older lobate ridge (yellow dotted line in Fig. 16L). Because no landforms are offset by the trough margins, we interpret the trough to be an erosional feature. The mutual cross-cutting relationship requires the steep-walled trough and southward-protruding lobate ridges to have formed coevally.

The lineated smooth-surfaced terrain (unit *lsm*) occurs as a north-trending strip between two muted linear ejecta terrains (unit *mle*) (Fig. 15A). Unit *lsm* displays 100-200 m wide and 3-8 km long lighter-toned grooves (Fig. 16O) bounded by flat plains (see site 1 in Fig. 15B). This latter relationship contrasts grooves having a similar size and a similar trend in the nearby units (*mle* and *le*) that are rimmed by linear ridges (see site 2 in Fig. 15B).

Interpretation. The cross-cutting relationships displayed in Fig. 15 suggest a three-phase landform-development history: (i) formation of the three terrains containing radial lineations (unit *lsm, mle, and le* in Fig. 15A) attributable to the Oudemans impact, (ii) formation of the pitted and striated hummocky terrains that have a gradational relationship between each other and display shared washboard landforms (unit hm_P*and* hm_S in Fig. 15A), and (iii) creation of steep-walled troughs (units *swt-1 to swt-4* in Fig. 15A), channels (units *ch-1 to ch-3* in Fig. 15B), and southward-protruding lobate ridges (unit hm_R in Fig. 15A) that surround the striated and pitted terrains. Our interpretation that the formation of the striated terrain predates the lobate-ridged terrain is based on the following reasons. First, Fig. 15B shows that linear ridges in the striated terrain terminate in the south at the lineated smooth-surfaced unit *lsm* in Fig. 15A. The smooth-surfaced terrain at site 3 in Fig. 15B has a similar surface texture as the surface hosting the lobate-ridged terrain at site 4 of Fig. 15B. Based on this similarity, we suggest that the lineated smooth-surfaced terrain and the lobate-ridged terrain formed at the same time, which implies that the striated terrain postdates the lobate-ridged terrain. Second, linear ridges in the striated terrain trend north. If this terrain had formed after the formation of the lobate-ridged terrain, the lobate-ridged terrain would have been superposed by the same set of north-trending linear ridges, which are not observed.

Three mechanisms may be invoked to explain *individual* landforms developed during the second and third phases of the landscape development in the mapped plateau-plain area: (1) post-Oudemans-crater impact processes, (2) tectonic deformation, and (3) aeolian, fluvial and glacial erosion. Impact processes may explain pits as secondary craters (e.g., McEwen and Bierhaus, 2006) but do not explain (1) a lack of linear alignment of the pits and the absence of raised pit rims, (2) the generally non-circular shape of the pits, (3) a difficulty of relating the linear ridges to a set of radially trending ridges from any post-Oudemans impact crater, and (4) the washboard landform in the pitted and striated terrains. The lack of landform offsets and their variable trends rule out a tectonic origin for the formation of linear troughs on the plateau plains. A tectonic origin could explain the round-topped parallel ridges as folds in the striated terrain, but this interpretation faces the challenge of explaining the associated washboard landform pattern. The same issue also arises when invoking aeolian or fluvial processes to explain the washboard landform pattern, pitted terrain, and lobate ridges on the plateau plains.

The aforementioned landforms and landform assemblages can be readily explained by glacial processes. The clustered pits and their irregular map-view shapes represent kettle holes generated by dead-ice melting in glacial tills (e.g., Gerke et al., 2010), striated landforms represent streamlined subglacial landforms (e.g., Clark, 1993), lobate ridges represent recessional moraines (Chandler et al., 2016), washboard landforms represent ribbed moraines superposed on top of streamlined linear ridges (e.g., Cline et al., 2015), and elongated massive-textured mounds parallel to major northeast-trending ridges or minor northwest-trending ridges represent ice-fracture-controlled subglacial deposits. A possible Earth analogue for the mounds formed along two orthogonal sets of linear ridges is a modern glacial process reported from the Greenland ice sheet by Chudley et al. (2019). There, the subglacial deposits were controlled by the ice-sheet fracture pattern, with one fracture set perpendicular and another fracture set parallel to the ice flow direction.

The linear troughs with a systematic variation in their trends (*swt1-swt4* in Fig. 15) are interpreted as glacier-generated meltwater channels developed either below an ice sheet or along an ice-sheet margin. For a subglacial origin, the preferential distribution of these troughs on the western part of the mapped plateau plains shown in Fig. 15 may imply

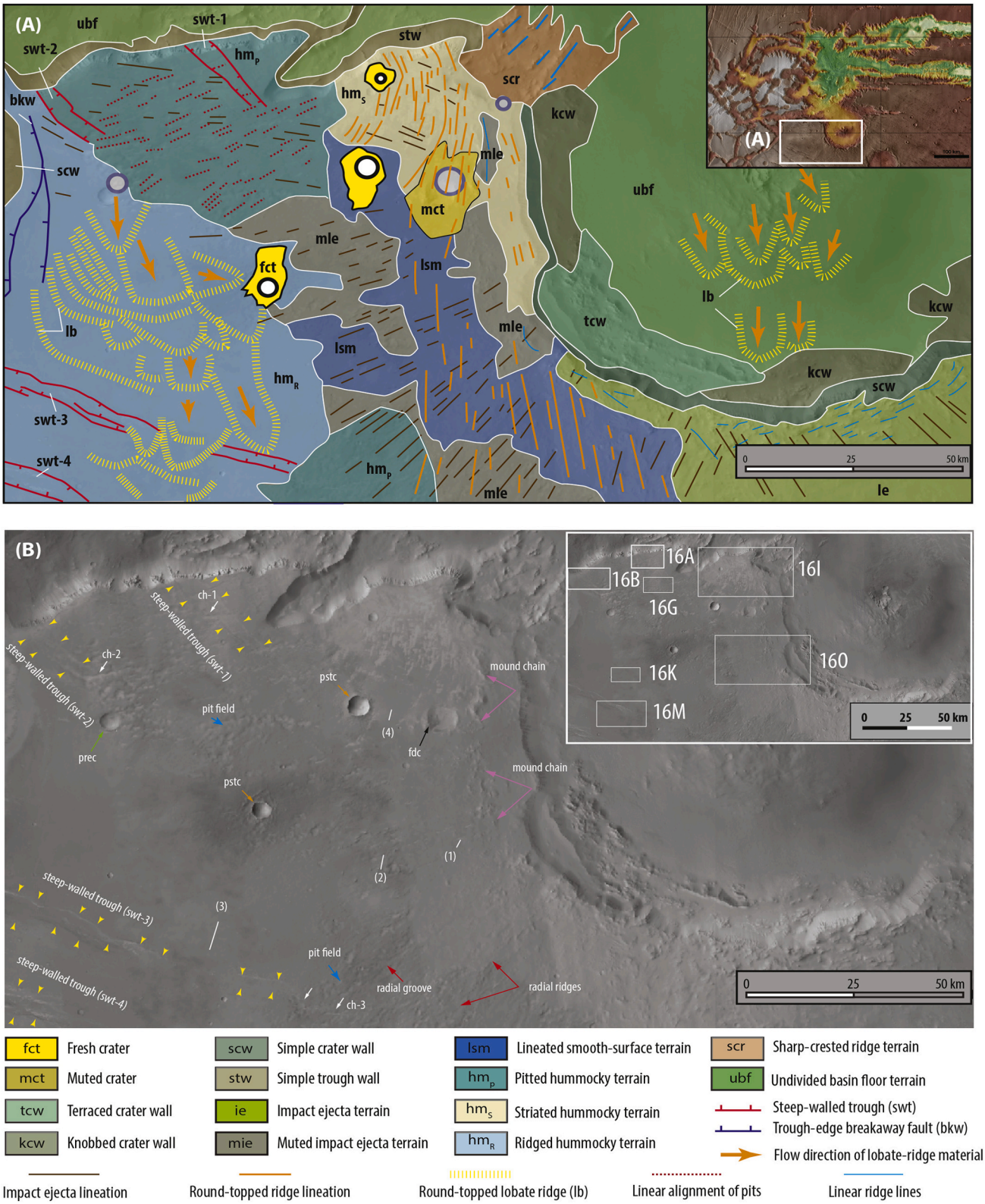

Fig. 15. (A) A geomorphic map of the crater-bounding plateau plains northwest of Oudemans crater. Interpretation is based on the CTX image shown in (B). A suite of northwest-trending steep-walled and flat-floored troughs labelled as *swt-1* to *swt-4* are spatially associated with pit fields (blue arrows). The latter are superposed on top of linear landforms that trend radially from Oudemans crater (red arrows). Linear, L-shaped, and curvilinear channels (*ch1-ch3* shown by white arrows) cut across pit fields and/or steep-walled troughs. Craters on the plateau plains display three types of morphology: (1) the rims are superposed by pits (labelled as "*prec*" and associated with a green arrow), (2) post-pit-field craters (labelled as "*pstc*" and associated with orange arrows), and (3) partially filled craters (labelled as "*fdc*" and associated with a black arrow). Also present are north-trending linear chains of mounds (pink arrows). Numbers 1, 2, 3, and 4 are sites mentioned in the text. (For interpretation of the references to color in this figure legend, the reader is referred to the web version of this article.)

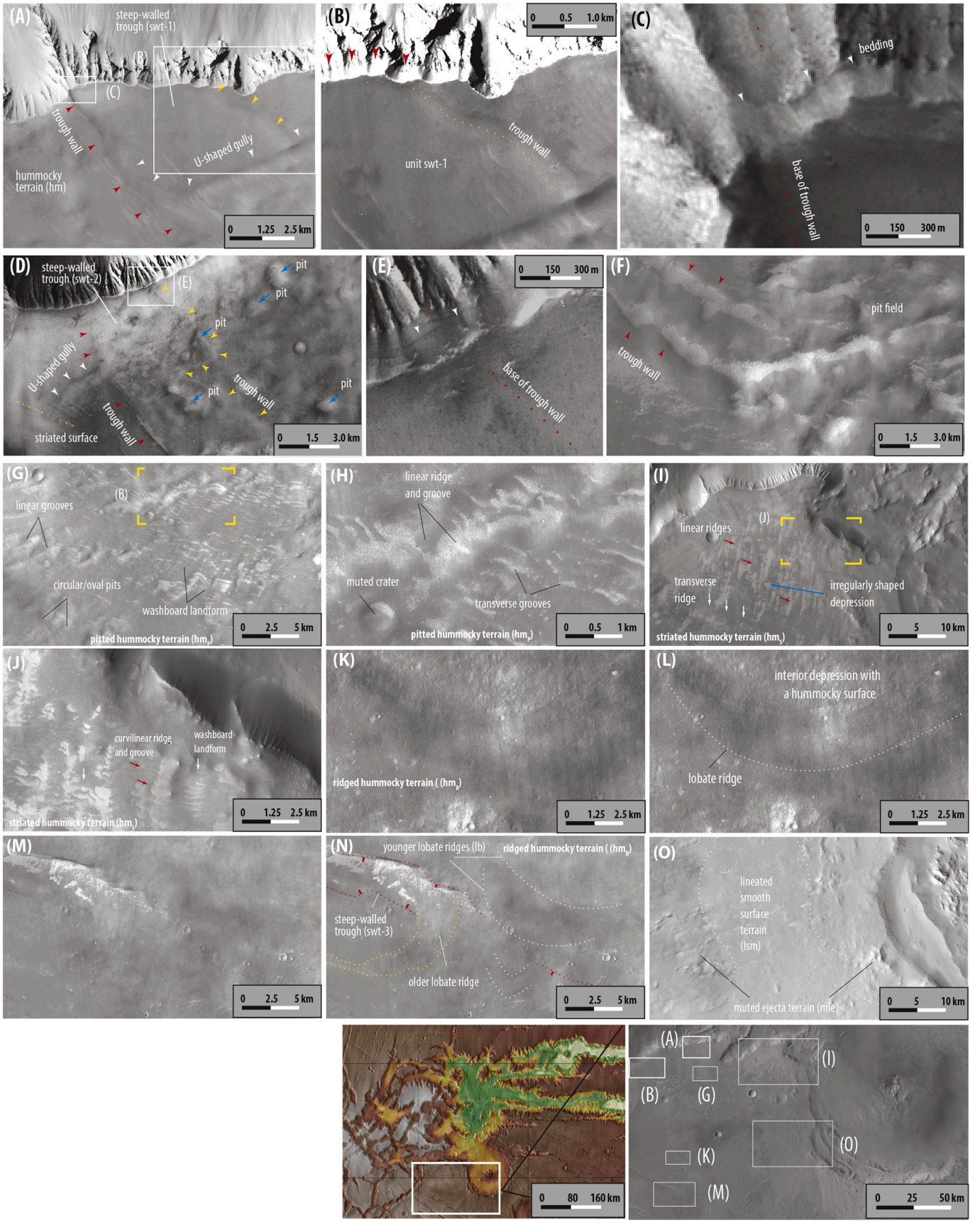

(caption on next page)

Fig. 16. (A) Northeastern margin (yellow arrows) of a linear trough (*swt-1* in Fig. 15B) that is cut across by an L-shaped gully (white arrows). The gulley turns abruptly from an east trend to a north trend westward along the base of the southwestern trough margin (red arrows). (B) The northeastern trough margin is defined by two round-topped ridges (yellow arrows). (C) Southwestern margin of the same trough, when projected along its trend (dotted red line), *does not offset beds* exposed below the trough (white arrow). (D) A linear trough (unit *swt-2* in Fig. 15) displays a Z-shaped margin in the northeast (yellow arrows) and a linear margin in the southwest (red arrows). (E) Projection of the southwest trough wall onto a cliff face where exposed beds on the cliff face below the trough are not offset. (F) A pit field that terminates a northwest-trending linear trough (red arrows). (G) and (H) Pitted hummocky terrain (unit hm_P) displays circular- and oval-shaped depressions and washboard-like landforms. (I) and (J) Striated hummocky terrain (unit hm_S) dominated by northeast-trending linear (red arrows in image I) and curvilinear ridges (red arrows in image J). This terrain is locally dotted by irregularly shaped depressions (blue arrow in image I) and displays washboard-like landforms defined by the longer northeast-trending ridges (red arrows) and shorter northwest-trending ridges (white arrows). (K) and (L) Uninterpreted and interpreted ridged hummocky terrain (unit hm_R) of a CTX image that displays convex southward round-topped lobate ridges (white dashed line). (M) Uninterpreted and (N) interpreted ridged hummocky terrain. The lobate ridges truncate and/or override a northwest-trending trough (*swt-3* in Fig. 15B) (red dotted lines). The trough that is overridden by lobate ridges itself truncates an older southward-protruding lobate ridge (yellow dotted line). (O) Lineated smooth-surfaced terrain (unit *lsm*) displays lighter-toned grooves that are 100-200 m wide and 3-8 km long. (For interpretation of the references to color in this figure legend, the reader is referred to the web version of this article.)

the presence of a polythermal ice sheet: a thicker ice sheet on the west side of the mapped area favorable for pressure melting, and a thinner ice sheet on the east side of the mapped area unfavorable for pressure melting (see chapter 7 in Cuffey and Paterson, 2010 for the related physics). It is ambiguous whether the steep-walled troughs (*swt-1* and *swt-2*) in the northern part of Fig. 15 were generated subglacially or proglacially, because the troughs are not associated with lobate ridges. For the troughs to the south that occur next to and formed coeval with the nearby lobate ridges, they may have formed as meltwater channels along the ice margin defined by the lobate ridges.

6. Discussion

Photogeologic mapping based on analysis of satellite images and digital topographic data shows that the intermediate-elevation Tharsis domain at the western end of Valles Marineris (Fig. 1A) exposes (Fig. 2B): lineated ejecta zone (*le*), crater-rim zone (*rz*), crater-wall zone (*cw*), smooth- (*sf*) and rough-surfaced (*rf*) crater-floor terrains, and central-uplift terrain (*cu*) that can be attributed to the Oudemans impact. Our mapping also reveals the superposition of a suit of younger landform assemblages over the Oudemans-impact-induced landforms. Although any single feature in the younger assemblages may be consistent with multiple formation mechanisms, the assemblages as a whole are best interpreted as products of regional ice-sheet-style glaciation. Comparison to well-documented and well-understood Earth-based landsystems and morphological features suggests that glacial processes explain the full suite of observations and are therefore the simplest mechanisms for controlling the evolving landscape of the study area after the Oudemans impact.

Glacier-induced landforms not mentioned in the early studies may in part be due to research focused on specific aspects of the region, such as alluvial fans (Moore and Howard, 2005), secondary craters (Robbins and Hynek, 2011), mega-breccia formation (McEwen et al., 2010; Mest et al., 2011), Oudemans-impact-induced structures (Kasmai, 2014), and mineral compositions (Caudill et al., 2011; Tirsch et al., 2011; Quantin et al., 2012; Sun and Milliken, 2015). Data resolution may also prevent glacial interpretations in early studies before sub-meter-resolution images were used in regional mapping (Witbeck et al., 1991; Tanaka et al., 2014). As shown in this study, the relationship between the shape of a landform and the surface texture with an implied composition (e.g., boulders) of the landform material could only be defined when the HiRISE images are used in the analysis of landform-forming processes.

6.1. Mega-scale glacial lineations (MSGLs) on Mars

Mega-scale glacial-lineation (MSGL) terrains on Earth are considered to have formed under ice streams within topographically unconstrained regional ice sheets, such as those in Antarctica and Greenland, or the Quaternary Laurentide ice sheet in North America (Clark, 1993; Clark and Stokes, 2003; Stokes, 2018). To test whether the lineated landforms in our mapped striated terrain are MSGLs on Mars, we created a more detailed geomorphologic map (Fig. 17A cf., Fig. 17B) that allows an in-depth discussion on the issue. The map shows that the linear ridges and grooves defining the possible mega-scale glacial lineations on Mars are superposed by irregularly shaped depressions (unit *ird*) and massive-textured mounds (unit *kb*). The largest mounds (unit *kb_L* in Fig. 17A) are elongated in the northeast direction parallel to the trend of the major linear ridges (see the lower right part of Fig. 17A), whereas the smaller mounds (unit *kb_S* in Fig. 17A) are elongated in the northwest direction parallel to the minor transverse ridges (see the lower left part of Fig. 17A). As noted earlier, the striated hummocky terrain is the source of a viscous flow feature (i.e., VFF following the definition of Milliken et al., 2003) (Figs. 3I and 17A), which suggests that the striated-terrain material is not bedrock.

Fig. 17A (cf. Fig. 17B) shows that the major northeast-trending linear ridges have a consistent northeastward-tapering map-view shape (indicated by blue, yellow, and red arrows for three such features), which is expressed by a wider ridge segment in the south that splits into several smaller narrower northward-tapering ridges in the north (see the example outlined by the yellow arrows). The dominant northeast-trending ridges have lengths of 2 to 17 km, widths of 2 to 6 km superposed by minor parallel ridges, and an average length to width ratio of ~9 (Figs. 17C-17E). The typical spacing of the major linear ridges is about 4-6 km and the ridge-trough elevation difference varies from ~30 m to >100 m as shown in two topographic profiles constructed using the HRSC-MOLA blended DEM data at the resolution of 200 m/pixel (Figs. 17D and 17E). Below, we compare the above observations against the well-established geometric attributes of MSGLs on Earth.

Spagnolo et al. (2014) conducted a systematic morphometric analysis of 4043 MSGLs from eight best-documented MSGL terrains on Earth, which include those created by modern ice sheets and those formed in the Quaternary period. These authors showed that the average length, width, and aspect ratio of MSGLs on Earth are ~2900 m, ~270 m, and ~9, respectively. Individual studies show, however, that departures from the above mean values could be as high as a factor of 2 to 3 even within the same MSGL terrains (Stokes et al., 2006; Storrar and Stokes, 2007). Fig. 17C shows that the average length and width values of the MSGLs tabulated by Spagnolo et al. (2014) with a factor of 2 uncertainty against the data from the striated terrain mapped in this study on Mars. The width and length values from the Earth alone are plotted at the lower end of the Mars data, but the length-to-width ratio is the same at ~9 for data from both planets (Fig. 17C). The similar aspect ratio requires a controlling factor independent of gravity, which may include the rheological properties of subglacial tills and overlying ice that are independent of gravity (see discussion below). The overlapping range of terrestrial and martian geometric parameters (Fig. 17C) led us to suggest that the striated terrain in our study area represents a MSGL terrain on Mars. This interpretation implies the presence of a regional ice sheet on the plateau plains in the central Tharsis rise region as required by the MSGL analogues on Earth.

To further assess the MSGL hypothesis, we compare the linear landforms in our mapped striated terrain (Fig. 18A) with two terrestrial

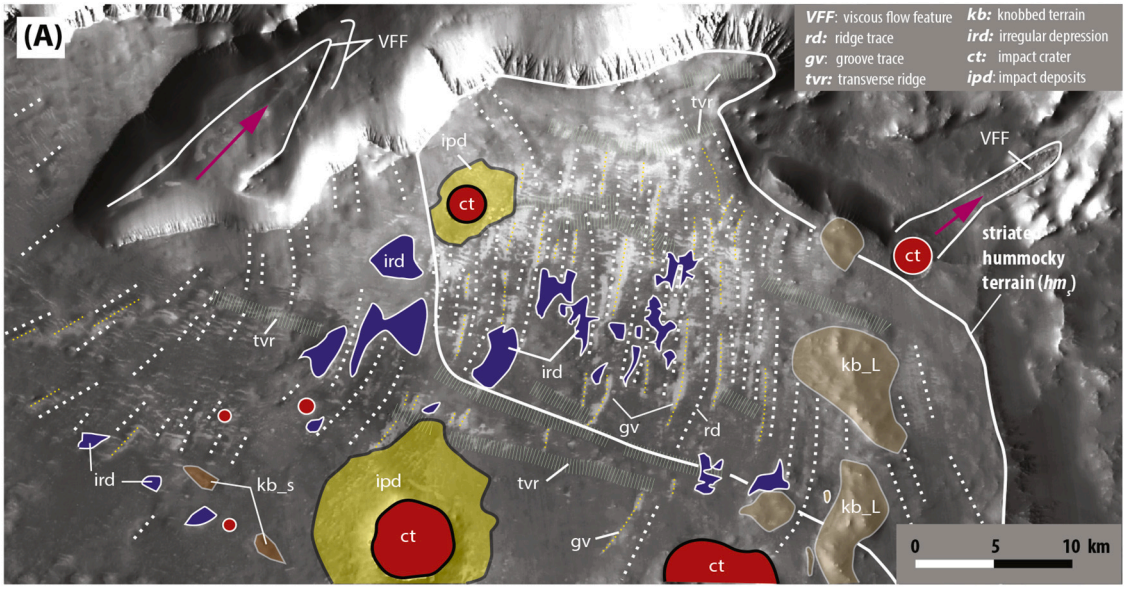

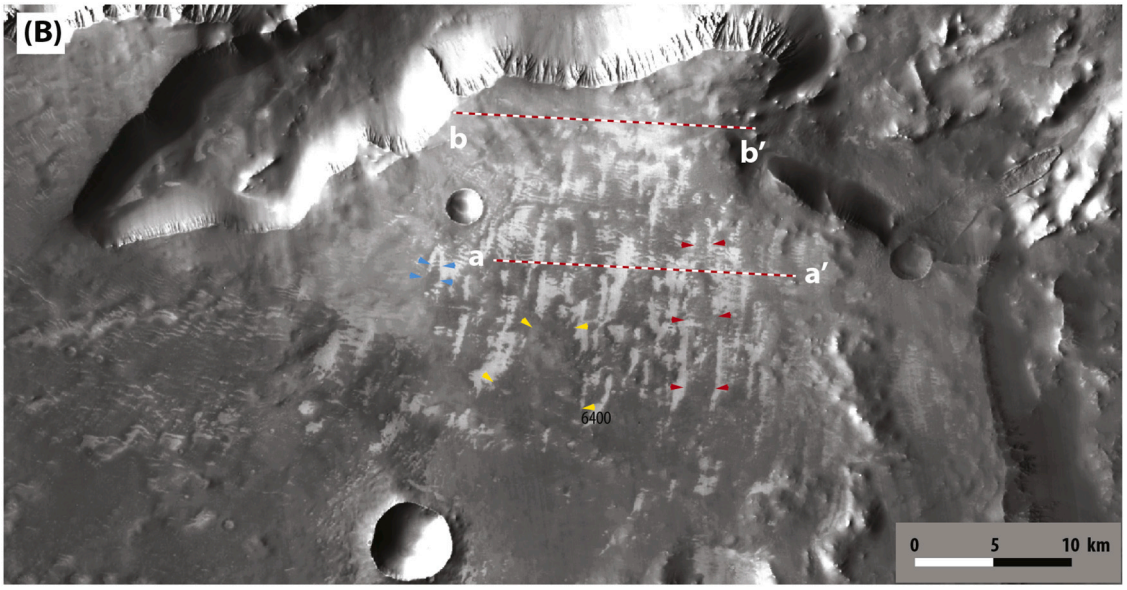

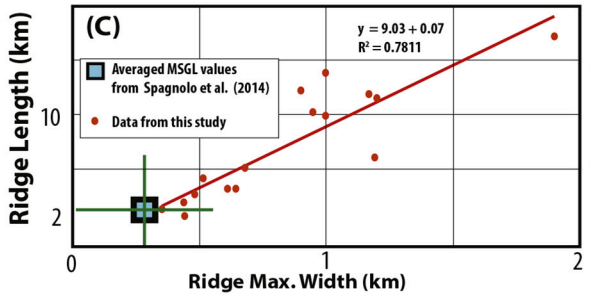

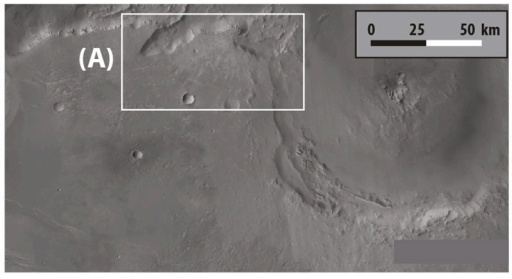

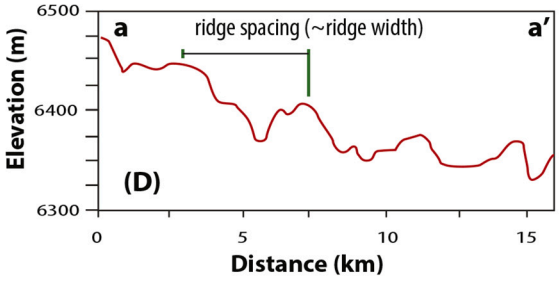

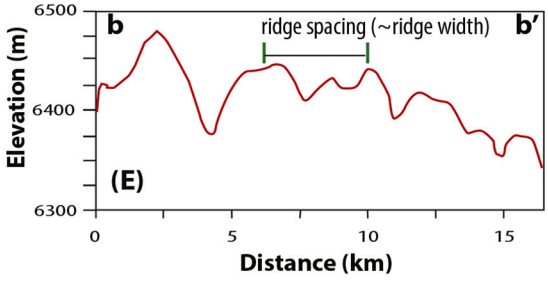

(caption on next page)

Fig. 17. (A) Interpreted and (B) uninterpreted CTX image of the striated hummocky terrain northwest of Oudemans crater. Geomorphologic map in (A) shows the linear landforms in the striated terrain are superposed by irregularly shaped depressions (unit *ird*) and massive-textured mounds (unit *kb*). Larger mounds (unit *kb_L*) are elongated and/or aligned linearly in the northeast direction parallel to the main trend of the longer ridges in this terrain. The smaller mounds (unit *kb_S*) are elongated and aligned in the northwest direction parallel to the minor transverse ridges. (C) A plot of ridge length vs. maximum ridge width for the northeast-trending ridges in the striated terrain shown in (A). The ridges have lengths from 2 to 17 km, widths from 0.5 to 2 km, and an averaged length vs. width ratio of ~9. Also shown is the average width and length of MSGLs from Earth with a factor of 2 uncertainties from the averaged values. See text for details. (D) and (E) Topographic profiles constructed using the HRSC-MOLA blended DEM data across the striated hummocky terrain with profile locations shown in (B).

MSGL terrains created by the Quaternary Laurentide ice sheet in Canada (cf. Figs. 18B and 18C). Note that all three figures in Figs. 18A-18C are shown at the same scale. The images of the terrestrial MSGL terrains were obtained from Google Earth in areas where MGSLs were systematically mapped by Stokes et al. (2006) and Storrar and Stokes (2007). We note that the striated hummocky terrain in our study area and the Quaternary MSGL terrains on Earth share the following similarities: (1) long linear ridges (red arrows) are superposed by shorter transverse ridges (white arrows), (2) the superposed orthogonal ridges display a washboard-like pattern, (3) irregularly shaped depressions (yellow arrows) are dotted on the surface of linear ridges and grooves, (4) linear ridges are round-topped, and (5) ridge widths narrow from central segments towards terminal segments (Figs. 18A-C).

Modern and paleo-MSGL terrains share many similarities but also display important differences in morphology. The modern MSGL terrains, recently exposed from below active ice sheets, may display continuous ridge traces with uniform ridge widths and a smooth ridge-surface morphology (red arrow in Fig. 18D) (Spagnolo et al., 2014; also see Dowdeswell et al., 2020). In contrast, Quaternary MSGL terrains typically exhibit discontinuous ridge traces, hummocky ridge-surface textures, and variable ridge widths (red arrows in Figs. 18B and 18C). A possible explanation for these differences is that modern MSGLs still contain dead-ice blocks, whereas older Quaternary MSGL terrains have the dead-ice blocks removed that led to the formation of rough-surfaced ridges, variable ridge widths, and discontinuous ridge traces (Figs. 18B and 18C; cf. Fig. 18D).

Quaternary MSGLs with flat- and round-topped ridges (white arrow) may be superposed by transverse ridges (blue dashed line), which is expressed by a washboard landform pattern (e.g., Cline et al., 2015) (Fig. 18E). This Earth example of glacier-generated washboard landforms shows a similar size and a similar morphology to the washboard landform pattern displayed in our mapped pitted and striated terrains (see Figs. 15A and 15B; cf. Fig. 18F). This similarity further supports the hypothesis that the striated terrain in our study area represents a MSGL terrain on Mars, similar to those documented on Earth (e.g., Stokes et al., 2006; Cline et al., 2015; Möller and Dowling, 2018). The transverse ridges may have formed by crevasse squeezing (Hättestrand and Kleman, 1999) and/or compressional flows (Stokes et al., 2008).

We note that the exact mechanism for MSGL formation on Earth remains poorly understood and hotly debated. However, the new observations from Mars based on the above discussion may provide a fresh perspective on this important issue in glacier physics. Current models invoke basal-ice irregularities ploughing into softer subglacial tills (Tulaczyk et al., 2001; Clark et al., 2003), subglacial mega-floods (Shaw et al., 2008), kinematic-wave and/or rheological-contrast triggered instability at the ice-till interface (Hindmarsh, 1998; Fowler and Chapwanya, 2014), and coeval erosion and deposition of subglacial tills below fast-moving ice streams (Barcheck et al., 2020). Establishing which of the above mechanisms was responsible for the formation of the striated terrain on Mars may allow us to relate spacing, length, and length-width ratio of MSGLs to the dynamics and size/thickness of the involved ice sheet. As the aspect ratio of MSGLs on Earth and Mars is the same at ~9 (Fig. 17C), we suggest that the mechanism involving the viscous-creep instability at the ice-till contact (i.e., Hindmarsh, 1998; Fowler and Chapwanya, 2014) would be the most plausible explanation of MSGL formation on both planets, as this mechanism does not involve gravity.

Regardless of how MSGLs may have formed, direct measurements from the base of active ice streams on Earth indicate that the basal water pressure is very close to the overburden pressure of the ice sheet (Engelhardt and Kamb, 1997; Kamb, 2001). This observation suggests that meltwater along the base of our inferred ice sheet would also have been present when the MSGL terrain (= striated terrain) was developed on Mars. Although no channel-like features are present within our mapped striated terrain (Fig. 17A), we note that this observation is not uncommon for MGSL terrains on Earth (e.g., Sookhan et al., 2018). A possible explanation for this observation on both planets is that the subglacial channels are transient landforms constantly erased by continued shear deformation of the soft subglacial tills that host the episodically formed subglacial meltwater channels.

Based on the above interpretation, the northeastward-tapering and northeast-trending ridges in the striated terrain in our study area (Fig. 17A) is a result of a northeastward glacial flow on the plateau surface. This flow direction is opposite to the southward glacial flow suggested by the shape of the younger lobate ridges on the plateau plains (Fig. 15A). These observations and implied interpretations can be reconciled by the occurrence of two phases of glacial flow in opposite directions on the plateau plains. This inference is supported by the observation from the nearby sharp-crested ridge terrain, where the streamlined ridge shapes also indicate two phases of northeastward and southwestward glacial flows (see Fig. 3E and related discussion). Although landforms mapped across the Oudemans central uplift also indicate local northward glacial flows (see Figs. 4 and 8 and related discussion), these flows should have postdated the main phase of southward-flowing glaciation based on the cross-cutting relationships discussed above.

A possible landsystem evolution for the formation of the striated hummocky terrain is shown in Figs. 18G-18H. During glaciation (Fig. 18G), dead-ice blocks are embedded in subglacial tills and streamlined ridges (= MSGLs) that display a smooth surface texture. After the end of glaciation (Fig. 18H), the removal of the dead-ice blocks by ice melting created a hummocky surface texture on the streamlined MSGLs. The two-stage model may also explain the morphological difference between the modern and Quaternary MSGL terrains on Earth as mentioned earlier (cf. Figs. 18B and 18C).

6.2. *Glacial modification of Oudemans crater morphology and ice-sheet evolution*

Post-impact modification of Oudemans crater is best illustrated by comparing its morphology against a smaller crater that preserves a full set of complex-crater features. Fig. 19A shows a DEM map of Oudemans crater and Fig. 19B shows a DEM map of a smaller crater (D = ~50 km) on the Tharsis rise centered at 290.84° E and 21.389° S using the same color elevation scale. The smaller crater displays (1) a well-preserved central uplift that has an irregularly shaped moat, (2) discontinuous ridge segments that bound the outer rim of the moat, (3) a circular central peak bounded by the moat, (4) a sharp-crested and nearly continuous rim ridge, and (5) a sharp-crested and nearly continuous ridge in the crater-wall zone (Fig. 19B). In contrast, the morphology of Oudemans crater differs markedly from that of the smaller crater: its central uplift lacks the moat and rimmed ridges, its central peak is non-circular, and its crater rim and crater wall lack both ridge continuity and ridge-crest sharpness encircling the crater basin (Fig. 19A; cf. Fig. 19B). The above comparison strengthens our interpretation that Oudemans crater has been modified significantly by younger resurfacing processes.

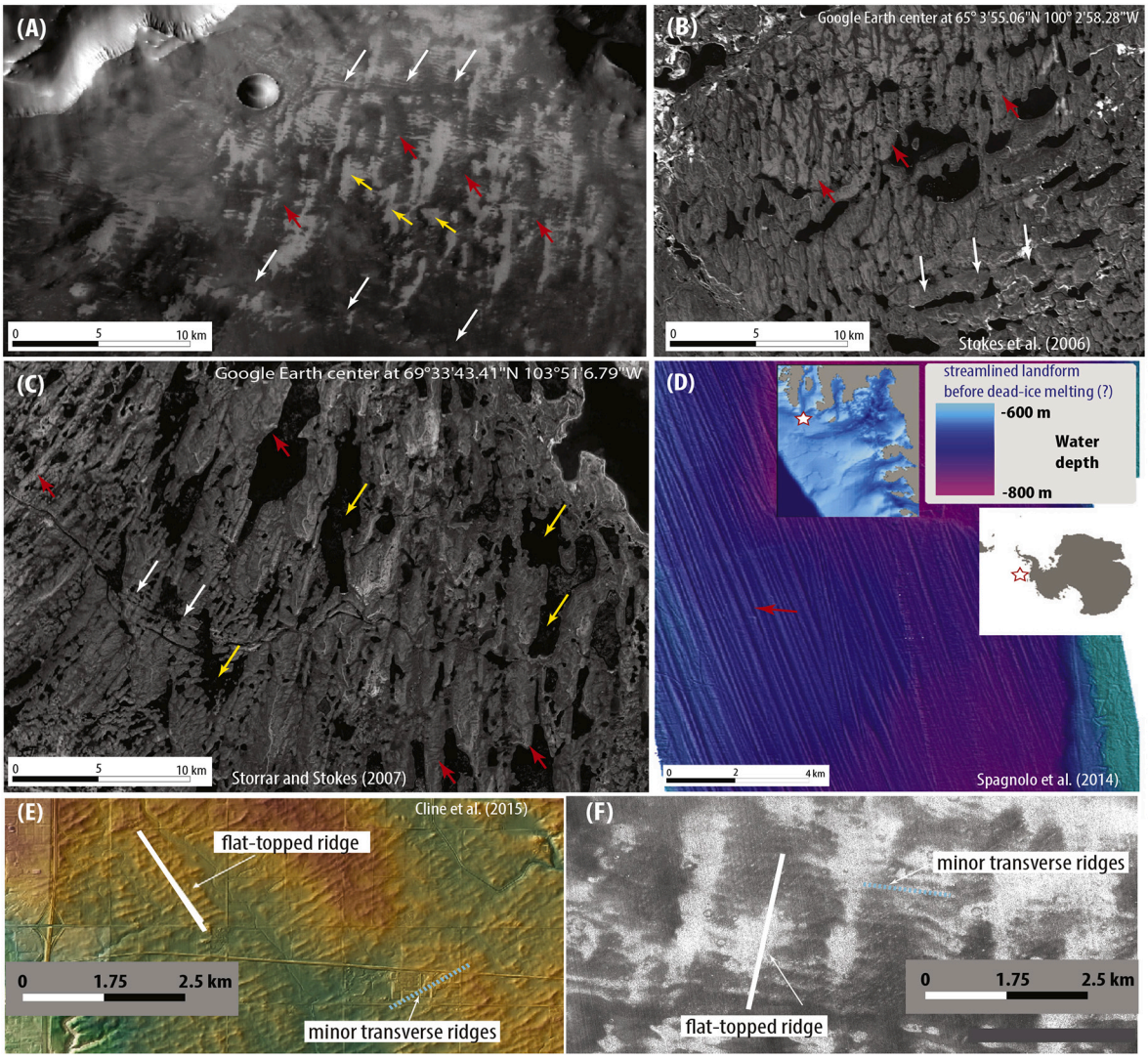

(caption on next page)

Fig. 18. (A) Linear landforms from the striated hummocky terrain mapped in this study. (B) and (C) are Google Earth images of Quaternary MSGL terrains from Canada that are displayed at the same scale as the striated terrain from Mars in (A). Landforms in the two areas from Canada were mapped by Stokes et al. (2006) and Storrar and Stokes (2007), respectively. Similarities between our interpreted MSGL terrain (= striated terrain) on Mars and the MSGL terrains from the Earth include: (1) longer linear ridges (red arrows) up to >10 km in length, (2) the long ridges are superposed by shorter transverse ridges (white arrows) with a washboard-like landform, (3) the longer ridge surfaces for the Quaternary and Mars MSGL terrains exhibit irregularly shaped depressions (yellow arrows), (4) the ridge crests are round-topped, and (5) ridge widths taper from the central segments towards the ridge terminations. (D) A modern MSGL terrain that shows continuous linear ridge traces, uniform ridge widths, and smooth ridge surfaces (red arrow). The figure is adopted and modified from Spagnolo et al. (2014). Note that the landform of the modern MSGLs differs from that of the discontinuous and variable-width ridges in Quaternary and Mars MSGL terrains. (E) Quaternary MSGLs with flat-topped ridges (white arrow) and transverse ridges (blue dashed line) are associated with a washboard-moraine pattern. The figure is modified from Cline et al. (2015). (F) Similar size and similar morphology of the washboard landform to those shown in (E) from the striated terrain in our study area. (G) and (H) show a possible explanation for the morphological difference between modern and Quaternary/Mars MGSL terrains and the evolution of the striated terrain in our study area. In (G): dead-ice blocks are embedded in subglacial tills before being removed by melting. The landform at this stage is expressed by smooth-surfaced ridges and grooves and even-width ridges and grooves. In (H): removal of dead-ice blocks by melting created hummocky surfaces on the streamlined MSGLs, discontinuous ridge traces, and variable ridge widths. The transverse ridges may have been generated by crevasse-squeezing as shown. (For interpretation of the references to color in this figure legend, the reader is referred to the web version of this article.)

A possible modification history of the Oudemans crater basin is shown in Fig. 19. On the plateau plains, an ice stream in a northward-flowing northward-advancing ice sheet created mega-scale glacial lineations (MSGLs) in the striated terrain discussed above (Fig. 19C). The northward-advancing glacier may have filled up the Oudemans crater basin, the Triple Intersection Basin, and the nearby troughs of Noctis Labyrinthus and Valles Marineris. The northward glacial flow was followed by a southward glacial flow across both the Oudemans crater basin and the plateau plains (Fig. 19D). The younger southward glacial flow was associated with a northward glacial-front retreat, indicated by a south-facing ice margin expressed by the development of lobate ridges and the interpreted margin-parallel meltwater channels (Fig. 19E). Relict mountain glaciers on top of the central uplift of Oudemans crater flowed downhill during the waning stage of deglaciation (Fig. 19F).

6.3. *Hiawatha crater in Greenland and Oudemans crater on Mars*

A possible analogue for the relationship between Oudemans crater and its bounding plateau plains under the influence of a regional ice sheet is the complex Hiawatha crater with a diameter of ~35 km buried below the ~3-km thick Greenland ice sheet (Kjær et al., 2018) (Fig. 20A). Due to glacier-induced erosion, its central uplift is mostly eroded away with only a few isolated knobs remained (Kjær et al., 2018) (Figs. 20A and 20E). This observation testifies to the effectiveness of glacial erosion in removing impact-induced landforms. The northern wall of Hiawatha crater has been partially eroded away by the action of meltwater flow along subglacial channels (Kjær et al., 2018) (Fig. 20A; cf. Fig. 20C). As time progresses, the Hiawatha northern crater wall will eventually be removed, exhibiting a crater morphology similar to that of Oudemans crater (Fig. 20B; cf. Fig. 20D).

To place our observations in a context comparable to the morphological features from the Hiawatha crater area, we show the location and sequence of the inferred glacial flow events from the Oudemans crater area in Fig. 20B: (1) an older northward-flowing glacier developed on the plateau (*feature B*), (2) a coeval southward-flowing glacier moved across the central uplift, crater floor (*feature C*), and the plateau plains (*feature A*), (3) a south-facing ice margin on the plateau plains (*feature A*), and (4) the youngest and local northward-flowing mountain glaciation across the central uplift of Oudemans crater (*feature D*). When comparing Hiawatha and Oudemans craters, we find the following shared morphological features (Figs. 20A and 20B; cf. Figs. 20C and 20D): (1) steep-walled troughs with undulating long profiles cutting into the bounding plateau plains (see *feature 1* and consult with the color elevation scale), (2) these troughs are expressed by chains of linked oval-shaped depressions with a similar size (*feature 1*), (3) shorter U-shaped troughs link the crater basins with the bounding plateau plains (*feature 2*), (4) the northern crater walls are either completely or partially removed (*feature 3*), (5) central uplift peaks are non-circular (*feature 4*), (6) linear steep-walled troughs are present around the crater basin (*feature 5*), and (7) orthogonal terminations of steep-walled troughs (*feature 6*) (Fig. 20A; cf. Figs. 3D and 16A).

Based on the above similarities, we interpret steep-walled troughs consisting of chained oval-shaped depressions (*feature 1*) and troughs having U-shaped cross sections (*feature 2*) in our mapped dissected terrain to have been created during the formation of subglacial meltwater channels. This interpretation follows that proposed by Kjær et al. (2018) for the similar morphological features around Hiawatha crater below the Greenland ice sheet. We further suggest that the erosion of the northern wall (*feature 3*) and central uplift of Oudemans crater (*feature 4*) (also see Figs. 20A, 20C, and 20E; cf. Figs. 20A and 20D) were induced, at least in part, by glacial erosion (see further discussion below on this issue).

The interpreted foreland meltwater channels next to Oudemans crater on the plateau plains are subparallel to the ice margin, whereas the foreland meltwater channels next to the Hiawatha glacier are orthogonal to its respective ice margin. This difference can be explained by the local topographic settings of the two ice margins. For the Hiawatha glacier, the elevation of the proglacial region is lower than that of the ice margin (Fig. 20A), which allows downslope meltwater flow. In contrast, the elevation of the proglacial region for the plateau plains next to Oudemans crater on Mars is higher than our inferred ice margin (Fig. 20F), which would have favored meltwater to flow along, not away from, the ice margin.

The topographic profile shown in Fig 20F implies that the ice sheet on the plateau plains was at least ~300 m thick at the waning stage of the south-flowing north-retreating glaciation on the plateau plains. If Oudemans crater was completely filled by glaciers as shown in Fig. 19A, its 4-km relief requires the ice sheet over the crater basin to be at least 4 km in thickness (see Fig. 1B). For a diameter of 125 km and a depth of 4 km, the above interpretation would yield an ice volume of ~200,000 km^3 stored in the Oudemans crater basin alone, which is about one-fifth of the north polar layered deposits (NPLD) composed of ≥95% pure water ice (Grima et al., 2009). Such an estimate would support the hypothesis that Valles Marineris was once filled by a trough-glacier system with an estimated volume on the order of one million km^3 by Gourronc et al. (2014), which is interestingly similar in volume to that of the NPLD. Establishing the interconnectedness of ice bodies (i.e., plateau ice sheets, trough glaciers, and mountain glaciers) among troughs and basins in Noctis Labyrinth, Valles Marineris, Triple Intersection Basin, and Oudemans crater in the future will be critical in testing competing mechanisms for the formation of the giant circum-Tharsis outflow channels (e.g., Carr, 1979; Baker et al., 1991; Malin and Carr, 1999; Nimmo and Tanaka, 2005; Baker et al., 2000; Baker, 2001; Harrison and Grimm, 2004; Andrews-Hanna and Phillips, 2007; Cassanelli et al., 2015; Cassanelli and Head, 2019).

The interpreted glacier-induced resurfacing event across Oudemans crater and its bounding plateau plains may resolve several puzzling observations: (1) the lack of alluvial fans on the Oudemans crater floor (Moore and Howard, 2005) may be explained by glacier-induced erosion after earlier fan construction, (2) the absence of secondary craters

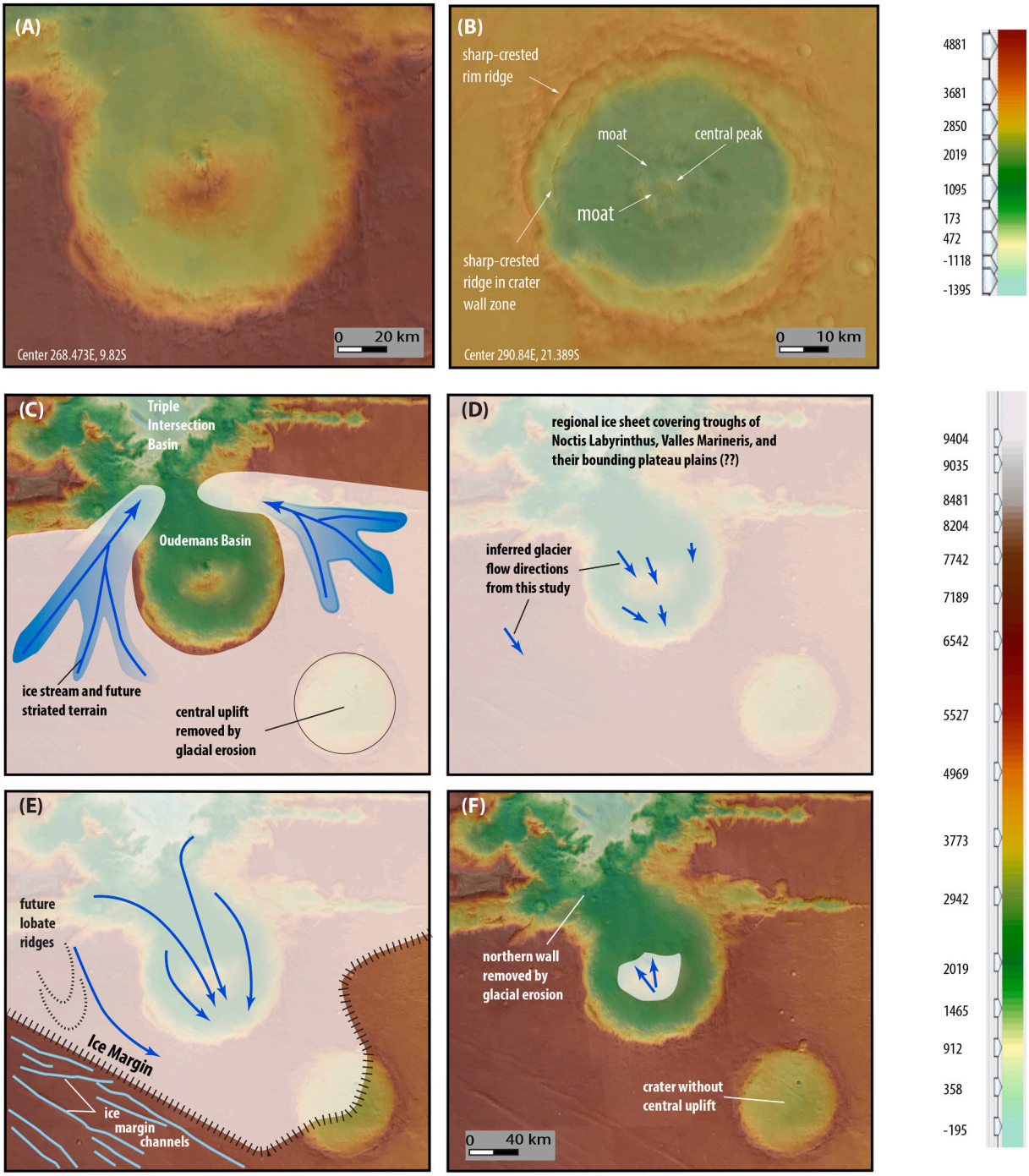

Fig. 19. Comparison of Oudemans crater (A) with a fresh complex crater exposed in eastern Tharsis (B). See text for details. (C)-(F) show a possible sequence of glaciation events that have modified the morphology of Oudemans crater. (C) Time 1: A northward glacial flow from the plateau plains that may have filled up the Oudemans crater basin, troughs of Noctis Labyrinthus and Valles Marineris, and the Triple Intersection Basin. (D) Time 2: A southward glacial flow from the Triple Intersection Basin and Oudemans crater over the plateau plains. (E) Time 3: The southward glacial flow continued on the plateau plains while its ice margin was retreating northward. (F) Time 4: Relic mountain glaciers flowed northward during the waning phase of deglaciation in the central uplift of Oudemans crater.

around Oudemans crater (Robbins and Hynek, 2011) may be explained also by post-Oudemans-impact glacier-induced erosion and deposition, and (3) the half-circled Oudemans central uplift and an isolated ridge complex hosting U-shaped valleys (Fig. 3) could have been produced by erosion mostly during a southward-flowing glaciation event.

6.4. Missing northern wall of Oudemans crater and a glacial origin for the shared basin floor in western Valles Marineris

A first-order observation at the western end of Valles Marineris is the shared basin floor among troughs of Valles Marineris and Noctis Labyrinthus, the Triple Intersection Basin, and the Oudemans crater basin. As pointed out in the introduction, this observation requires a unified geological process to connect the originally isolated troughs and basins having drastically different formation origins (e.g., impact vs. rifting).

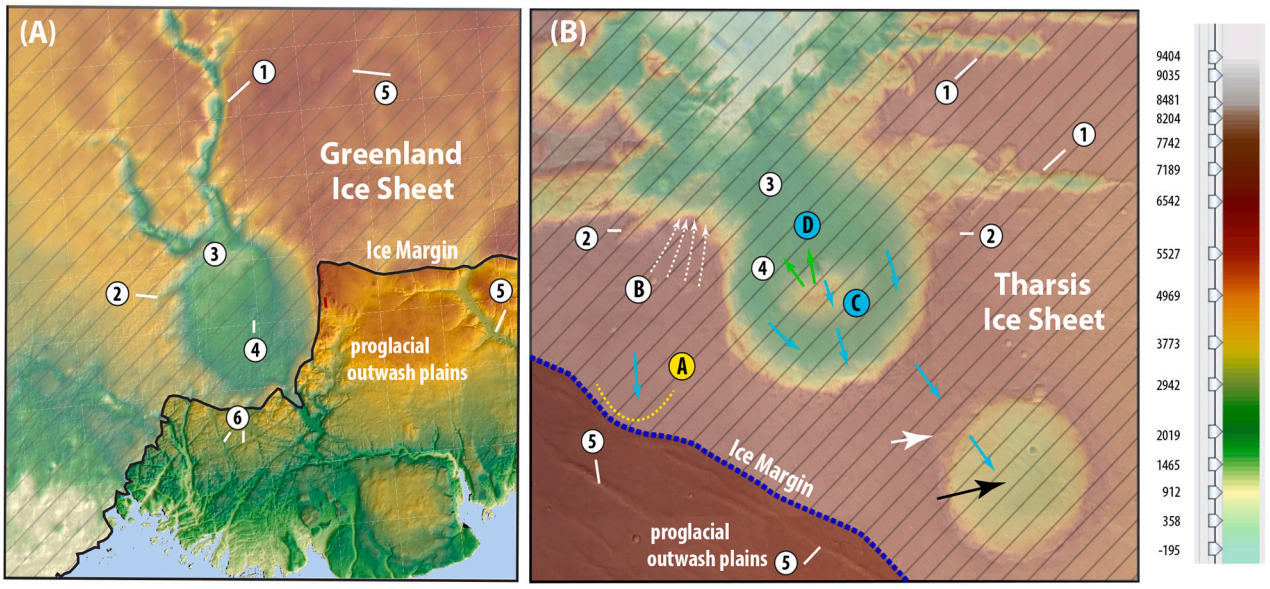

Correlative features between Hiawatha crater on Earth and Oudemans crater on Mars: 1 = steep-walled troughs with undulating long profiles expressed by chains of linked oval-shaped depressions, 2 = U-shaped valleys linking crater basins with bounding plateau plains, 3 = missing segments of crater walls, 4 = non-circular relics of the central uplifts, 5 = linear steep-walled troughs, 6 = orthogonally terminating linear gullies. Glacier flow directions inferred from this study: A = ice-stream flow predating southward glacier flow; B = convex southward lobate ridge formed during southward glacier flow; C = flow directions inferred from interpreted glacial landforms on crater floor and crater central uplift.

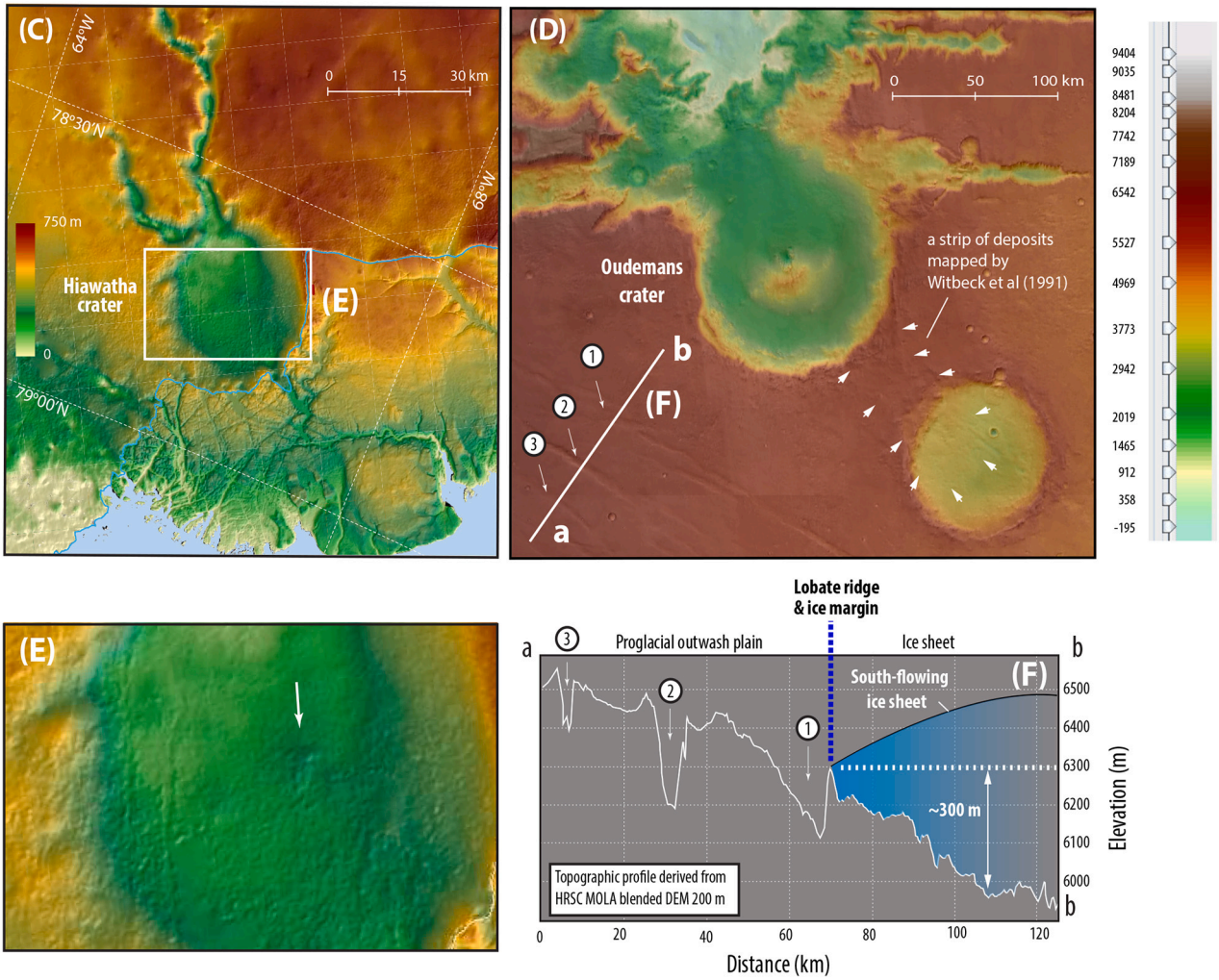

(caption on next page)

Fig. 20. (A) A DEM map of Hiawatha crater below and in front of the Greenland ice sheet after Kjær et al. (2018). Numbers are glacially induced features (see explanation below the figure). Compare to (C), which is the uninterpreted DEM map modified from Kjær et al. (2018). (B) A AA DEM map of the Oudemans crater area that displays interpreted impact and glacial features comparable to those shown in (A) from the Hiawatha crater area on Earth. The uninterpreted DEM map is shown in (D). Features comparable between Hiawatha and Oudemans craters include: (1) steep-walled troughs with an undulating long profiles (*feature 1*) and chains of linked oval-shaped depressions (*feature 1*), (2) U-shaped valleys linking crater basins with bounding plateau plains (*feature 2*), (3) a missing segment and partially destructed segment of the northern crater wall (*feature 3*), (4) a non-circular central uplift (*feature 4*), (5) linear steep-walled troughs (*feature 5*), and (6) orthogonally terminating gullies/troughs (*feature 6*) (cf. Figs. 3D and 16A). (E) A closer view of Hiawatha crater where the central uplift has been largely eroded away except a few subtle knobs (white arrow). (F) A topographic profile across the interpreted ice margin on the crater-bounding plateau plains. See (D) for location. The profile cuts across the proposed ice margin and ice margin channels. Note that the ice margin faces upslope in the plot, which is opposite to the situation shown in (A) for the Hiawatha glacier that has a foreland plain dipping away from the ice margin.

Below, we use the missing northern wall of Oudemans crater as a focal point of discussion on this issue.

Early studies (Mest et al., 2011; Osinski et al., 2011; Kasmai, 2014) suggest that the absence of the northern wall of Oudemans crater could have been caused by a northward-plunging oblique impact. Support for this hypothesis is the presence of isolated light-toned and internally layered blocks in the Triple Intersection Basin north of the Oudemans crater basin. These blocks share similar albedos, surface textures, and internal layering to rocks exposed in the central uplift of Oudemans crater (Mest et al., 2011; Osinski et al., 2011). The blocks were interpreted as impact breccia transported by the proposed northward plunging oblique Oudemans impact (Mest et al., 2011; Osinski et al., 2011). Although this hypothesis is supported by the similar morphology of Oudemans crater to that of oblique impact craters on Earth (Mest et al., 2011; Osinski et al., 2011) (also see Earth examples of oblique impact craters in Schultz and D'Hondt, 1996 and in Schultz and Anderson, 1996), the current morphology of Oudemans crater has been modified by younger resurfacing processes that were not considered by the early studies. As demonstrated in this study, light-toned and internally layered breccias could be parts of subglacial tills transported by regional glaciation (see Figs. 12A-12C and related text). In light of this finding, the blocks with similar appearances to the central-uplift rocks of Oudemans crater now in the Triple Junction Basin could be alternatively interpreted as glacial erratics.

For an end-member case in which the northern wall was completely removed by glacial erosion, we envision that a strip of crustal section had existed between the Triple Intersection Basin and Oudemans crater prior to our inferred regional glaciation. During southward-flowing glaciation with ice mass transported from the Triple Intersection Basin into the Oudemans crater basin, the base of the ice sheet may have exhibited a mechanical condition similar to what is illustrated for the development of a roche moutonnée in Fig. 8G. In this scenario, pressure melting occurring on the stoss (north and up-flow) side and hydrofracturing occurring on the lee (south and down-flow) side would have preferentially removed the lee-side bedrock (see chapter 7 in Cuffey and Paterson, 2010 and Iverson, 2012 for the involved physics and mechanics). This process could have also been associated with the development of subglacial channels and related erosional process analogous to the modern situation displayed at the northern wall of Hiawatha crater (Fig. 20A). As time progressed, glacial erosion would have removed the northern wall of Oudemans crater.

A similar process may have also occurred across the central uplift of Oudemans crater. However, the incomplete removal of the central uplift may have resulted from the difference in the mechanical strength between the crater-wall and central-uplift rocks. Recall that the central-uplift rocks were excavated from a deeper crustal level below the impact-basin floor (Melosh, 1989), and the scaling relationship requires an excavation depth of ~13 km for the Oudemans central-uplift rocks measured from the surface of the plateau plains (e.g., McEwen et al., 2010; Mest et al., 2011; Quantin et al., 2012). A mechanically stronger central-uplift rocks would have led to a slower erosion rate, allowing it to be partially preserved; meanwhile the weaker northern wall would have been completely removed under the same glacial action. Although the subsurface geology of the glacier-covered Hiawatha crater is unknown, we speculate that the relative strength of the crater-wall and central-uplift rocks may be opposite to that of Oudemans crater. That is, the strength of the Hiawatha central-uplift rocks may be lower than that of the wall rocks, which allows the crater wall to be partially preserved while the central uplift to be rapidly and nearly completely removed (Fig. 20A).

The involvement of a southward-flowing glacier across the apparently intact southern Oudemans crater wall is evident from the following discussion. On Mars the transition diameter from simple to complex craters is ~7 km (Robbins and Hynek, 2011). An unnamed crater with a diameter of ~88 km and located ~70 km south of Oudemans crater lacks a central uplift (black arrow). We note that its northern raised crater rim (white arrow) is missing (Fig. 20B). Associated with the missing northern rim is a strip of surficial deposits (white arrows in Fig. 20D) extending from the southern rim of Oudemans crater to the center of the unnamed crater that was mapped by Witbeck et al. (1991). The deposits have a tongue-shaped landform inside the unnamed crater with a lobate-shaped southward-protruding front (Witbeck et al., 1991). Witbeck et al. (1991) attributed the unit to the Oudemans impact, which would require a southward-plunging oblique impact because the deposits are localized at the southern rim of Oudemans crater. Problems with this interpretation are that it does not explain why the northern rim of the unnamed crater is missing and why the eroded crater rim segment of the unnamed crater was overlain precisely in space by the surficial deposits. Here, we suggest that the missing northern rim of the unnamed crater was eroded by the same southward-flowing glaciation across the Oudemans crater basin and its bounding plateau plains. The surficial deposits mapped by Witbeck et al. (1991) represent glacially excavated materials from Oudemans crater, which were transported into the unnamed crater. The northern rim of the unnamed crater was erased during glacial transport and deposition. The same southward-flowing glaciation across the Oudemans crater basin may have also removed the central uplift of the unnamed crater.

The above discussion shows that the southern wall of Oudemans crater should have experienced the southward-flowing glaciation documented in this study. However, the complete destruction of the northern wall and the intact southern wall requires an explanation. Below, we discuss four possible factors that may have contributed to the current morphology of the Oudemans crater basin. First, the southern crater wall lies farther away from the fault-controlled Valles Marineris troughs (e.g., Carr, 1974; Wise et al., 1979; Yin, 2012a), where trough-forming tectonic deformation may have created a more fractured and weaker northern wall and a less fractured and stronger southern wall. The same effect could also have been generated by a northward-plunging impact as suggested by Mest et al. (2011) and Osinski et al. (2011), which would imply that the oblique Oudemans impact also contributed partially to the removal of the northern crater wall as a rock-weakening rather than rock-removal process. Second, the presence of the central uplift may have acted as a topographic barrier, causing the southward glacial flow to slow down before climbing up the southern wall of Oudemans crater. The reduced glacial flow speed in turn would have decreased the rate of glacial erosion (see chapter 7 of Cuffey and Paterson, 2010 for the related physics). Third, according to our proposed erosional mechanism illustrated in Fig. 8G for the removal of the original crustal section separating the Triple Intersection Basin and the Oudemans crater basin, glacially induced rock removal should be

focused on the lee side. That is, a topographic barrier can be completely removed only when the backward cutting lee side has migrated across the entire width of the barrier. Fourth, the ice sheet flowing over Oudemans crater could have been polythermal. That is, the basal thermal state and mechanical condition of the ice sheet were not uniform at the northern and southern walls of Oudemans crater. This inference is observationally based and most favored, because our inferred southward-flowing glacier requires a southward-thinning ice sheet. Such a thickness distribution would be conducive to wet-based glaciation in the north and cold-based glaciation in the south (see chapter 7 in Cuffey and Paterson, 2010 for the related mechanics and physics). The lack of erosion associated with cold-based thin ice-sheet glaciation is well known on Earth (Atkins et al., 2002; Atkins and Dickinson, 2007; Atkins, 2013; Bierman et al., 2015), and has been inferred to have operated across the western flank of the Tharsis Montes (Head and Marchant, 2003; Kadish et al., 2008; Parsons et al., 2020).

Invoking wet-based glaciation for removing the northern wall of Oudemans crater has a broader implication for why the major troughs and basins at the western end of Valles Marineris share an interconnected floor network (Fig. 1). We envision that the troughs and basins were originally partitioned by crustal sections. Glacial filling and overspill following the process discussed above may have led to a unified floor linking troughs, basins, and Oudemans crater at the western end of Valles Marineris.

6.5. *Age of Tharsis glaciation and relationships to other regional glaciation events on Mars*

Differentiating competing models for the formation of the Late Hesperian circum-Tharsis outflow channels hinges critically on the timing of Tharsis glaciation and ice melting (Baker et al., 2000; Lucchitta, 2001; Harrison and Grimm, 2004; Carr and Head, 2019). We addressed this issue by conducting crater dating of the interpreted glacial landforms. Ideally, we may use a crater-size-frequency distribution to determine the absolute model age of each glacially generated landform assemblage (i.e., most of the second-order landforms mapped in this study), which would allow us to reconstruct the detailed history of landform evolution as shown in Fig. 8A. However, we found this approach impractical and potentially misleading. This is because the few largest craters (only 9 with D $\geq$ 900 m postdating the interpreted glaciation) are scattered across the Oudemans crater basin with an area of ~49,000 km^2, averaged about 1 such a crater in every 5000 km^2. As most of our mapped units are much smaller than 5000 km^2, performing crater counting on individual unit would have a high probability of missing these large craters, leading to apparent younger ages than the nearby terrains demonstrably formed during a coeval geologic process

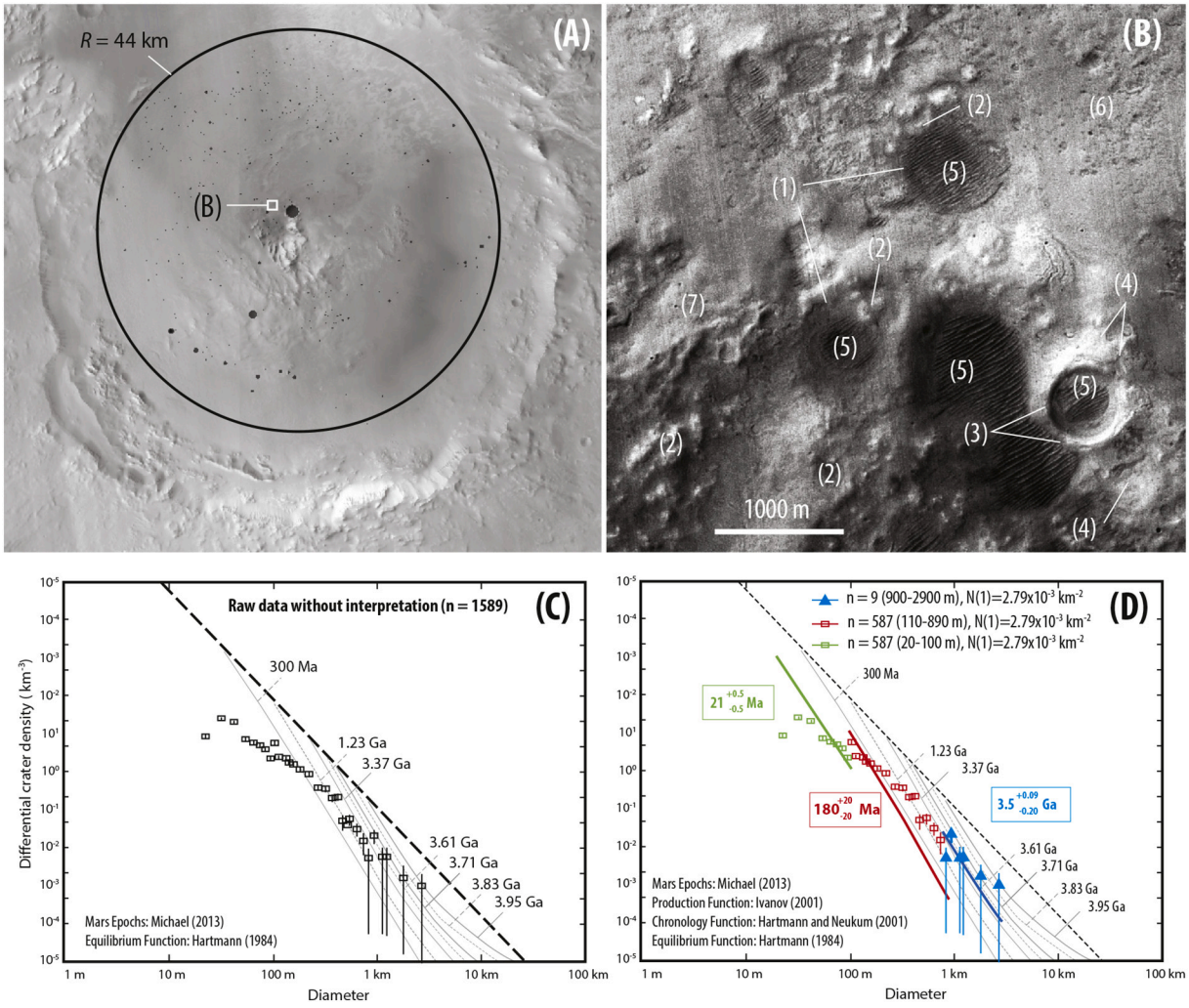

Fig. 21. (A) Aerial extent of the crater counting area and the craters counted in this study. (B) Examples of landform features and their relationships to impact craters considered in our crater counting. See text for detailed discussion. (C) Crater size-frequency distribution of the Oudemans crater floor. (D) Interpreted ages of geologic events on a crater size-frequency-distribution plot. The oldest event at $3.5^{+0.09}_{-0.20}$ Ga is interpreted as representing the timing of the inferred glaciation event in this study. Two younger events assigned at ~180 Ma and ~21 Ma provide the simplest interpretations to fit the rest of the data.

(see Warner et al., 2014 on this issue). The lack of a rigorous physical and statistical model defining the minimum size of a crater-counting area has led to many uncertainties in interpreting the geological significance of crater-counting-based model ages (Hartmann and Daubar, 2017; Hepburn et al., 2020).

In this study, we took the most conservative approach by performing crater counting across the entire Oudemans crater basin (Fig. 21A). To obtain an estimated age of glaciation, we only count craters that are superposed on top of our interpreted glaciated landforms. Pre-glaciation craters are not counted because they represent products of older geologic events. Pre-glaciation craters are characterized by the lack of raised crater rims, partial or complete burial of the crater basins by glacial-landform materials, and superposition of younger glacial landforms. We illustrate this practice below using geologic examples shown in Fig. 21B. *Feature 1* in Fig. 21B represents circular depressions without raised rims interpreted as pre-glaciation craters. Such craters are not counted. The rims of the pre-glaciation craters are overlain by a hummocky terrain (*feature 2* in Fig. 21B) interpreted to have a glacial origin. Craters on top of the hummocky terrain postdate glaciation and are counted. A circular depression with a raised rim (*feature 3*) and related impact deposits (*feature 4*) overlie glacial landforms; this crater postdating glaciation is counted. Dark-toned linear ridges in Fig. 21B inside circular depressions are interpreted as aeolian bedforms (*feature 5*), which overlie glaciated landforms and postdate glaciation. Craters on top of such terrains are counted. Also shown in Fig. 21B are scattered pits (*feature 6*) interpreted to have a glacial origin, and craters on top of the pitted terrain postdating glaciation are counted. Tongue-shaped ridges (*feature 7* in Fig. 21B) are interpreted as viscous-flow features related to glaciation, and craters on top of such ridges postdating glaciation are counted.

Using the examples illustrated above, we counted a total of 1589 craters with diameters from 20 m to 2850 m, which we interpret to have been superposed on the surface of the interpreted glacier-induced landforms. Fig. 21C shows the resulting crater size-frequency distribution using the size-binning convention of Michael and Neukum (2010). The data show a progressive shallowing trend towards smaller crater sizes (i.e., to the left of the plot), which implies resurfacing after the initial formation of the interpreted glacial landforms on which the crater counting was conducted (Michael and Neukum, 2010). Because the largest craters have the best chance of surviving post-glaciation resurfacing, we fit an isochron to craters with $D \geq 900$ m to estimate the oldest possible age with the smallest uncertainty. This yielded an absolute *crater model age* of $3.5^{+0.09}_{-0.20}$ Ga with a sample size $n = 9$ (Fig. 21D). Increasing the sample size by including smaller craters would make the estimated age younger and the uncertainty larger. This is because the population of small craters is under sampled as a result of resurfacing and counting errors (e.g., Platz et al., 2013; Robbins et al., 2014; Williams et al., 2018), and the slope of the smaller-crater data crosses rather follows isochrons as discrete clusters (Fig. 21C). Although nonunique, we find that the simplest interpretation of the smaller craters with $D<900$ m places the resurfacing events at $\sim 180 \pm 20$ Ma and $\sim 20 \pm 0.5$ Ma, respectively.

We note that our inferred Late Hesperian glaciation event is similar to the estimated Late Hesperian glacier-induced landform development along the ~2000 km Valles Marineris trough zone (Fueten et al., 2011; Mège and Bourgeois, 2011; Gourronc et al., 2014; Dębniak et al., 2017; cf. Kissick and Carbonneau, 2019). There, the lower age bound of the inferred glaciation event is constrained to the Late Noachian and Early Hesperian bedrock (Tanaka et al., 2014) on which the glacial landforms were superposed (Fueten et al., 2011; Mège and Bourgeois, 2011; Gourronc et al., 2014; Dębniak et al., 2017). The upper age bound is provided by post-glaciation landslides, which occur throughout Valles Marineris (Brunetti et al., 2014; Watkins et al., 2015; Watkins et al., 2020) and overlie the interpreted glacier-generated landforms (Gourronc et al., 2014). The age of these landslides were dated to have started at ~3.5 Ga (Quantin et al., 2004). Because the trough and basin floors of westernmost Valles Marineris and Oudemans crater share a similar elevation range of 2-3 km, display similar glacier-induced landforms (cf. landforms mapped by Dębniak et al., 2017), and have a similar age of glacial-landform formation, we suggest that the two regions were affected by the same regional glaciation event in the Late Hesperian.

The Late Hesperian glaciation in Valles Marineris and our study area in the central Tharsis rise predates by more than 2 Ga the Late Amazonian mountain glaciation event restricted to the western flanks of the Tharsis Montes and Olympus Mons in the western Tharsis rise (Lucchitta, 1981; Head and Marchant, 2003; Milkovich et al., 2006; Shean et al., 2005; Kadish et al., 2008; Rossi et al., 2011; Head and Weiss, 2014; Scanlon et al., 2014, 2015a, 2015b; Parsons et al., 2020). This younger glaciation event was attributed to an obliquity event and the rain shadow effect of the Tharsis Montes, which blocked moistures transported by the westerlies (Forget et al., 2006).

An interesting question raised by our study is whether the western Tharsis plateau-trough glaciation had extended to the southern highlands of Mars. Whether the southern highlands have ever experienced a regional glaciation event remains a subject of intense debate. It has been proposed that the region was covered by an ice sheet at or before the Late Noachian (~3.8 Ga) (Forget et al., 2013; Wordsworth et al., 2013; Head and Marchant, 2014; Cassanelli et al., 2015; Fastook and Head, 2015; Wordsworth, 2016). In contrast, a warm-wet Mars climate in the Late Noachian was also proposed (see review by Ramirez and Craddock, 2018), which may explain the widely occurring gully networks that formed before the end of the Noachian (Fassett and Head III, 2008) in the southern highlands. We note that the Late Noachian gully networks were recently reinterpreted as subglacial not surface stream channels (Galofre et al., 2020). Even if glaciation did occur in the southern highlands, its inferred age at or prior to ~3.8 Ga (see Wordsworth, 2016 for a review) appears to be >300 Ma older than the glaciation event dated in our study area *when all dating uncertainties are neglected*. Although regional glaciation may not seem to be coeval, local mountain glaciation dated at ~3.6 Ga in the southern highlands (Bouquety et al., 2019) is similar to our inferred regional glaciation age, which points to the important role of high topography in intercepting moistures leading to mountain and plateau glaciation in the Late Hesperian.

The above discussion suggests that *regional* glaciation on Mars may have been punctuated, with each event occurring at different locations. This style of glaciation appears to have been expressed by ice sheets on relatively flat highlands in the early history of Mars (i.e., the southern highlands of Mars and the Tharsis plateau), followed by younger mountain glaciation (i.e., Tharsis Montes and Olympus Mons in the Tharsis rise and mountain glaciation in the southern highlands). Among the three proposed regional glaciation events (i.e., Noachian icy southern highlands, Late Hesperian Tharsis ice cap, and Late Amazonian mountain glaciers), only the Late Hesperian Tharsis glaciation event was coeval with the outflow-channel development (Carr and Head III, 2010; Cassanelli and Head, 2019). Although this temporal correlation supports the Tharsis ice-cap hypothesis, it also requires a rapid ice-melting mechanism. The sudden melting of the Tharsis ice cap could have been triggered by an obliquity event (Ward, 1973; Laskar et al., 2004), a large impact event that caused a sudden warming of the Mars climate (Segura et al., 2002, 2008, 2012), greenhouse-gas effects induced by an intense episode of volcanism (Jakosky and Phillips, 2001; Halevy and Head III, 2014), polar-ice evolution (Urata and Toon, 2013), and a phase of methane bursts (Wordsworth et al., 2017; Kite et al., 2017). It could also have been caused by heating on top of an ice sheet such as supraglacial melting (e.g., Palumbo et al., 2018) and supraglacial lava emplacement (Cassanelli and Head, 2019), or by geothermal heating from below an ice sheet (Carr and Head III, 2003; Ojha et al., 2020). Our current knowledge is unable to differentiate these competing mechanisms.

7. Conclusions

Geomorphologic mapping based on high-resolution satellite images (0.25-6.0 m/pixel) across Oudemans crater and its bounding plateau plains in the central Tharsis rise shows that the first-order morphologic units and landform assemblages are dominantly Oudemans-impact-induced. The impact-induced morphology was superposed by a suite of younger landform assemblages that we interpret to consist of horn-like peaks, arête-like ridges, cirque-like depressions, U-shaped trunk and hanging valleys, trim-line-like escarpments, lobate ridges composed of unconsolidated boulders, steep-walled and mutually terminating channels, pitted, striated and hummocky terrains, and features resembling drumlins, crag-and-tails and roches moutonnées. A striated terrain on the plateau plains consists of streamlined linear ridges that are 400-2000 m wide and up to 17 km long. These ridges are superposed by coevally developed shorter transverse ridges. Together, two ridge sets exhibit a washboard pattern. The length-to-width ratio, shape, and washboard pattern of the linear ridges in the striated terrain are comparable to mega-scale glacial lineations (MSGLs) documented on Earth. MSGLs on Earth are the product of ice-stream flow in regional ice sheets. Using well-understood Earth analogues as a guide, specifically the MSGL terrains on Earth and Hiawatha crater under the Greenland ice sheet, we suggest that the younger post-Oudemans-impact landform assemblages were created by multiple flow phases of a regional ice sheet across the Tharsis plateau plains and their bounding crater basins and troughs. The inferred ice sheet was unconstrained by topography, expressed by uphill flows similar to those in Greenland and Antarctica on Earth. The shape of the inferred glacial landforms and their cross-cutting relationships require early northward-flowing northward-advancing glaciation that filled up Oudemans crater and its nearby troughs in Valles Marineris and Noctis Labyrinthus. The total volume of the glacier ice stored in Oudemans crater alone is estimated on the order of ~200,000 km^3. The northward-flowing ice-sheet-style glaciation was followed by southward-flowing and northward-retreating ice-sheet style glaciation across the region. Finally, local northward-flowing mountain glaciation occurred across the central uplift of Oudemans crater. The size-frequency distribution of the craters superposed on top of the interpreted glaciated landforms yields an estimated glaciation age of ~3.5 Ga. This age is coeval with the age of the previously interpreted glacier-induced landforms along the ~2000-km Valles Marineris trough zone, which supports the presence of a regional ice sheet and along-trough-flowing glaciers as predicted by the Tharsis ice-cap hypothesis. Our estimated glaciation age is also coeval with the development of the circum-Tharsis outflow channels, which is consistent with a scenario that the Tharsis ice-sheet melting was the source of surface running water for creating the giant (>1000s km in length) outflow channels. In light of the earlier documented glaciation events on Mars, it appears that regional-scale glacier systems formed episodically throughout the Mars history, and each event occurred at a different location with a different style of glaciation. Specifically, the regional glaciation appears to have evolved from topographically unconstrained ice-sheet flow (i.e., the Late Noachian icy southern highlands and Late Hesperian Tharsis ice cap) to topographically constrained mountain-glacier flow (i.e., Tharsis Montes and Olympus Mons and high-altitude regions of the southern highlands). This spatiotemporal pattern provides a new basis for future numerical modeling of the Mars climate evolution.

Declaration of Competing Interest

None.

Acknowledgements

We thank NASA for making the CTX and HiRISE images available and the HiRISE Team at the University of Arizona for creating DEMs used in this study. We also thank T. Kneissl and G. Michael from the Freie Universität Berlin for making available their *craterstats2* used in this study. Feedback on the original manuscript was provided by two anonymous journal reviewers; we are very grateful for their thoughtful and detailed comments. The work presented in this paper is a result of curiosity-driven research and was not supported by any funding agencies.

References

Alden, W.C., 1914. Glaciers of Glacier National Park. US Government Printing Office, pp. 1–53.
Anderson, R.C., Dohm, J.M., Golombek, M.P., Haldemann, A.F., Franklin, B.J., Tanaka, K.L., Peer, B., 2001. Primary centers and secondary concentrations of tectonic activity through time in the western hemisphere of Mars. J. Geophys. Res. 106 (E9), 20563–20585.
Andrews-Hanna, J.C., Phillips, R.J., 2007. Hydrological modeling of outflow channels and chaos regions on Mars. J. Geophys. Res. 112 (E8).
Atkins, C.B., 2013. Geomorphological evidence of cold-based glacier activity in South Victoria Land, Antarctica. Geol. Soc. Lond., Spec. Publ. 381 (1), 299–318.
Atkins, C.B., Dickinson, W.W., 2007. Landscape modification by meltwater channels at margins of cold-based glaciers, Dry Valleys, Antarctica. Boreas 36 (1), 47–55.
Atkins, C.B., Barrett, P.J., Hicock, S.R., 2002. Cold glaciers erode and deposit: evidence from Allan Hills, Antarctica. Geology 30 (7), 659–662.
Baioni, D., 2018. Karst Landforms as Markers of Recent Climate Change on Mars: An Example From a Late Amazonian Epoch Evaporate-Karst Within a Trough in Western Noctis Labyrinthus. In: Dynamic Mars. Elsevier, pp. 411–429.
Baioni, D., Tramontana, M., 2017. Possible evaporite karst in an interior layered deposit in Juventae Chasma, Mars. Int. J. Speleol. 46 (2), 5.
Baker, V.R., 2001. Water and the Martian landscape. Nature 412 (6843), 228–236.
Baker, V.R., Strom, R.G., Gulick, V.C., Kargel, J.S., Komatsu, G., Kale, V.S., 1991. Ancient oceans, ice sheets and the hydrological cycle on Mars. Nature 352 (6336), 589–594.
Baker, V.R., Strom, R.G., Dohm, J.M., Gulick, V.C., Kargel, J.S., Komatsu, G., Ori, G.G., Rice Jr., J.W., 2000. Mars' Oceanus Borealis, ancient glaciers, and the MEGAOUTFLO hypothesis. Lunar Planet. Sci XXXI, 1863.
Baker, V.R., Maruyama, S., Dohm, J.M., 2007. Tharsis superplume and the geological evolution of early Mars. In: Superplumes: Beyond plate tectonics (pp. 507-522). Springer, Dordrecht.
Barcheck, C.G., Schwartz, S.Y., Tulaczyk, S., 2020. Icequake streaks linked to potential mega-scale glacial lineations beneath an Antarctic ice stream. Geology 48 (2), 99–102.
Bendle, J.M., Thorndycraft, V.R., Palmer, A.P., 2017. The glacial geomorphology of the Lago Buenos Aires and Lago Pueyrredón ice lobes of central Patagonia. J. Maps 13 (2), 654–673.
Bierman, P.R., Davis, P.T., Corbett, L.B., Lifton, N.A., Finkel, R.C., 2015. Cold-based Laurentide ice covered New England's highest summits during the Last Glacial Maximum. Geology 43 (12), 1059–1062.
Blair, T.C., 1999. Sedimentology of the debris-flow-dominated Warm Spring Canyon alluvial fan, Death Valley, California. Sedimentology 46 (5), 941–965.
Blasius, K.R., Cutts, J.A., Guest, J.E., Masursky, H., 1977. Geology of the Valles Marineris: First analysis of imaging from the Viking 1 Orbiter primary mission. Journal of Geophysical Research 82 (28), 4067–4091.
Bouley, S., Baratoux, D., Matsuyama, I., Forget, F., Séjourné, A., Turbet, M., Costard, F., 2016. Late Tharsis formation and implications for early Mars. Nature 531 (7594), 344–347.
Bouley, S., Baratoux, D., Paulien, N., Missenard, Y., Saint-Bézar, B., 2018. The revised tectonic history of Tharsis. Earth Planet. Sci. Lett. 488, 126–133.
Boulton, G.S., Dongelmans, P., Punkari, M., Broadgate, M., 2001. Palaeoglaciology of an ice sheet through a glacial cycle: the European ice sheet through the Weichselian. Quat. Sci. Rev. 20 (4), 591–625.
Bouquety, A., Sejourné, A., Costard, F., Mercier, D., Bouley, S., 2019. Morphometric evidence of 3.6 Ga glacial valleys and glacial cirques in martian highlands: South of Terra Sabaea. Geomorphology 334, 91–111.
Bridges, N.T., 2006. Studies of Martian sedimentological history through in situ study of Gale and Oudemans craters: Two landing site proposals for the Mars Science Laboratory. In: Abstract for Program for the First MSL Landing Site Workshop, Pasadena, California.
Brodzikowski, K., Van Loon, A.J., 1987. A systematic classification of glacial and periglacial environments, facies and deposits. Earth Sci. Rev. 24 (5), 297–381.
Brož, P., Kryza, O., Wilson, L., Conway, S.J., Hauber, E., Mazzini, A., Patel, M.R., 2020. Experimental evidence for lava-like mud flows under Martian surface conditions. Nat. Geosci. 1–5.
Brunetti, M.T., Guzzetti, F., Cardinali, M., Fiorucci, F., Santangelo, M., Mancinelli, P., Borselli, L., 2014. Analysis of a new geomorphological inventory of landslides in Valles Marineris, Mars. Earth Planet. Sci. Lett. 405, 156–168.
Bull, W.B., 1991. Geomorphic responses to climatic change.
Burgess, W.P., Yin, A., Dubey, C.S., Shen, Z.K., Kelty, T.K., 2012. Holocene shortening across the Main Frontal Thrust zone in the eastern Himalaya. Earth Planet. Sci. Lett. 357, 152–167.
Butcher, F.E., Conway, S.J., Arnold, N.S., 2016. Are the Dorsa Argentea on Mars eskers? Icarus 275, 65–84.
Butcher, F.E., Balme, M.R., Gallagher, C., Arnold, N.S., Conway, S.J., Hagermann, A., Lewis, S.R., 2017. Recent basal melting of a mid-latitude glacier on Mars. J. Geophys. Res. 122 (12), 2445–2468.

Carling, P.A., Burr, D.M., Johnsen, T.F., Brennand, T.A., 2009. 3 A review of open-channel megaflood depositional landforms on Earth and Mars. Megaflooding on Earth Mars 33.
Carr, M.H., 1974. Tectonism and volcanism of the Tharsis region of Mars. J. Geophys. Res. 79 (26), 3943–3949.
Carr, M.H., 1979. Formation of Martian flood features by release of water from confined aquifers. J. Geophys. Res. Solid Earth 84 (B6), 2995–3007.
Carr, M.H., Head, J.W., 2015. Martian surface/near-surface water inventory: Sources, sinks, and changes with time. Geophys. Res. Lett. 42 (3), 726–732.
Carr, M., Head, J., 2019. Mars: Formation and fate of a frozen Hesperian ocean. Icarus 319, 433–443.
Carr, M.H., Head III, J.W., 2003. Basal melting of snow on early Mars: A possible origin of some valley networks. Geophys. Res. Lett. 30 (24).
Carr, M.H., Head III, J.W., 2010. Geologic history of Mars. Earth Planet. Sci. Lett. 294 (3–4), 185–203.
Cassanelli, J.P., Head, J.W., 2019. Glaciovolcanism in the Tharsis volcanic province of Mars: Implications for regional geology and hydrology. Planet. Space Sci. 169, 45–69.
Cassanelli, J.P., Head, J.W., Fastook, J.L., 2015. Sources of water for the outflow channels on Mars: Implications of the Late Noachian "icy highlands" model for melting and groundwater recharge on the Tharsis rise. Planet.Space Sci. 108, 54–65.
Caudill, C.M., Tornabene, L.L., McEwen, A.S., Byrne, S., Ojha, L., Mattson, S., 2012. Layered Mega Blocks in the central uplifts of impact craters. Icarus 221 (2), 710–720.
Caudill, C., Tornabene, L., McEwen, A., Wray, J., 2011, March. Crater-exposed intact stratigraphy blocks and volcanogenic origin. In: Lunar and Planetary Science Conference (No. 1608, p. 2393.
Chandler, B.M., Evans, D.J., Roberts, D.H., 2016. Characteristics of recessional moraines at a temperate glacier in SE Iceland: Insights into patterns, rates and drivers of glacier retreat. Quat. Sci. Rev. 135, 171–205.
Chapman, M.G., Soderblom, L.A., Cushing, G., 2005. Evidence of very young glacial processes in central Candor Chasma. Mars. LPI 1850.
Christensen, P.R., Engle, E., Anwar, S., Dickenshied, S., Noss, D., Gorelick, N., Weiss-Malik, M., 2009. JMARS-a planetary GIS. In: AGU Fall Meeting Abstract #IN22A-06.
Chudley, T.R., Christoffersen, P., Doyle, S.H., Bougamont, M., Schoonman, C.M., Hubbard, B., James, M.R., 2019. Supraglacial lake drainage at a fast-flowing Greenlandic outlet glacier. Proceedings of the National Academy of Sciences 116 (51), 25468–25477.
Cintala, M.J., Grieve, R.A.F., 1998. Scaling impact melting and crater dimensions: Implications for the lunar cratering record. Meteorit. Planet. Sci. 33, 889–912.
Clark, C.D., 1993. Mega-scale glacial lineations and cross-cutting ice-flow landforms. Earth Surf. Process. Landf. 18 (1), 1–29.
Clark, C.D., Stokes, C.R., 2003. Palaeo-ice stream landsystem. In: Evans, D.J.A. (Ed.), Glacial Landsystems. Arnold, London, pp. 204–227.
Clark, C.D., Tulaczyk, S.M., Stokes, C.R., Canals, M., 2003. A groove-ploughing theory for the production of mega-scale glacial lineations, and implications for ice-stream mechanics. J. Glaciol. 49 (165), 240–256.
Clark, C.D., Ely, J.C., Spagnolo, M., Hahn, U., Hughes, A.L., Stokes, C.R., 2018. Spatial organization of drumlins. Earth Surf. Process. Landf. 43 (2), 499–513.
Clarke, G.K., 2005. Subglacial processes. Annu. Rev. Earth Planet. Sci. 33, 247–276.
Cline, M.D., Iverson, N.R., Harding, C., 2015. Origin of washboard moraines of the Des Moines Lobe: Spatial analyses with LiDAR data. Geomorphology 246, 570–578.
Cuffey, K.M., Paterson, W.S.B., 2010. The physics of glaciers. Academic Press.
Dębniak, K., Mège, D., Gurgurewicz, J., 2017. Geomorphology of Ius Chasma, Valles Marineris, Mars. J. Maps 13 (2), 260–269.
Dickson, J.L., Head, J.W., Goudge, T.A., Barbieri, L., 2015. Recent climate cycles on Mars: Stratigraphic relationships between multiple generations of gullies and the latitude dependent mantle. Icarus 252, 83–94.
Dickson, J.L., Kerber, L.A., Fassett, C.I., Ehlmann, B.L., 2018. A global, blended CTX mosaic of Mars with vectorized seam mapping: a new mosaicking pipeline using principles of non-destructive image editing. In: Lunar and Planetary Science Conference, Vol. 49, pp. 1–2.
Ding, Z., Zhao, J., Wang, J., Lai, Z., 2020. Yardang on Earth and its implications to Mars: A review. Geomorphology 364, 1–55, 107230.
Dohm, J.M., Tanaka, K.L., Hare, T.M., 2001. Geologic map of the Thaumasia region of Mars. ASSEMBLAGE 2 (5), 16.
Dohm, J.M., Baker, V.R., Maruyama, S., Anderson, R.C., 2007. Traits and evolution of the Tharsis superplume, Mars. In: In Superplumes: Beyond plate tectonics. Springer, Dordrecht, pp. 523–536.
Dohm, J.M., Maruyama, S., Kido, M., Baker, V.R., 2018. A possible anorthositic continent of early Mars and the role of planetary size for the inception of Earth-like life. Geosci. Front. 9 (4), 1085–1098.
Dong, Z., Lv, P., Lu, J., Qian, G., Zhang, Z., Luo, W., 2012. Geomorphology and origin of yardangs in the Kumtagh Desert, Northwest China. Geomorphology 139, 145–154.
Dowdeswell, E.K., Todd, B.J., Dowdeswell, J.A., 2016. Crag-and-tail features: convergent ice flow through Eclipse Sound, Baffin Island, Arctic Canada. Geol. Soc. Lond. Mem. 46 (1), 55–56.
Dowdeswell, J.A., Batchelor, C.L., Montelli, A., Ottesen, D., Christie, F.D.W., Dowdeswell, E.K., Evans, J., 2020. Delicate seafloor landforms reveal past Antarctic grounding-line retreat of kilometers per year. Science 368 (6494), 1020–1024.
Edwards, C.S., Nowicki, K.J., Christensen, P.R., Hill, J., Gorelick, N., Murray, K., 2011. Mosaicking of global planetary image datasets: 1. Techniques and data processing for Thermal Emission Imaging System (THEMIS) multi-spectral data. J. Geophys. Res. 116. E10008.
Engelhardt, H., Kamb, B., 1997. Basal hydraulic system of a West Antarctic ice stream: constraints from borehole observations. J. Glaciol. 43 (144), 207–230.
Evans, D.J.A., 2003. Glacial Landsystems. Hodder Arnold, London, p. 532.
Evans, D.J.A., Phillips, E.R., Hiemstra, J.F., Auton, C.A., 2006. Subglacial till: formation, sedimentary characteristics and classification. Earth Sci. Rev. 78 (1–2), 115–176.
Eyles, N., Boyce, J.I., Barendregt, R.W., 1999. Hummocky moraine: sedimentary record of stagnant Laurentide Ice Sheet lobes resting on soft beds. Sediment. Geol. 123 (3–4), 163–174.
Fassett, C.I., Head III, J.W., 2008. Valley network-fed, open-basin lakes on Mars: Distribution and implications for Noachian surface and subsurface hydrology. Icarus 198 (1), 37–56.
Fastook, J.L., Head, J.W., 2015. Glaciation in the Late Noachian Icy Highlands: Ice accumulation, distribution, flow rates, basal melting, and top-down melting rates and patterns. Planet. Space Sci. 106, 82–98.
Fergason, R.L., Hare, T.M., Laura, J., 2018. HRSC and MOLA Blended Digital Elevation Model at 200m v2, Astrogeology PDS Annex. US Geological Survey.
Forget, F., Haberle, R.M., Montmessin, F., Levrard, B., Head, J.W., 2006. Formation of glaciers on Mars by atmospheric precipitation at high obliquity. Science 311 (5759), 368–371.
Forget, F., Wordsworth, R., Millour, E., Madeleine, J.B., Kerber, L., Leconte, J., Haberle, R.M., 2013. 3D modelling of the early martian climate under a denser CO2 atmosphere: Temperatures and CO2 ice clouds. Icarus 222 (1), 81–99.
Fowler, A.C., Chapwanya, M., 2014. An instability theory for the formation of ribbed moraine, drumlins and mega-scale glacial lineations. Proc. Royal Soc. 470, 2171, 20140185.
Fueten, F., Flahaut, J., Le Deit, L., Stesky, R., Hauber, E., Gwinner, K., 2011. Interior layered deposits within a perched basin, southern Coprates Chasma, Mars: Evidence for their formation, alteration, and erosion. J. Geophys. Res. 116 (E2).
Gallagher, C., Balme, M., 2015. Eskers in a complete, wet-based glacial system in the Phlegra Montes region, Mars. Earth Planet. Sci. Lett. 431, 96–109.
Galofre, A.G., Jellinek, A.M., Osinski, G.R., 2020. Valley formation on early Mars by subglacial and fluvial erosion. Nat. Geosci. 1–6.
Gerke, H.H., Koszinski, S., Kalettka, T., Sommer, M., 2010. Structures and hydrologic function of soil landscapes with kettle holes using an integrated hydropedological approach. J. Hydrol. 393 (1–2), 123–132.
Golabek, G.J., Keller, T., Gerya, T.V., Zhu, G., Tackley, P.J., Connolly, J.A., 2011. Origin of the Martian dichotomy and Tharsis from a giant impact causing massive magmatism. Icarus 215 (1), 346–357.
Golombek, M.P., Phillips, R.J., Watters, T.R., Schultz, R.A., 2010. Mars tectonics. Planetary Tectonics 11, 183–232.
Gourronc, M., Bourgeois, O., Mège, D., Pochat, S., Bultel, B., Massé, M., Le Deit, L., Le Mouélic, S., Mercier, D., 2014. One million cubic kilometers of fossil ice in Valles Marineris: Relicts of a 3.5 Gy old glacial landsystem along the Martian equator. Geomorphology 204, 235–255.
Grieve, R.A., Pilkington, M., 1996. The signature of terrestrial impacts. AGSO J. Austr. Geol. Geophys. 16, 399–420.
Grima, C., Kofman, W., Mouginot, J., Phillips, R.J., Hérique, A., Biccari, D., Cutigni, M., 2009. North polar deposits of Mars: Extreme purity of the water ice. Geophys. Res. Lett. 36 (3).
Halevy, I., Head III, J.W., 2014. Episodic warming of early Mars by punctuated volcanism. Nat. Geosci. 7 (12), 865–868.
Hall, A.M., Krabbendam, M., van Boeckel, M., Goodfellow, B.W., Hättestrand, C., Heyman, J., Näslund, J.O., 2020. Glacial ripping: geomorphological evidence from Sweden for a new process of glacial erosion. Series A, Physical Geography, Geografiska Annaler, pp. 1–21.
Hambrey, M.J., Huddart, D., Bennett, M.R., Glasser, N.F., 1997. Genesis of 'hummocky moraines' by thrusting in glacier ice: evidence from Svalbard and Britain. J. Geol. Soc. 154 (4), 623–632.
Harder, H., Christensen, U.R., 1996. A one-plume model of Martian mantle convection. Nature 380 (6574), 507–509.
Fergason, R.L, Hare, T.M., Laura, J., 2018, HRSC and MOLA Blended Digital Elevation Model at 200 m v2, Astrogeology PDS Annex, U.S. Geological Survey, URL: http://bit.ly/HRSC_MOLA_Blend_v0.
Harrison, K.P., Grimm, R.E., 2004. Tharsis recharge: A source of groundwater for Martian outflow channels. Geophys. Res. Lett. 31 (14).
Hartmann, W.K., Daubar, I.J., 2017. Martian cratering 11. Utilizing decameter scale crater populations to study Martian history. Meteorit. Planet. Sci. 52 (3), 493–510.
Hättestrand, C., Kleman, J., 1999. Ribbed moraine formation. Quat. Sci. Rev. 18 (1), 43–61.
Hauber, E., Brož, P., Jagert, F., Jodłowski, P., Platz, T., 2011. Very recent and wide-spread basaltic volcanism on Mars. Geophys. Res. Lett. 38 (10).
Head, J.W., Marchant, D.R., 2003. Cold-based mountain glaciers on Mars: western Arsia Mons. Geology 31 (7), 641–644.
Head, J.W., Marchant, D.R., 2014. The climate history of early Mars: insights from the Antarctic McMurdo Dry Valleys hydrologic system. Antarct. Sci. 26 (6), 774–800.
Head, J.W., Weiss, D.K., 2014. Preservation of ancient ice at Pavonis and Arsia Mons: tropical mountain glacier deposits on Mars. Planetary Space Sci. 103, 331–338.
Head, J.W., Marchant, D.R., Dickson, J.L., Kress, A.M., Baker, D.M., 2010. Northern mid-latitude glaciation in the Late Amazonian period of Mars: Criteria for the recognition of debris-covered glacier and valley glacier landsystem deposits. Earth Planet. Sci. Lett. 294 (3–4), 306–320.
Hepburn, A.J., Ng, F., Livingstone, S.J., Holt, T., Hubbard, B., 2020. Poly-phase mid-latitude glaciation on Mars: Chronology of the formation of superposed glacier-like forms from crater-count dating. J. Geophys. Res. 125 e2019JE006102.
Hindmarsh, R.C., 1998. Drumlinization and drumlin-forming instabilities: viscous till mechanisms. J. Glaciol. 44 (147), 293–314.
Inbar, M., Risso, C., 2001. Holocene yardangs in volcanic terrains in the southern Andes, Argentina. Earth Surface Process. Landforms 26 (6), 657–666.

Iverson, N.R., 2012. A theory of glacial quarrying for landscape evolution models. Geology 40 (8), 679–682.
Jakosky, B.M., Phillips, R.J., 2001. Mars' volatile and climate history. Nature 412 (6843), 237–244.
Jansson, K.N., Kleman, J., 1999. The horned crag-and-tails of the Ungava Bay landform swarm, Quebec–Labrador, Canada. Ann. Glaciol. 28, 168–174.
Johnson, M.D., Schomacker, A., Benediktsson, Í.Ö., Geiger, A.J., Ferguson, A., Ingólfsson, Ó., 2010. Active drumlin field revealed at the margin of Múlajökull, Iceland: a surge-type glacier. Geology 38 (10), 943–946.
Kadish, S.J., Head, J.W., Parsons, R.L., Marchant, D.R., 2008. The Ascraeus Mons fan-shaped deposit: Volcano–ice interactions and the climatic implications of cold-based tropical mountain glaciation. Icarus 197 (1), 84–109.
Kadish, S.J., Head, J.W., Fastook, J.L., Marchant, D.R., 2014. Middle to Late Amazonian tropical mountain glaciers on Mars: The ages of the Tharsis Montes fan-shaped deposits. Planet. Space Sci. 91, 52–59.
Kamb, B., 2001. Basal zone of the West Antarctic ice streams and its role in lubrication of their rapid motion. In: The West Antarctic ice sheet: behavior and environment, 77, pp. 157–199.
Kapp, P., Pelletier, J.D., Rohrmann, A., Heermance, R., Russell, J., Ding, L., 2011. Wind erosion in the Qaidam basin, central Asia: implications for tectonics, paleoclimate, and the source of the Loess Plateau. GSA Today 21 (4/5), 4–10.
Kasmai, B., 2014. Morphological and structural mapping of the Oudemans Impact Crater layered central uplift, Mars. MS Thesis. the University of Western Ontario, p. 82.
Kirk, R.L., Howington-Kraus, E., Rosiek, M.R., Anderson, J.A., Archinal, B.A., Becker, K. J., Holmberg, I.M., 2008. Ultrahigh resolution topographic mapping of Mars with MRO HiRISE stereo images: Meter-scale slopes of candidate Phoenix landing sites. J. Geophys. Res. 113 (E3).
Kissick, L.E., Carbonneau, P.E., 2019. The case against vast glaciation in Valles Marineris, Mars. Icarus 321, 803–823.
Kite, E.S., Gao, P., Goldblatt, C., Mischna, M.A., Mayer, D.P., Yung, Y.L., 2017. Methane bursts as a trigger for intermittent lake-forming climates on post-Noachian Mars. Nat. Geosci. 10 (10), 737–740.
Kjær, K.H., Larsen, N.K., Binder, T., Bjørk, A.A., Eisen, O., Fahnestock, M.A., Houmark-Nielsen, M., 2018. A large impact crater beneath Hiawatha Glacier in northwest Greenland. Sci. Adv. 4 (11), eaar8173.
Kohlstedt, D.L., Evans, B., Mackwell, S.J., 1995. Strength of the lithosphere: Constraints imposed by laboratory experiments. J. Geophys. Res. Solid Earth 100 (B9), 17587–17602.
Krabbendam, M., Eyles, N., Putkinen, N., Bradwell, T., Arbelaez-Moreno, L., 2016. Streamlined hard beds formed by palaeo-ice streams: A review. Sediment. Geol. 338, 24–50.
Laskar, J., Correia, A.C.M., Gastineau, M., Joutel, F., Levrard, B., Robutel, P., 2004. Long term evolution and chaotic diffusion of the insolation quantities of Mars. Icarus 170 (2), 343–364.
Lastras, G., Dowdeswell, J.A., 2016. Terminal and recessional moraines in the fjords of southern Chile. Geol. Soc. Lond. Mem. 46 (1), 65–66.
Lavé, J., Avouac, J.P., 2001. Fluvial incision and tectonic uplift across the Himalayas of central Nepal. J. Geophys. Res. Solid Earth 106 (B11), 26561–26591.
Le Heron, D.P., Sutcliffe, O.E., Whittington, R.J., Craig, J., 2005. The origins of glacially related soft-sediment deformation structures in Upper Ordovician glaciogenic rocks: implication for ice-sheet dynamics. Palaeogeogr. Palaeoclimatol. Palaeoecol. 218 (1–2), 75–103.
Leone, G., 2014. A network of lava tubes as the origin of Labyrinthus Noctis and Valles Marineris on Mars. J. Volcanol. Geotherm. Res. 277, 1–8. https://doi.org/10.1016/j.jvolgeores.2014.01.011.
Li, J., Dong, Z., Qian, G., Zhang, Z., Luo, W., Lu, J., Wang, M., 2016. Yardangs in the Qaidam Basin, northwestern China: Distribution and morphology. Aeolian Res. 20, 89–99.
Lillis, R.J., Dufek, J., Bleacher, J.E., Manga, M., 2009. Demagnetization of crust by magmatic intrusion near the Arsia Mons volcano: Magnetic and thermal implications for the development of the Tharsis province, Mars. J. Volcanol. Geothermal Res. 185, 123–138. https://doi.org/10.1016/j.jvolgeores.2008.12.007.
Livingstone, S.J., Clark, C.D., 2016. Morphological properties of tunnel valleys of the southern sector of the Laurentide Ice Sheet and implications for their formation. Earth Surface Dyn. 4, 567–589.
Loher, M., Pape, T., Marcon, Y., Römer, M., Wintersteller, P., Praeg, D., Bohrmann, G., 2018. Mud extrusion and ring-fault gas seepage–upward branching fluid discharge at a deep-sea mud volcano. Sci. Rep. 8 (1), 1–11.
Lucchitta, B.K., 1981. Mars and Earth: Comparison of cold-climate features. Icarus 45 (2), 264–303.
Lucchitta, B.K., 2001. Antarctic ice streams and outflow channels on Mars. Geophys. Res. Lett. 28 (3), 403–406.
Malin, M.C., Carr, M.H., 1999. Groundwater formation of Martian valleys. Nature 397 (6720), 589–591.
Malin, M.C., Bell, J.F., Cantor, B.A., Caplinger, M.A., Calvin, W.M., Clancy, R.T., Lee, S. W., 2007. Context camera investigation on board the Mars Reconnaissance Orbiter. J. Geophys. Res. 112 (E5).
Mangold, N., Loizeau, D., Poulet, F., Ansan, V., Baratoux, D., LeMouelic, S., Bardintzeff, J.M., Platevoet, B., Toplis, M., Pinet, P., Masson, P., 2010. Mineralogy of recent volcanic plains in the Tharsis region, Mars, and implications for platy-ridged flow composition. Earth Planet. Sci. Lett. 294 (3-4), 440–450.
Masson, P., 1980. Contribution to the structural interpretation of the Valles Marineris–Noctis Labyrinthus–Claritas Fossae regions of Mars. Earth Moon Planet. 22 (2), 211–219. https://doi.org/10.1007/BF00898432.
Mazzini, A., Svensen, H., Etiope, G., Onderdonk, N., Banks, D., 2011. Fluid origin, gas fluxes and plumbing system in the sediment-hosted Salton Sea Geothermal System (California, USA). J. Volcanol. Geotherm. Res. 205 (3-4), 67–83.
McEwen, A.S., Bierhaus, E.B., 2006. The importance of secondary cratering to age constraints on planetary surfaces. Annu. Rev. Earth Planet. Sci. 34, 535–567.
McEwen, A., et al., 1999. Voluminous volcanism on early Mars revealed in Valles Marineris. Nature 397, 584–586.
McEwen, A.S., et al., 2007. Mars Reconnaissance Orbiter's High Resolution Imaging Science Experiment (HiRISE). J. Geophys. Res 112. E05S02.
McEwen, A.S., et al., 2010. The high resolution imaging science experiment (HiRISE) during MRO's primary science phase (PSP). Icarus 205 (1), 2–37.
Mège, D., Bourgeois, O., 2011. Equatorial glaciations on Mars revealed by gravitational collapse of Valles Marineris wall slopes. Earth Planet. Sci. Lett. 310 (3-4), 182–191.
Mège, D., Masson, P., 1996a. A plume tectonics model for the Tharsis province, Mars. Planet. Space Sci. 44 (12), 1499–1546.
Mège, D., Masson, P., 1996b. Stress models for Tharsis formation, Mars. Planet. Space Sci. 44 (12), 1471–1497.
Mège, D., Cook, A.C., Garel, E., Lagabrielle, Y., Cormier, M., 2003. Volcanic rifting at martian grabens. J. Geophys. Res. 108, 5044. https://doi.org/10.1029/2002JE001852.
Melosh, H.J., 1989. Impact cratering: A geologic process. Research supported by NASA. Oxford University Press, New York. Oxford Monographs on Geology and Geophysics, No. 11), 1989, 253.
Mest, S.C., Weitz, C.M., Tornabene, L.L., 2011. Correlation of Low-Albedo Deposits on the Floors of Oudemans crater and Southeast Noctis Labyrinthus. In: In Lunar and Planetary Science Conference, 42, p. 2547.
Michael, G.G., 2013. Planetary surface dating from crater size–frequency distribution measurements: Multiple resurfacing episodes and differential isochron fitting. Icarus 226 (1), 885–890.
Michael, G.G., Neukum, G., 2010. Planetary surface dating from crater size–frequency distribution measurements: Partial resurfacing events and statistical age uncertainty. Earth Planet. Sci. Lett. 294 (3–4), 223–229.
Milkovich, S.M., Head, J.W., Marchant, D.R., 2006. Debris-covered piedmont glaciers along the northwest flank of the Olympus Mons scarp: Evidence for low-latitude ice accumulation during the Late Amazonian of Mars. Icarus 181 (2), 388–407.
Milliken, R.E., Mustard, J.F., Goldsby, D.L., 2003. Viscous flow features on the surface of Mars: Observations from high-resolution Mars Orbiter Camera (MOC) images. J. Geophys. Res. 108 (E6).
Möller, P., Dowling, T.P.F., 2018. Equifinality in glacial geomorphology: instability theory examined via ribbed moraine and drumlins in Sweden. GFF 140 (2), 106–135.
Moore, J.M., Howard, A.D., 2005. Large alluvial fans on Mars. J. Geophys. Res. 110 (E4).
Morris, E.C., Tanaka, K.L., 1994. Geologic maps of the Olympus Mons region of Mars. The US Geological Survey.
Mouginis-Mark, P.J., Wilson, L., 2019. Late-stage intrusive activity at Olympus Mons, Mars: Summit inflation and giant dike formation. Icarus 319, 459–469.
Neukum, G., Jaumann, R., Hoffmann, H., Hauber, E., Head, J.W., Basilevsky, A.T., Ivanov, B.A., Werner, S.C., Van Gasselt, S., Murray, J.B., McCord, T., 2004. Recent and episodic volcanic and glacial activity on Mars revealed by the High Resolution Stereo Camera. Nature 432 (7020), 971–979.
Nimmo, F., Tanaka, K., 2005. Early crustal evolution of Mars. Annu. Rev. Earth Planet. Sci. 33, 133–161.
Oehler, D.Z., Allen, C.C., 2010. Evidence for pervasive mud volcanism in Acidalia Planitia, Mars. Icarus 208 (2), 636–657.
Ojha, L., Mazarico, E., Goossens, S., 2020. Is There a Crustal Thickness Dichotomy on Mars? LPI 2326, 2386.
Okubo, C.H., 2016. Morphologic evidence of subsurface sediment mobilization and mud volcanism in Candor and Coprates Chasmata, Valles Marineris, Mars. Icarus 269, 23–37.
Onderdonk, N., Mazzini, A., Shafer, L., Svensen, H., 2011. Controls on the geomorphic expression and evolution of gryphons, pools, and caldera features at hydrothermal seeps in the Salton Sea Geothermal Field, southern California. Geomorphology 130 (3-4), 327–342.
Osinski, G.R., Tornabene, L.L., Grieve, R.A., 2011. Impact ejecta emplacement on terrestrial planets. Earth Planet. Sci. Lett. 310 (3–4), 167–181.
Palumbo, A.M., Head, J.W., Wordsworth, R.D., 2018. Late Noachian Icy Highlands climate model: Exploring the possibility of transient melting and fluvial/lacustrine activity through peak annual and seasonal temperatures. Icarus 300, 261–286.
Parsons, R.A., Kanzaki, T., Hemmi, R., Miyamoto, H., 2020. Cold-based glaciation of Pavonis Mons, Mars: evidence for moraine deposition during glacial advance. Prog. Earth Planet. Sci. 7 (1), 1–21.
Pelletier, Jon D., et al., 2018. Controls on yardang development and morphology: 1. Field observations and measurements at Ocotillo Wells, California. J. Geophys. Res. Earth Surf. 123 (4), 694–722.
Phillips, R.J., Zuber, M.T., Solomon, S.C., Golombek, M.P., Jakosky, B.M., Banerdt, W.B., Smoith, D.E., Hynek, B.M., Aharonson, O., Hauck II, S.A., 2001. Ancient geodynamics and global-scale hydrology on Mars. Science 291 (5513), 2587–2591.
Phillips, E., Cotterill, C., Johnson, K., Crombie, K., James, L., Carr, S., Ruiter, A., 2018. Large-scale glacitectonic deformation in response to active ice sheet retreat across Dogger Bank (southern central North Sea) during the Last Glacial Maximum. Quat. Sci. Rev. 179, 24–47.
Platz, T., Michael, G., Tanaka, K.L., Skinner Jr., J.A., Fortezzo, C.M., 2013. Crater-based dating of geological units on Mars: Methods and application for the new global geological map. Icarus 225 (1), 806–827.
Pullen, A., Kapp, P., Chen, N., 2018. Development of stratigraphically controlled, eolian-modified unconsolidated gravel surfaces and yardang fields in the wind-eroded Hami Basin, northwestern China. GSA Bull. 130 (3-4), 630–648.

Quantin, C., Allemand, P., Mangold, N., Delacourt, C., 2004. Ages of Valles Marineris (Mars) landslides and implications for canyon history. Icarus 172 (2), 555–572.
Quantin, C., Flahaut, J., Clenet, H., Allemand, P., Thomas, P., 2012. Composition and structures of the subsurface in the vicinity of Valles Marineris as revealed by central uplifts of impact craters. Icarus 221 (1), 436–452.
Ramirez, R.M., Craddock, R.A., 2018. The geological and climatological case for a warmer and wetter early Mars. Nat. Geosci. 11 (4), 230–237.
Ramsay, J.G., Huber, M.I., 1987. Modern Structural Geology (II): Folds and Fractures, pp. 309–700.
Reese, C.C., Solomatov, V.S., Baumgardner, J.R., Stegman, D.R., Vezolainen, A.V., 2004. Magmatic evolution of impact-induced Martian mantle plumes and the origin of Tharsis. J. Geophys. Res. 109 (E8).
Richardson, J.A., Wilson, J.A., Connor, C.B., Bleacher, J.E., Kiyosugi, K., 2017. Recurrence rate and magma effusion rate for the latest volcanism on Arsia Mons, Mars. Earth Planet. Sci. Lett. 458, 170–178.
Rijsdijk, K.F., Owen, G., Warren, W.P., McCarroll, D., van der Meer, J.J., 1999. Clastic dykes in over-consolidated tills: evidence for subglacial hydrofracturing at Killiney Bay, eastern Ireland. Sediment. Geol. 129 (1–2), 111–126.
Robbins, S.J., Hynek, B.M., 2011. Secondary crater fields from 24 large primary craters on Mars: Insights into nearby secondary crater production. J. Geophys. Res. 116 (E10).
Robbins, S.J., Antonenko, I., Kirchoff, M.R., Chapman, C.R., Fassett, C.I., Herrick, R.R., Singer, K., Zanetti, M., Lehan, C., Huang, D., Gay, P.L., 2014. The variability of crater identification among expert and community crater analysts. Icarus 234, 109–131.
Rodriguez, J.A.P., Zarroca, M., Linares, R., Gulick, V., Weitz, C.M., Yan, J., Fairén, A.G., Miyamoto, H., Platz, T., Baker, V., Kargel, J., 2016. Groundwater flow induced collapse and flooding in Noctis Labyrinthus, Mars. Planet. Space Sci. 124, 1–14.
Rossi, A.P., Komatsu, G., Kargel, S., Rossi, A.P., 2000. Rock glacier-like landforms in Valles Marineris, Mars. In: Lunar and Planetary Science Conference XXXI.
Rossi, A.P., Van Gasselt, S., Pondrelli, M., Dohm, J., Hauber, E., Dumke, A., Neukum, G., 2011. Evolution of periglacial landforms in the ancient mountain range of the Thaumasia Highlands, Mars. Geol. Soc. Lond., Spec. Publ. 356 (1), 69–85.
Scanlon, K.E., Head, J.W., Wilson, L., Marchant, D.R., 2014. Volcano–ice interactions in the Arsia Mons tropical mountain glacier deposits. Icarus 237, 315–339.
Scanlon, K.E., Head, J.W., Marchant, D.R., 2015a. Remnant buried ice in the equatorial regions of Mars: morphological indicators associated with the Arsia Mons tropical mountain glacier deposits. Planet. Space Sci. 111, 144–154.
Scanlon, K.E., Head, J.W., Marchant, D.R., 2015b. Volcanism-induced, local wet-based glacial conditions recorded in the Late Amazonian Arsia Mons tropical mountain glacier deposits. Icarus 250, 18–31.
Schultz, P.H., Anderson, R.R., 1996. Asymmetry of the Manson impact structure: Evidence for impact angle and direction. Geol. Soc. Am. Spec. Pap. 302, 397–417.
Segura, T.L., Toon, O.B., Colaprete, A., Zahnle, K., 2002. Environmental effects of large impacts on Mars. Science 298 (5600), 1977–1980.
Segura, T.L., Toon, O.B., Colaprete, A., 2008. Modeling the environmental effects of moderate-sized impacts on Mars. J. Geophys. Res. 113 (E11).
Schultz, P.H, D'Hondt, S, 1996. Cretaceous-Tertiary (Chicxulub) impact angle and its consequences. Geology 24 (11), 963–967.
Segura, T.L., McKay, C.P., Toon, O.B., 2012. An impact-induced, stable, runaway climate on Mars. Icarus 220 (1), 144–148.
Shanmugam, G., 2017. Global case studies of soft-sediment deformation structures (SSDS): Definitions, classifications, advances, origins, and problems. J. Palaeogeogr. 6 (4), 251–320.
Sharp, R.P., 1958. Malaspina Glacier, Alaska. Geol. Soc. Am. Bull. 69 (6), 617–646.
Shaw, J., Pugin, A., Young, R.R., 2008. A meltwater origin for Antarctic shelf bedforms with special attention to megalineations. Geomorphology 102 (3–4), 364–375.
Shean, D.E., Head, J.W., Marchant, D.R., 2005. Origin and evolution of a cold-based tropical mountain glacier on Mars: The Pavonis Mons fan-shaped deposit. J. Geophys. Res. 110 (E5).
Skinner Jr., J.A., Mazzini, A., 2009. Martian mud volcanism: Terrestrial analogs and implications for formational scenarios. Mar. Pet. Geol. 26 (9), 1866–1878.
Sleep, N.H., 1994. Martian plate tectonics. J. Geophys. Res. 99 (E3), 5639–5655.
Smellie, J.L., 2006. The relative importance of supraglacial versus subglacial meltwater escape in basaltic subglacial tuya eruptions: an important unresolved conundrum. Earth Sci. Rev. 74 (3–4), 241–268.
Smith, D.E., Zuber, M.T., Solomon, S.C., Phillips, R.J., Head, J.W., Garvin, J.B., Lemoine, F.G., 1999. The global topography of Mars and implications for surface evolution. Science 284 (5419), 1495–1503.
Solomon, S.C., Head, J.W., 1982. Evolution of the Tharsis province of Mars: The importance of heterogeneous lithospheric thickness and volcanic construction. J. Geophys. Res. Solid Earth 87 (B12), 9755–9774.
Solomon, S.C., Aharonson, O., Aurnou, J.M., Banerdt, W.B., Carr, M.H., Dombard, A.J., Frey, H.V., Golombek, M.P., Hauck, S.A., Head, J.W., Jakosky, B.M., 2005. New perspectives on ancient Mars. Science 307 (5713), 1214–1220.
Sookhan, S., Eyles, N., Arbelaez-Moreno, L., 2018. Converging ice streams: a new paradigm for reconstructions of the Laurentide Ice Sheet in southern Ontario and deposition of the Oak Ridges Moraine. Can. J. Earth Sci. 55 (4), 373–396.
Spagnolo, M., Clark, C.D., Ely, J.C., Stokes, C.R., Anderson, J.B., Andreassen, K., King, E. C., 2014. Size, shape and spatial arrangement of mega-scale glacial lineations from a large and diverse dataset. Earth Surf. Process. Landf. 39 (11), 1432–1448.
Stevenson, D.J., 2001. Mars' core and magnetism. Nature 412 (6843), 214–219.
Stokes, C.R., 2018. Geomorphology under ice streams: Moving from form to process. Earth Surf. Process. Landf. 43 (1), 85–123.
Stokes, C.R., Clark, C.D., Lian, O.B., Tulaczyk, S., 2006. Geomorphological map of ribbed moraines on the Dubawnt Lake Palaeo-Ice stream bed: a signature of ice stream shut-down? J. Maps 2 (1), 1–9.
Stokes, C.R., Lian, O.B., Tulaczyk, S., Clark, C.D., 2008. Superimposition of ribbed moraines on a palaeo-ice-stream bed: implications for ice stream dynamics and shutdown. Earth Surface Process. Landforms 33 (4), 593–609.
Storrar, R., Stokes, C.R., 2007. A glacial geomorphological map of Victoria Island, Canadian Arctic. J. Maps 3 (1), 191–210.
Sugden, D.E., Glasser, N., Clapperton, C.M., 1992. Evolution of large roches moutonnées. Geografiska Annaler: Series A, Physical Geography 74 (2–3), 253–264.
Sun, V.Z., Milliken, R.E., 2015. Ancient and recent clay formation on Mars as revealed from a global survey of hydrous minerals in crater central peaks. J. Geophys. Res. 120 (12), 2293–2332.
Tanaka, K.L., Davis, P.A., 1988. Tectonic history of the Syria Planum province of Mars. J. Geophys. Res. Solid Earth 93 (B12), 14893–14917.
Tanaka, K.L., Skinner Jr., J.A., Dohm, J.M., Irwin III, R.P., Kolb, E.J., Fortezzo, C.M., Platz, T., Michael, G.G., Hare, T.M., 2014. Geologic Map of Mars.
Thaisen, K.G., Schieber, J., Dumke, A., Hauber, E., Neukum, G., 2008. Geomorphic evidence for significant glacial and fluvial activity in Candor Chasma, Mars. LPI 1391, 2358.
Thollot, P., Mangold, N., Ansan, V., Le Mouélic, S., Milliken, R.E., Bishop, J.L., Weitz, C. M., Roach, L.H., Mustard, J.F., Murchie, S.L., 2012. Most Mars minerals in a nutshell: Various alteration phases formed in a single environment in Noctis Labyrinthus. J. Geophys. Res. 117 (E11).
Tirsch, D., Jaumann, R., Pacifici, A., Poulet, F., 2011. Dark aeolian sediments in Martian craters: Composition and sources. J. Geophys. Res. 116 (E3).
Trenhaile, A.S., 1975. The morphology of a drumlin field. Ann. Assoc. Am. Geogr. 65 (2), 297–312.
Tulaczyk, S.M., Scherer, R.P., Clark, C.D., 2001. A ploughing model for the origin of weak tills beneath ice streams: a qualitative treatment. Quat. Int. 86 (1), 59–70.
Urata, R.A., Toon, O.B., 2013. Simulations of the martian hydrologic cycle with a general circulation model: Implications for the ancient martian climate. Icarus 226 (1), 229–250.
Waldron, J.W., Gagnon, J.F., 2011. Recognizing soft-sediment structures in deformed rocks of orogens. J. Struct. Geol. 33 (3), 271–279.
Ward, W.R., 1973. Large-scale variations in the obliquity of Mars. Science 181 (4096), 260–262.
Ward, A.W., 1979. Yardangs on Mars: Evidence of recent wind erosion. J. Geophys. Res. Solid Earth 84 (B14), 8147–8166.
Watkins, J.A., Ehlmann, B.L., Yin, A., 2015. Long-runout landslides and the long-lasting effects of early water activity on Mars. Geology 43 (2), 107–110.
Watkins, J.A., Ehlmann, B.L., Yin, A., 2020. Spatiotemporal evolution, mineralogical composition, and transport mechanisms of long-runout landslides in Valles Marineris. Mars. Icarus 113836.
Watters, T.R., 1991. Origin of periodically spaced wrinkle ridges on the Tharsis Plateau of Mars. J. Geophys. Res. 96 (E1), 15599–15616.
Weitz, C.M., Bishop, J.L., Thollot, P., Mangold, N., Roach, L.H., 2011. Diverse mineralogies in two troughs of Noctis Labyrinthus, Mars. Geology 39 (10), 899–902.
Weitz, C.M., Bishop, J.L., Grant, J.A., 2013. Gypsum, opal, and fluvial channels within a trough of Noctis Labyrinthus, Mars: Implications for aqueous activity during the Late Hesperian to Amazonian. Planet. Space Sci. 87, 130–145.
Weitz, C.M., Berman, D., Rodriguez, A., Bishop, J.L., 2018. Geologic Mapping and Studies of Diverse Deposits at Noctis Labyrinthus, Mars. LPICo 1920, 7029.
Williams, J.P., van der Bogert, C.H., Pathare, A.V., Michael, G.G., Kirchoff, M.R., Hiesinger, H., 2018. Dating very young planetary surfaces from crater statistics: A review of issues and challenges. Meteorit. Planet. Sci. 53 (4), 554–582.
Wilson, L., Head III, J.W., 2002. Tharsis-radial graben systems as the surface manifestation of plume-related dike intrusion complexes: Models and implications. J. Geophys. Res. 107 (E8), 1–24.
Wise, D.U., Golombek, M.P., McGill, G.E., 1979. Tectonic evolution of Mars. J. Geophys. Res. Solid Earth 84 (B14), 7934–7939.
Witbeck, N.E., Tanaka, K.L., Scott, D.H., 1991. Geologic map of the Valles Marineris region, Mars. US Geological Survey Report.
Wordsworth, R.D., 2016. The climate of early Mars. Annu. Rev. Earth Planet. Sci. 44, 381–408.
Wordsworth, R., Forget, F., Millour, E., Head, J.W., Madeleine, J.B., Charnay, B., 2013. Global modelling of the early martian climate under a denser CO2 atmosphere: Water cycle and ice evolution. Icarus 222 (1), 1–19.
Wordsworth, R., Kalugina, Y., Lokshtanov, S., Vigasin, A., Ehlmann, B., Head, J., Wang, H., 2017. Transient reducing greenhouse warming on early Mars. Geophys. Res. Lett. 44 (2), 665–671.
Yin, A., 2012a. An episodic slab-rollback model for the origin of the Tharsis rise on Mars: Implications for initiation of local plate subduction and final unification of a kinematically linked global plate-tectonic network on Earth. Lithosphere 4 (6), 553–593.
Yin, A., 2012b. Structural analysis of the Valles Marineris fault zone: Possible evidence for large-scale strike-slip faulting on Mars. Lithosphere 4 (4), 286–330.
Zhong, S., 2009. Migration of Tharsis volcanism on Mars caused by differential rotation of the lithosphere. Nat. Geosci. 2 (1), 19–23.
Zimbelman, J.R., Griffin, L.J., 2010. HiRISE images of yardangs and sinuous ridges in the lower member of the Medusae Fossae Formation, Mars. Icarus 205 (1), 198–210.
Zuber, M.T., 2001. The crust and mantle of Mars. Nature 412 (6843), 220–227.